CONSTRUCTOR UNIVERSITY

Layer-Resolved Spectroscopic Study of Tensile Strain Effects in Flexible Organic Electronic Structures

by

Mahya Ghorab

A thesis submitted in partial fulfillment of the requirements for the degree of

Doctor of Philosophy in Electrical Engineering

Approved Dissertation Committee

Prof. Dr.-Ing.habil. Mojtaba Joodaki
Constructor University

Prof. Dr. Veit Wagner
Constructor University

Prof. Dr. Dr. Arnulf Materny
Constructor University

Prof. Dr. Björn Lüssem
Bremen University

Date of Defense: 30.04.2026

School of Computer Science & Engineering

Statutory Declaration

Family Name, Given/First Name	Ghorab, Mahya
Matriculationnumber	20332738
What kind of thesis are you submitting: Bachelor-, Master- or PhD-Thesis	PhD-Thesis

English: Declaration of Authorship

I hereby declare that the thesis submitted was created and written solely by myself without any external support. Any sources, direct or indirect, are marked as such. I am aware of the fact that the contents of the thesis in digital form may be revised with regard to usage of unauthorized aid as well as whether the whole or parts of it may be identified as plagiarism. I do agree my work to be entered into a database for it to be compared with existing sources, where it will remain in order to enable further comparisons with future theses. This does not grant any rights of reproduction and usage, however.

The Thesis has been written independently and has not been submitted at any other university for the conferral of a PhD degree; neither has the thesis been previously published in full.

German: Erklärung der Autorenschaft (Urheberschaft)

Ich erkläre hiermit, dass die vorliegende Arbeit ohne fremde Hilfe ausschließlich von mir erstellt und geschrieben worden ist. Jedwede verwendeten Quellen, direkter oder indirekter Art, sind als solche kenntlich gemacht worden. Mir ist die Tatsache bewusst, dass der Inhalt der Thesis in digitaler Form geprüft werden kann im Hinblick darauf, ob es sich ganz oder in Teilen um ein Plagiat handelt. Ich bin damit einverstanden, dass meine Arbeit in einer Datenbank eingegeben werden kann, um mit bereits bestehenden Quellen verglichen zu werden und dort auch verbleibt, um mit zukünftigen Arbeiten verglichen werden zu können. Dies berechtigt jedoch nicht zur Verwendung oder Vervielfältigung.

Diese Arbeit wurde in der vorliegenden Form weder einer anderen Prüfungsbehörde vorgelegt noch wurde das Gesamtdokument bisher veröffentlicht.

Mahya Ghorab 23.07.2026

……

Date, Signature

Abstract

This thesis investigates how uniaxial tensile strain influences the optical and molecular properties of polymer thin films relevant to flexible organic electronic applications. The work focuses on poly(ethylene terephthalate) (PET) as a representative flexible substrate and poly(3-hexylthiophene-2,5-diyl) (P3HT) as a model semiconducting polymer. The materials are studied as single layers and in PET/P3HT and PET/PEDOT:PSS/P3HT stacks at room-temperature.

Mechanical deformation is applied in a controlled and reproducible manner using a custom-built stretching setup. The strain response is examined using ultraviolet–visible spectroscopy and Raman spectroscopy. The former resolves strain-induced variations in band gap and spectral response, while the latter provides molecular-level insight into chain reorientation, conformational changes, and defect formation during and after deformation.

For PET substrates, uniaxial tensile strain leads to a progressive degradation of optical performance. An increase in absorption across the ultraviolet and visible spectral regions is observed. Beyond approximately 5% strain, these changes become irreversible and are accompanied by clear spectroscopic signatures of permanent structural modification. The results distinguish two deformation regimes, with elastic behavior at low strain and irreversible structural changes at higher strain levels.

For P3HT thin films, the optical band gap remains stable up to 7% strain within experimental resolution. This stability is independent of annealing temperature and stack configuration. At 10% strain, a small but reproducible increase of approximately 4–5 meV is detected, indicating a threshold beyond which electronic perturbation becomes measurable.

Raman spectroscopy shows that the strain response of P3HT depends strongly on thermal history, with annealing redistributing strain sensitivity between band-position shifts and linewidth evolution. Unannealed films accommodate deformation mainly through reversible chain alignment. After annealing at 50 °C, the response becomes mixed, with stronger contributions from microstructural heterogeneity under strain. After annealing at 75 °C, deformation is increasingly constrained and accompanied by pronounced strain-induced defect accumulation. The introduction of a PEDOT:PSS interlayer modifies strain transfer and redistributes strain accommodation across the stack, reducing strain localization and enhancing mechanical tolerance, particularly in highly ordered films.

Overall, this work establishes how mechanically applied strain modifies optical response and molecular structure in polymer thin films under realistic operating conditions. Furthermore, it clarifies how these responses depend on processing history

and stack architecture. The results establish experimentally grounded strain limits for flexible device operation andprovide quantitative constraints for mechanical and optoelectronic modeling.

Contents

List of Tables

List of Figures

List of Abbreviations

AFM Atomic Force Microscopy. 114

AM1.5 Standard Solar Spectrum (Air Mass 1.5). 61, 66, 73

BHJ Bulk Heterojunction. 1, 30–32, 57, 60, 62, 65, 66

BOPET Biaxially Oriented Polyethylene Terephthalate. 12

CBM Conduction Band Minimum. 104

CCD Charge-Coupled Device. 55

CNC Computer Numerical Control. 49

CT Charge-Transfer. 7–9, 11, 31, 62, 63, 66

CV Cyclic Voltammetry. 104

D–A Donor–Acceptor. 6–8, 30, 31, 37, 60, 62, 65, 66, 70, 72

DC Direct Current. 50

DFG German Research Foundation (Deutsche Forschungsgemeinschaft). 3

DFT Density Functional Theory. 38, 72, 113

DOS Density of States. 65, 66, 70

EA Electron Affinity. 105

ETL Electron Transport Layer. 57

FEM Finite Element Modeling. 4, 32, 46, 56–58, 115

FF Fill Factor. 9–11, 28–31, 67–69, 73

FWHM Full Width at Half Maximum. 17, 55, 76, 85, 87, 89, 92, 95, 96, 99, 118, 119, 121, 122, 125, 126, 129, 130, 133, 136, 137

GIWAXS Grazing-Incidence Wide-Angle X-ray Scattering. 69

HC3 Heteroskedasticity-consistent standard errors (type HC3). 110, 111

HOMO Highest Occupied Molecular Orbital. 7–9, 17, 20, 31, 37, 66, 72

HTL Hole Transport Layer. 57

I–V Current–Voltage. 27, 28

I/O Input/Output. 51

IDE Integrated Development Environment. 51

IoT Internet of Things. 2, 47

IP Ionization Potential. 105

IPES Inverse Photoelectron Spectroscopy. 104

IR Infrared. 95, 120

Isc Short-circuit current. 28, 29

ITO Indium Tin Oxide. 10, 57, 58, 60, 63

J–V Current density–Voltage. 28, 67, 69, 73

Jsc Short-circuit current density. 11, 28–31, 67, 68, 73

KDE Kernel Density Estimate. 107

LUMO Lowest Unoccupied Molecular Orbital. 7–9, 17, 20, 31, 37, 66, 72

NEMA National Electrical Manufacturers Association (motor frame standard). 50

NFA Non-Fullerene Acceptor. 11

OLED Organic Light-Emitting Diode. 76

OLS Ordinary Least Squares. 106

OSC Organic Solar Cell. 1–4, 6, 7, 10, 11, 27–32, 38, 46, 47, 52, 56, 57, 59–66, 68–70, 76, 79, 82, 105

P3HT Poly(3-hexylthiophene). 3–6, 15–21, 23–25, 27, 29–32, 36, 37, 39–42, 45–49, 52–55, 57, 60, 62–69, 71–73, 101–103, 105–108, 111–122, 124–126, 128–130, 132, 133, 135–137

PCBM Phenyl-C_{61}-Butyric Acid Methyl Ester. 29–31, 37, 46, 57, 60, 62–68, 71–73, 113

PCE Power Conversion Efficiency. 28–31, 64, 67, 68

PDMS Poly(dimethylsiloxane). 29, 43

PEDOT poly(3,4-ethylenedioxythiophene). 125

PEDOT:PSS Poly(3,4-ethylenedioxythiophene):Poly(styrenesulfonate). 5, 29, 48, 52–55, 57, 60, 63, 64, 67, 101–103, 105, 111, 112, 114, 117, 119, 121, 125, 126, 128–130, 133, 135–137

PEN Polyethylene Naphthalate. 10

PES Photoelectron Spectroscopy. 104

PET Poly(ethylene terephthalate). 2–6, 10–14, 20, 23–25, 27, 32–36, 38, 47–49, 52–55, 75–77, 79, 81, 82, 85, 87, 95–103, 111, 114, 117–119, 121, 122, 124–126, 128–130, 132, 133, 135–137

PWM Pulse-Width Modulation. 51

Rp Shunt resistance. 28

rr-P3HT Regioregular Poly(3-hexylthiophene). 30, 117, 120, 136

Rs Series resistance. 28

SEM Scanning Electron Microscopy. 114

SRH Shockley–Read–Hall (recombination). 65

TAR Trap-Assisted Recombination. 64–66

TOST Two One-Sided Tests (equivalence testing). 110

TPU Thermoplastic Polyurethane. 2

ULWD Ultra-Long Working Distance (objective). 55

USB Universal Serial Bus. 51

UV–Vis Ultraviolet–Visible (absorption spectroscopy). 5, 18–20, 23, 26, 48, 51, 52, 54, 76, 79, 82, 87, 97, 98, 102, 104, 105

VBM Valence Band Maximum. 104

Voc Open-circuit voltage. 7, 9, 11, 28–31, 67–69, 72, 73

WAXD Wide-Angle X-ray Diffraction. 87, 95

WF Work Function. 38

ZnO Zinc Oxide. 57, 60, 63, 64, 67

Chapter 1

Introduction

1.1 Organic Solar Cells – An Overview

The exploration of organic materials for photovoltaic applications began in the mid-20th century. In 1958, Martin Pope first observed photovoltaic behaviour in organic materials through studies on anthracene crystals, demonstrating their potential for photovoltaic applications [1, 2]. A significant advancement occurred in 1986, when Ching W. Tang developed the first efficient bilayer Organic Solar Cell (OSC). The device achieved roughly 1% efficiency and established the donor–acceptor heterojunction concept [3]. In 1995, this architecture evolved substantially with the introduction of the Bulk Heterojunction (BHJ) structure by Alan J. Heeger and colleagues, greatly enhancing charge separation and device efficiency [4]. Subsequently, in 2011, industrial relevance for this technology increased notably when Mitsubishi Chemical reported a landmark 10% efficiency, validating commercial viability prospects for these cells [5]. More recently, between 2015 and 2016, the emergence of non-fullerene acceptors significantly elevated efficiencies beyond 18%, marking a pivotal advance toward industrial competitiveness [6, 7].

OSCs occupy a unique position among emerging photovoltaic technologies, offering environmental and material advantages that complement rather than compete with established platforms. Crystalline silicon devices continue to dominate the market due to their unmatched stability and mature manufacturing infrastructure [8]. However, their inherent rigidity limits integration into lightweight or deformable systems. In addition, their energy-intensive production further constrains such applications. Perovskite solar cells, by contrast, have demonstrated record efficiencies exceeding 25%, but their long-term durability and the presence of toxic lead compounds remain significant barriers to commercialization [9].

On the other hand, OSCs, can be processed from abundant and non-toxic materials

under ambient or low-temperature conditions. Their compatibility with solution printing and roll-to-roll fabrication enables production on flexible substrates at industrial scale. This offers an attractive pathway toward sustainable, mechanically compliant photovoltaics. With certified power conversion efficiencies now reaching 19.8% [10], these devices are narrowing the performance gap with inorganic counterparts. They are also redefining how photovoltaic technology can merge with next-generation electronics. In particular, such systems are thin, adaptable, and seamlessly integrated into everyday surfaces [11–16]. The following section examines how the mechanical flexibility of OSCs enables applications and device geometries that are not feasible with rigid solar technologies.

1.2 Mechanical Compliance: From Advantage to Challenge

The mechanical flexibility of OSCs stems from both the intrinsic compliance of their organic semiconductors and the ultrathin design of the device stack. The active layer is typically composed of π-conjugated polymers or small molecules with elastic moduli in the 0.1–10 GPa range. Hence, the device can sustain moderate strain without fracture [17, 18]. However, flexibility, is not determined by material softness alone. It also arises from structural design where all functional layers ranging from electrodes to encapsulation are fabricated as nanometer scale films (usually < 300 nm). This would lead to reduction in bending stiffness and allows the multilayer stack to deform coherently [19, 20]. This compliance is effective only when the active layers are supported on flexible substrates such as Poly(ethylene terephthalate) (PET) or Thermoplastic Polyurethane (TPU), emphasizing the need for system level optimization in achieving mechanically robust devices [21].

This mechanical resilience enables OSCs to function in areas where rigid photovoltaic technologies fail. In wearable electronics, they can be laminated onto fabrics or stretchable supports, maintaining performance under repeated deformation. Their flexibility also facilitates integration into foldable displays, electronic skin, and soft robotic components that experience dynamic strain [22, 23]. Beyond portable systems, OSCs are promising for building and vehicle integrated photovoltaics, where their conformability to curved and textured surfaces supports aesthetic and functional design [24]. They also provide lightweight and low-cost power for distributed devices such as Internet of Things (IoT) sensors where compact and adaptable energy sources are essential [25].

1.2.1 From Mechanical Flexibility to Functional Uncertainty

Over the past decade, a substantial body of research has emerged focusing on flexible and stretchable OSCs. The primary goal of these studies, such as those by Wardani *et al.* [26], Dauzon *et al.* [27], and Wang *et al.* [28], has been to enhance device architectures for improved mechanical compliance, durability, and application versatility in wearable and bio-integrated electronics. The strategies proposed include intrinsically stretchable polymers, pre-strained buckling mechanisms, hybrid electrodes, and multilayer interfacial engineering. While this body of work demonstrates significant progress, strain is generally framed as an external constraint to be mitigated, rather than as a dynamic variable intrinsically modulating the physical behaviour of device materials [29–34]. The influence of mechanical stress on the optoelectronic properties of functional layers, such as the active layer, remains only partially understood. These strain-induced alterations including changes in optical absorption, molecular alignment, and charge transport pathways are critical because they ultimately determine the propagation of stress through the device and modulate its overall performance [35–38].

1.3 Thesis Objectives and Scope

This thesis is driven by the need to understand how mechanical strain influences the optical and structural behaviour of materials used in OSCs. The fundamental question of how deformation alters the functional properties of individual layers, such as substrates and active materials, remains largely open. This is particularly true under realistic fabrication and operating conditions.

This work began as part of a broader German Research Foundation (Deutsche Forschungsgemeinschaft) (DFG) proposal that aimed to study strain effects at the device level in complete OSCs using complementary characterization techniques. As the research progressed, it became clear that interpreting strain behaviour in multilayer devices requires first knowing how each layer responds on its own. Existing studies offered little data on how separate layers such as substrates, transport, or active materials change optically or structurally under stress. Without that knowledge, device-level observations could not be traced to their physical origins.

To address this gap, the focus of the thesis shifted toward a more fundamental investigation. By characterizing the optical and molecular responses of key layers such as PET and Poly(3-hexylthiophene) (P3HT) under strain, this work establishes the foundation needed to interpret and model strain effects across complete OSC stacks. Rather than diverging from the original DFG objectives, this approach forms a nec-

essary first step toward reliable, physics-based understanding of strain in flexible photovoltaic systems. The specific objectives of this research are as follows:

- **Optical characterization:** Examine how mechanical strain affects the optical absorption of representative OSC materials. Specifically, focus on PET as a flexible substrate and P3HT as a model photoactive layer. Using UV–Vis absorption spectroscopy, analyze strain-dependent spectral changes to determine how deformation influences light-harvesting behaviour.
- **Molecular and structural analysis:** Investigate the molecular-level origins of these optical responses using Raman spectroscopy to probe strain-induced shifts in vibrational modes.
- **Modeling and interpretation:** Employ Finite Element Modeling (FEM) to simulate how mechanical strain propagates through a simplified multilayer OSC architecture.

Together, these studies provide an experimentally grounded and mechanistically resolved understanding of how mechanical deformation modulates the optical and molecular behaviour of OSC materials. This understanding lays the groundwork for the design of reliable and strain-resilient flexible photovoltaics.

1.4 Key Contributions

This thesis offers several original contributions to the understanding of how mechanical strain influences the behaviour of OSC materials under realistic conditions:

- **Identification of critical material-level knowledge gaps limiting strain modeling in OSCs.** Through initial simulation efforts, this work highlighted the absence of key strain-dependent material parameters including optical absorption changes and structural responses, which motivated the subsequent experimental focus.
- **Experimental quantification of strain-induced optical changes in OSC-relevant materials.** The study provides new data on how uniaxial strain affects the optical absorption behaviour of PET (substrate) and P3HT (photoactive layer), offering direct insight into light-harvesting variations under deformation.

- **In-situ probing of molecular structural changes under mechanical strain.** By capturing real-time vibrational and conformational changes in PET and P3HT using Raman spectroscopy. The work reveals how mechanical stress affects molecular orientation and bonding. This information is used to complement and explain the optical behaviour.

- **Development and use of a custom-built mechanical stretcher setup.** A custom strain-application device was designed and implemented to enable controlled and repeatable deformation of thin films during characterization. This setup played a critical role in enabling both ex-situ and in-situ measurements.

1.5 Structure of Dissertation

The remainder of this dissertation is organized as follows. Chapter 2 presents the key physical concepts and the experimental techniques employed in this study for probing strain effects in flexible organic electronic layers. Chapter 3 reviews recent studies on mechanical deformation in organic electronic systems and positions this work within the existing literature. Chapter 4 describes the experimental design, sample preparation procedures, and measurement protocols used to systematically probe strain-dependent behaviour in the investigated thin-film systems. Chapter 5 presents the electrical modeling approach used to represent strain-induced effects in organic solar cells. Chapter 6 investigates the optical and spectroscopic response of PET substrates under tensile strain. Chapter 7 examines the strain dependence of the optical bandgap of P3HT thin films using Ultraviolet–Visible (absorption spectroscopy) (UV–Vis) spectroscopy and statistical analysis. Chapter 8 analyzes strain-induced molecular reorganization in PET/P3HT and PET/Poly(3,4-ethylenedioxythiophene):Poly(styrenesulfonate) (PEDOT:PSS)/P3HT stacks using Raman spectroscopy. Finally, Chapter 9 summarizes the main findings and outlines perspectives for future work.

Chapter 2

Background

This chapter presents the theoretical and conceptual foundations required for the subsequent experimental and analytical work. Section 2.1 reviews the operating principles of organic solar cells, Section 2.2 examines the structural, optical and mechanical properties of PET as a flexible substrate, Section 2.3 explores the mechanisms by which mechanical strain influences molecular ordering as well as optical/vibrational responses of conjugated polymers (with a focus on P3HT), and Section 2.4 provides a detailed account of the spectroscopic techniques (UV–Vis absorption and Raman scattering) applied in this research.

2.1 Fundamentals of Organic Solar Cells

OSCs exploit the unique photophysical, charge-transport, and interfacial phenomena of conjugated organic semiconductors to convert sunlight into electrical power. Although they share several operational principles with inorganic photovoltaic technologies, the disordered, excitonic, and molecular-scale nature of organic absorber materials necessitates a dedicated conceptual framework [39].

In this section, we develop a fundamental understanding of: (i) photophysical generation and dissociation of bound excitons; (ii) the Donor–Acceptor (D–A) interface and charge separation; (iii) charge transport and collection in disordered organic networks; (iv) typical device architectures with emphasis on mechanical flexibility; (v) material considerations for donor and acceptor compounds; and (vi) performance metrics and loss mechanisms.

These foundations establish the physical context necessary to interpret the strain-induced optical and molecular transformations discussed in subsequent chapters.

2.1.1 Photophysical Principles

OSCs rely on light absorption and charge generation within π-conjugated semiconductors, whose electronic structure differs fundamentally from that of crystalline inorganic materials. In these molecular solids, electronic wavefunctions are confined along polymer backbones or small molecule cores. Intermolecular interactions are dominated by weak van der Waals forces. As a consequence, the electronic states remain highly localized, and the material exhibits a low dielectric constant (typically $\varepsilon_r \approx 3$–4) [40]. This low permittivity provides only weak dielectric screening, meaning that the medium does not substantially reduce the Coulomb attraction between an electron and a hole. Together with the localized nature of the wavefunctions, this leads to strongly bound excitons with binding energies far exceeding thermal energy at room temperature. Thus, when a photon promotes an electron from the Highest Occupied Molecular Orbital (HOMO) to the Lowest Unoccupied Molecular Orbital (LUMO), the electron and hole remain strongly bound as a neutral excitation—an exciton—with binding energies of 0.3–1 eV. As mentioned, this exceeds the $k_\mathrm{B}T$ at room temperature (where k_B is Boltzmann's constant and T the absolute temperature, giving $k_\mathrm{B}T \approx 26$ meV at room temperature) [41].
Because of this strong binding, excitons in OSCs do not separate spontaneously into free carriers. Instead, charge generation follows a sequence:

(i) Photon absorption in either the donor or the acceptor generates a singlet exciton ($S = 0$). In modern non-fullerene OSCs, the acceptor often contributes substantially to exciton generation due to its strong and broad optical absorption [42].

(ii) Exciton diffusion proceeds by incoherent hopping over a limited diffusion length $L_\mathrm{D} \sim 5$–20 nm, which is material and order-dependent [43].

(iii) At a D–A interface, the exciton undergoes charge transfer, forming an interfacial Charge-Transfer (CT) state.

(iv) The CT state either dissociates into spatially separated charges that drift/hop to the electrodes, or recombines back to the ground state. Recombination is termed geminate when the electron and hole originate from the same exciton [44].

The CT state comprises an electron localized on the acceptor and a hole on the donor, typically separated by only a few nanometers across their interface. Its energy, E_CT, lies below the optical gap E_g^opt. While an adequate energy offset promotes exciton dissociation into free carriers, an excessive offset reduces the achievable V_oc

[45].

Organic semiconductors exhibit large absorption coefficients (often $\alpha > 10^5$ cm^{-1}) near their strongest vibronic transitions which are peaks arising from coupled electronic–vibrational excitations. Thin active layers (tens to $\lesssim 200$ nm) can therefore harvest much of the visible spectrum, but morphology must ensure that excitons reach D–A interfaces within L_D to suppress geminate loss [46].

2.1.2 Donor–Acceptor Interface and Charge Separation

The D–A interface governs the conversion of localized excitons into spatially separated charge carriers. When an exciton reaches the interface, its electron and hole can transfer onto different materials. A donor exciton undergoes an electron transfer to the acceptor, and an acceptor exciton undergoes a hole transfer to the donor. Both pathways form an interfacial CT state [45].

The energy of this CT state, E_{CT}, is often approximated by the difference between the donor HOMO and the acceptor LUMO. This picture captures the main contribution, but it omits an important correction. At the interface, the electronic wavefunctions of donor and acceptor molecules overlap weakly, and this interaction slightly stabilizes the electron–hole pair. The resulting CT energy therefore reflects both the frontier-orbital offset and the degree of electronic coupling across the interface. The strength of this coupling also affects how confined the CT state is. A more delocalized CT electron experiences a reduced Coulomb attraction to the hole and is more likely to separate before recombining [47].

Charge separation competes with geminate recombination, and the balance between the two depends on the interfacial microstructure. When the acceptor phase forms small but ordered domains, the electronic wavefunction of the CT electron can extend over several adjacent acceptor molecules. This partial delocalization gives the electron multiple nearby sites to occupy, increasing the probability of moving away from the interfacial hole. In contrast, if the acceptor molecules are highly disordered or if domains are too small, the CT electron becomes strongly localized and recombines with the hole more readily [48]. In addition to these interfacial processes, high excitation densities introduce an upstream loss channel through exciton–exciton annihilation within the donor or acceptor domains. In this bimolecular process, interactions between closely spaced excitons reduce the steady-state exciton population. This reduction limits the number of excitons that reach the D–A interface and form CT states. As a result, even when interfacial charge separation is efficient, exciton–exciton annihilation can indirectly reduce charge generation under strong illumination or intense optical excitation [49].

Morphology therefore plays a decisive role in governing these processes. When donor and acceptor materials are finely intermixed, the resulting high density of interfaces allows excitons to reach a dissociation site within their inherently short diffusion length. However, excessive mixing comes at a cost, as it introduces energetic disorder that impedes efficient charge transport. At the opposite extreme, large and well-segregated domains favor transport but significantly reduce exciton harvesting. Bulk heterojunction architectures emerged as a practical compromise between these competing requirements; their nanoscale phase separation provides sufficient interfacial area for exciton dissociation while maintaining continuous percolation pathways for charge extraction [50].

2.1.3 Charge Transport and Collection

After separating from the CT state, electrons and holes travel through a structurally disordered organic film. Unlike crystalline semiconductors, where delocalized band states support near-bandlike transport, organic materials contain localized molecular sites with energies that vary from one site to another. Slight differences in local packing, torsional angles, electrostatic microenvironments and intermolecular distances shift the HOMO or LUMO levels slightly. As a result, the material exhibits a distribution of site energies. In many conjugated polymers this distribution is well approximated by a Gaussian density of states, whereas in amorphous small molecules an exponential tail may dominate [51, 52].

Charge carriers move through this landscape by thermally activated hopping. In the Miller–Abrahams picture, a hop to a lower-energy site is energetically favorable, while a hop to a higher-energy site requires thermal activation. A significant fraction of hops therefore involve occupying slightly higher-energy states, which explains why mobility depends strongly on temperature and local electric field. Because carriers must repeatedly overcome such energetic barriers, their mobilities are typically in the range 10^{-4} to $10^{-2}\,\mathrm{cm^2\,V^{-1}\,s^{-1}}$ [51, 53, 54].

Imbalanced mobilities lead to space-charge formation and reduce the internal electric field that drives extraction. For example, if electrons move faster than holes, positive charge accumulates near the cathode, lowering the effective field and reducing both V_{oc} and Fill Factor (FF). Deep traps or localized states introduced by defects further suppress mobility by acting as energetic sinks. The interplay of mobility balance, energetic disorder and trap density therefore controls the magnitude of recombination losses [55–57].

Charge extraction at the electrodes depends on proper alignment between the transport layers and the electrode work functions. A selective contact should facilitate

extraction of one carrier type while blocking the other. If this selectivity is poor, minority carriers may accumulate or recombine at the contact. Such contact-induced losses can reduce the short-circuit current and broaden the distribution of internal fields, lowering both FF and efficiency [58–60].

2.1.4 Device Architecture and Function

The multilayer structure of an OSC reflects the requirements of light absorption, selective charge extraction and mechanical integrity. A typical regular architecture uses a transparent conductive substrate such as Indium Tin Oxide (ITO), followed by a hole-transport layer, the donor–acceptor active layer, an electron-transport layer and a reflective top electrode. In inverted architectures, the stacking order of the transport layers is reversed to improve stability or electrode compatibility [61]. Each layer serves several purposes. The transport layers provide energetic selectivity and reduce interfacial recombination by suppressing carrier leakage. They also smooth surface roughness and help establish a uniform electric field across the active layer. The optical field distribution inside the device depends on layer thicknesses and refractive indices. Excessively absorbing transport layers reduce the effective photocurrent, while insufficiently thick transport layers can lead to extraction losses [62].

Mechanical flexibility introduces additional constraints. Polymer substrates such as PET, Polyethylene Naphthalate (PEN) or ultrathin barrier films permit bending, but they limit allowed processing temperatures. Brittle transparent electrodes like ITO tend to crack under tensile strain, which motivates alternatives such as conductive polymers, metal-nanowire meshes, ultrathin metal films and hybrid electrodes [63, 64]. The active layer must also withstand deformation without disrupting π–π stacking or causing phase separation. Under mechanical loading, fractures can initiate at interfaces, and domains may reorganize or lose continuity. These responses depend on molecular weight, crystallinity, side-chain mobility and overall blend morphology [65, 66].

2.1.5 Material Considerations

Efficient OSC operation requires materials with tailored optical, electronic and mechanical properties. Donor polymers benefit from planar backbones that favor conjugation and intermolecular π–π stacking. The degree of backbone planarity, as well as the arrangement and length of side chains, influences both crystallinity and mechanical compliance. High crystallinity enhances mobility but can reduce strain

tolerance. More amorphous polymers withstand deformation more easily but may sacrifice transport properties. Parameters such as molecular weight and regioregularity also influence morphology, domain size and exciton diffusion [66].
Non-Fullerene Acceptors (NFAs) have reshaped OSCs performance by offering strong absorption, good packing and tunable energy levels. Many NFAs exhibit a donor–acceptor–donor molecular architecture that introduces a significant quadrupole moment. These quadrupolar electrostatic fields affect how molecules pack and modulate the local energy levels within the blend. Their intrinsic intramolecular charge-transfer character lowers the optical bandgap and supports broad absorption in the visible and near-infrared, which increases the contribution of the acceptor phase to photocurrent. NFAs also form well-ordered domains that support efficient electron transport when properly blended with suitable donors [67, 68] .

2.1.6 Performance Metrics

The performance of an OSC is determined by its J_{sc}, V_{oc} and FF. J_{sc} depends on how much light is absorbed and how efficiently excitons are harvested and converted to free carriers. V_{oc} is linked to the energy difference between the optical gap and the CT state, although non-radiative recombination lowers the quasi-Fermi level splitting and therefore limits the attainable voltage. FF reflects losses during extraction that arise from mobility limitations, recombination and insufficient contact selectivity [69, 70].
Organic solar cells typically exhibit lower FF than their inorganic counterparts. Field-dependent mobility and energetic disorder reduce extraction efficiency near the maximum power point, even in well-optimized blends. Transport resistance has been identified as a major factor limiting device performance in many state-of-the-art systems. Contact barriers and imperfect blocking of minority carriers further broaden the distribution of internal fields and contribute to losses [71].
Continual progress in materials design and interfacial engineering has recently enabled single-junction OSCs to exceed power-conversion efficiencies of 19%. These improvements result from enhanced absorption in both donor and acceptor materials, reduced non-radiative voltage losses, improved mobility balance and carefully controlled blend morphology [14]. Having established the operating principles of organic solar cells — from exciton generation and charge separation to carrier transport and collection — it is essential to examine the substrate materials that support these devices in flexible format. In the next section, we focus on PET films, their chemical structure and morphological attributes, optical properties relevant to thin-

film devices, and their role as flexible substrates in organic electronics.

2.2 Polyethylene Terephthalate (PET) as a Flexible Substrate

2.2.1 Chemical Structure and Basic Morphology

PET is a linear aromatic polyester synthesised by the polycondensation of ethylene glycol with terephthalic acid. Its repeat unit combines a flexible aliphatic ethylene glycol segment with a rigid para-substituted phenylene ring linked through ester bonds. This arrangement gives the polymer backbone intermediate stiffness, reflecting contributions from both the aromatic and aliphatic components. These structural features underlie PET's characteristic balance between mechanical robustness, optical clarity and thermal stability. Figure 2.1 shows the molecular structure of PET [72].

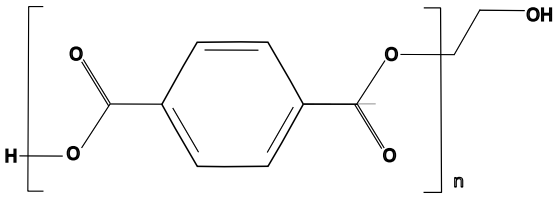

Fig. 2.1: PET Molecular Structure.

In the solid state, PET exhibits a semi-crystalline morphology consisting of crystalline lamellae dispersed within an amorphous matrix. The crystalline regions adopt a triclinic unit cell, while the amorphous regions contain chains with disordered conformations and greater segmental mobility. The relative proportions of these phases depend on processing conditions such as cooling rate, drawing and heat-setting. Commercial films typically display crystallinity values ranging from nearly amorphous to approximately 30–40%, depending on intended application and fabrication route [73].

This two-phase morphology is central to PET's suitability as a flexible substrate. The crystalline lamellae provide dimensional stability, resistance to solvents and a comparatively high elastic modulus. In contrast, the amorphous phase contributes to ductility and toughness, enabling the film to accommodate bending or shaping without brittle failure [72]. Biaxially Oriented Polyethylene Terephthalate (BOPET), a common commercial form, is produced by stretching the film in both the machine and transverse directions prior to heat-setting. This process improves thickness uni-

formity, enhances mechanical strength and stabilises the microstructure by reducing residual stress.

Film geometry also plays a practical role in thin-film electronics. PET substrates are commonly available in thicknesses from tens to a few hundred micrometres. Uniform thickness and low surface roughness support the deposition of nanoscale transport and active layers, reducing the likelihood of interfacial defects. Collectively, PET's intrinsic chemical identity, semi-crystalline architecture and engineered film structure establish its functionality as a mechanically compliant yet dimensionally stable substrate for flexible device stacks [74].

2.2.2 Optical Properties

PET is valued in optoelectronic applications for its high transparency in the visible spectral range. The aromatic ester backbone absorbs primarily in the ultraviolet, where π–π^* transitions of the benzene ring and n–π^* transitions associated with carbonyl groups lie. Consequently, PET exhibits negligible absorption above roughly 350–380 nm, resulting in visible transmission typically exceeding 85–90% for thin films.

The refractive index of PET in the visible is moderately high, with representative values around $n \approx 1.57$–1.58 depending on wavelength. Across this region, the dispersion follows the normal trend described by the Cauchy equation. In this regime,

$$n(\lambda) = A + \frac{B}{\lambda^2} + \frac{C}{\lambda^4},$$

the refractive index decreases smoothly with increasing wavelength, reflecting the fact that PET's electronic transitions lie far into the ultraviolet. This predictable dispersion simplifies optical modelling of thin-film stacks and allows robust control of interference effects in multilayer organic solar cells [75].

Optical scattering in PET films arises from microstructural features that produce refractive-index contrast, such as crystalline lamellae or surface irregularities. Amorphous or low-crystallinity films exhibit very low haze, whereas increased crystallinity can introduce measurable scattering. Commercial biaxially oriented PET is engineered to minimise such effects, resulting in low optical haze suitable for thin-film optoelectronic applications [76].

Overall, PET's optical characteristics—high visible transparency, modest and well-behaved refractive-index dispersion, and controlled scattering—ensure that the substrate acts as an optically passive supporter of device functionality. These properties provide a stable and well-defined optical environment for the active layers in organic

solar cells [77].

2.2.3 PET as a Substrate in Flexible Organic Electronics

Beyond its optical transparency, PET offers a combination of mechanical, thermal and surface properties that make it a practical substrate for flexible organic electronics. Its moderate glass-transition temperature, typically 70–90 °C depending on processing history, accommodates thermal steps used during the deposition or annealing of functional layers while maintaining dimensional stability. PET films can be manufactured with tight thickness tolerances and smooth surfaces, which is important when depositing thin transport or active layers whose performance is sensitive to interfacial uniformity [77].

Surface preparation is a critical step in device fabrication. Native PET has relatively low surface energy and limited chemical reactivity, which can hinder uniform wetting or adhesion of conductive polymers, metal oxides or organic semiconductors. Treatments such as plasma exposure, UV–ozone cleaning or application of primer layers are commonly used to increase surface energy, introduce polar functionalities or remove adventitious contaminants. These treatments improve adhesion and reduce interfacial defects within the device stack.

Mechanically, PET provides sufficient flexibility for bendable or partially rollable electronics, while offering enough rigidity to support typical multilayer architectures. The substrate thickness influences both the minimum achievable bend radius and the extent to which external deformation is transmitted to the active layers. Thinner PET films improve flexibility but are more susceptible to handling damage, whereas thicker films offer greater mechanical stability at the cost of increased stiffness.

Optically, PET acts as a relatively neutral medium in most device configurations. Its refractive index influences the internal optical-field distribution, but its negligible absorption and low haze ensure that incident light reaches the active layer with minimal attenuation or distortion. This stability allows optical simulations and device designs to focus on the functional layers without extensive correction for substrate-related effects [77, 78].

Taken together, the optical, mechanical and surface characteristics of PET support its role as a reliable substrate for flexible organic solar cells and related thin-film electronic devices. These background properties provide the context for its integration in the multilayer structures considered in later chapters of this thesis.

2.3 P3HT: Structure, Packing and Optoelectronic Features

P3HT has long served as a benchmark conjugated polymer in organic electronics due to its well-defined molecular structure, semi-crystalline morphology, and characteristic optical signatures. The combination of a π-conjugated thiophene backbone and flexible hexyl side chains produces a material whose optoelectronic properties are highly sensitive to molecular order. This section outlines the structural and spectroscopic foundations necessary to interpret deformation-induced changes in P3HT, particularly when the polymer is supported on flexible substrates [79].

2.3.1 Molecular Structure, Regioregularity and Hierarchical Packing

P3HT consists of a thiophene ring bearing a hexyl side chain at the 3-position. In thiophene, ring positions are numbered relative to the sulfur atom, and substitution at carbon 3 creates a substituted site, whereas carbon 4 remains unsubstituted. During polymerisation, monomer units may connect through different combinations of these sites, but high-quality electronic behaviour requires predominantly head–tail (HT) coupling, where the substituted carbon of one monomer links to the unsubstituted carbon of the next. A long sequence of HT–HT couplings aligns the hexyl side chains on the same side of the backbone, minimising geometric irregularities and allowing the chain to adopt a more planar conformation. In contrast, head–head

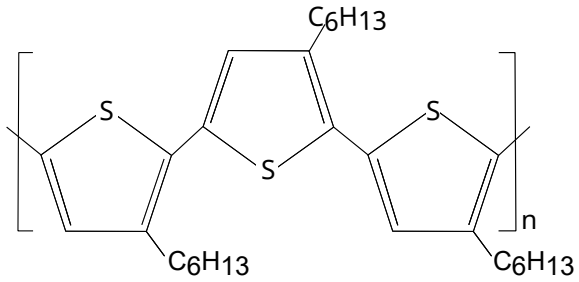

Fig. 2.2: P3HT Molecular Structure.

couplings place two substituted positions adjacent to one another, generating steric congestion—a local crowding of bulky hexyl groups—that forces the backbone to twist and disrupts conjugation [80, 81]. Figure 2.2 shows the molecular structure of P3HT.

The solid-state organisation of P3HT arises from the interplay between these planarised backbones and their alkyl side chains. The backbones constitute the elec-

tronically active cores, while the hexyl side chains segregate into alkyl-rich regions. As the film dries or undergoes thermal or solvent annealing, the chains self-assemble into semi-crystalline domains exhibiting two orthogonal packing directions. Along one direction, the conjugated backbones stack face-to-face in π–π stacks with typical interplanar distances of $\sim$0.36 nm. This stacking direction governs inter-chain electronic coupling, exciton delocalisation and charge mobility. Perpendicular to this, the hexyl side chains from neighbouring chains interdigitate—they insert between one another like interlocking bristles—forming layered alkyl matrices with spacings of approximately 1.6–2.0 nm. These two structural motifs together define the crystalline lamellae of P3HT; neither π–π alignment nor side-chain ordering alone is sufficient to stabilise lamellar order [82, 83].

The resulting film exhibits a hierarchical semi-crystalline morphology in which ordered lamellae are embedded within an amorphous matrix. Inside the crystalline lamellae, the backbones remain relatively planar and closely stacked, and the side chains maintain well-defined registry. In the surrounding amorphous regions, the backbone may twist, coil or deviate from planarity, and the side chains lose their regular organization. At the interfaces between these regions lie tie chains, polymer segments that span neighbouring crystallites and provide both mechanical continuity and charge-transfer pathways. These tie chains influence how strain is transmitted through the film and how charge percolates across domain boundaries, particularly under mechanical deformation [82, 84].

Even within crystalline lamellae, the structure is not perfectly periodic. Small but cumulative variations in lamellar spacing give rise to paracrystallinity, a measure of long-range positional disorder in the lattice. Whereas crystallinity quantifies the fraction of material in ordered domains, paracrystallinity reflects the quality of that order. Typical values of 5–10% in solution-processed P3HT films broaden X-ray diffraction peaks, weaken electronic coupling and limit long-range mobility. Together with torsional fluctuations along individual chains (intra-chain disorder), variations in π–π stacking distances (inter-chain disorder) and differences in orientation or purity between crystallites (inter-aggregate disorder), paracrystallinity shapes the energetic landscape encountered by excitons and charges. The balance among these hierarchical structural elements ultimately governs conjugation length, spatial coherence and the resulting optical lineshapes [85, 86].

2.3.2 Optical Bandgap, Absorption and Vibronic Structure

The optical properties of P3HT reflect the interplay between electronic coupling, vibrational structure and morphological order. The low dielectric constant of organic

semiconductors produces strongly bound excitons, with binding energies typically in the range of 0.3–0.5 eV [87, 88]. Consequently, the optical bandgap—observed as an absorption onset near ∼600 nm—corresponds to the energy required to create a bound exciton rather than free charges. This excitonic gap is therefore smaller than the underlying HOMO–LUMO (single-particle) gap, and its precise value depends on molecular packing, conjugation length and energetic disorder [89].

A characteristic feature of P3HT absorption is its vibronic progression, typically observed as the 0–0 and 0–1 peaks or shoulders in the visible spectrum. These arise from coupling between the electronic transition and specific backbone vibrational modes, such as C=C stretching. The 0–0 transition corresponds to a purely electronic excitation, whereas the 0–1 transition involves excitation of one vibrational quantum. The spacing between these peaks (∼0.18 eV) provides insight into the strength of electron–phonon coupling in the polymer [90]. The relative intensities of the vibronic peaks are highly sensitive to intermolecular coupling and aggregation type. P3HT predominantly forms weakly coupled H-aggregates, in which the face-to-face arrangement of backbones produces characteristic excitonic splitting patterns. According to the widely applied Spano model, increased structural order narrows the exciton bandwidth and enhances the amplitude of the 0–0 peak relative to the 0–1 peak [87, 91]. Consequently, the amplitude ratio A_{0-0}/A_{0-1} serves as a quantitative optical marker of aggregate order, backbone planarity and exciton coherence length. J-aggregate behaviour, characterised by strong 0–0 intensities and narrow red-shifted absorption, is uncommon in P3HT due to its side-chain-directed packing geometry [92].

Disorder influences the entire absorption lineshape. Torsional fluctuations along the chain, variations in π–π spacing and differences in crystallite orientation broaden the density of states and produce sub-bandgap absorption tails. Increased disorder diminishes vibronic resolution, broadens peak linewidths (larger Full Width at Half Maximum (FWHM)) and shifts the absorption onset to higher energy (blue-shift). Thermal or solvent annealing typically reverses these effects by restoring backbone planarity, enhancing packing and reducing energetic disorder [93]. The absorption spectrum of P3HT thus provides a sensitive probe of its structural state.

2.3.3 Relevance for Spectroscopic Characterisation and Strain Studies

The sensitivity of P3HT's optical and vibrational signatures to molecular conformation and hierarchical packing makes spectroscopic techniques powerful tools for probing structural evolution. Red-shifted absorption onsets, increased A_{0-0}/A_{0-1} ratios,

sharpened vibronic peaks and reduced energetic disorder all indicate improved backbone planarity and stronger inter-chain coupling. Conversely, blue-shifts, broadened peaks and diminished vibronic structure signify increased torsional disorder or weakened packing [94].

Mechanical strain perturbs both chain conformation and inter-chain registry, and deformation therefore induces measurable modifications to these optical descriptors. Stretching can increase torsional disorder, alter π–π spacing, distort the lamellar architecture or redistribute tie-chain load, all of which manifest in UV–Vis absorption and Raman scattering. Spectroscopic analysis thus provides a non-destructive means of tracking how P3HT accommodates mechanical deformation at the molecular level [17, 95].

The conceptual framework developed in this section—linking structure, aggregation, excitonic energetics and vibronic coupling—serves as a foundation for interpreting the strain-dependent optical and vibrational phenomena investigated in later chapters.

2.4 Principles of UV–Vis Absorption Spectroscopy

UV–Vis absorption spectroscopy probes the interaction between incident electromagnetic radiation and electronic excitations in a material. Absorption occurs when the photon energy $h\nu$ is resonant with the energy separation between an initial electronic state ψ_i and a higher-lying state ψ_f, such that

$$E_f - E_i \approx h\nu. \tag{2.1}$$

However, resonance alone is not sufficient for an optical transition to occur. The probability amplitude of absorption is governed by the transition dipole moment

$$\mu_{if} = \langle \psi_f \,|\, \hat{\mu} \,|\, \psi_i \rangle, \tag{2.2}$$

which represents the matrix element of the electric dipole operator between the two electronic states. The operator

$$\hat{\mu} = -e \sum_j \mathbf{r}_j \tag{2.3}$$

denotes the electronic dipole moment of the system. The magnitude $|\mu_{if}|^2$ determines the strength of coupling between the electronic transition and the oscillating electric field of light, and directly contributes to the oscillator strength of the corre-

sponding absorption band.

Transitions with $\mu_{if} \neq 0$ are dipole-allowed and couple efficiently to the radiation field. In contrast, transitions with $\mu_{if} = 0$ are dipole-forbidden within the electric dipole approximation and therefore exhibit negligible intensity in the UV–Vis spectrum.

In conjugated polymers such as P3HT, extended π-electron delocalization along the backbone enhances the magnitude of transition dipole moments. It also strengthens vibronic coupling between electronic and vibrational degrees of freedom. This gives rise to the characteristic vibronic progression observed in their UV–Vis absorption spectra [75, 96, 97].

Experimentally, one measures the transmittance $T = I/I_0$ of a sample with thickness d, where I_0 and I are the incident and transmitted intensities, respectively. The absorbance is defined as

$$A = -\log_{10}(T), \tag{2.4}$$

and is related to the absorption coefficient $\alpha(\nu)$ through the Lambert–Beer law,

$$I = I_0 \exp(-\alpha d)\,, \tag{2.5}$$

or equivalently,

$$A = \alpha d \, \log_{10} e. \tag{2.6}$$

The absorption coefficient α represents the probability per unit path length that a photon is absorbed as it propagates through the sample. A larger α therefore indicates that the material attenuates light more strongly over a given distance [75]. At the molecular level, $\alpha(\nu)$ depends on the number density of absorbers and the oscillator strength, which scales with $|\mu_{if}|^2$ and describes the intrinsic probability of a transition [98]. In isolated molecules, the vibrational substructure of the electronic states gives rise to transitions between pairs of vibronic levels. The Franck–Condon principle dictates that electronic transitions occur much faster than nuclear motion, so absorption is governed by vertical transitions on a potential energy diagram. The spectral signatures associated with these transitions appear as a vibronic progression, typically labelled as the 0–0, 0–1, and 0–2 peaks. The 0–0 transition corresponds to excitation from the vibrational ground state of the electronic ground state to the vibrational ground state of the excited state; the 0–1 and higher transitions populate excited vibrational levels. Their relative intensities reflect the overlap between vibrational wavefunctions and therefore encode information about the stiffness of molecular modes and the coupling between electronic and nuclear degrees of freedom [91, 94, 96]

In condensed phases such as conjugated polymer films or molecular crystals, electronic excitations are no longer confined to a single molecular unit. Instead, they form Frenkel excitons, i.e. bound electron–hole pairs with relatively large binding energies arising from the weak dielectric screening of organic solids [99]. The excitonic manifold acquires finite bandwidth due to electronic coupling between neighbouring chromophores; this bandwidth reflects the energetic spread of delocalised excitonic states. Closely related is the concept of exciton coherence length, which characterises the spatial extent over which the exciton wavefunction remains phase coherent before being localised by static or dynamic disorder [100]. A longer coherence length indicates stronger intermolecular coupling and greater structural order [101].
These excitonic effects modify not only the position of the absorption onset but also the vibronic structure. For example, in the weakly coupled H-aggregate regime relevant to many conjugated polymers, increased order enhances the relative intensity of the 0–0 transition, whereas disorder disrupts coherence and broadens the spectrum, suppressing vibronic resolution [91]. Thus, the absorption spectrum in thin films is shaped by both homogeneous broadening mechanisms (finite excited-state lifetimes, phonon interactions) and inhomogeneous broadening (variations in conjugation length, torsional disorder, packing geometry). The superposition of these contributions yields the experimentally observed lineshape, often with sub-bandgap tail states and smoothed vibronic peaks [84].
Practical extraction of bandgap values from such spectra frequently employs Tauc-type analyses, where $(\alpha E)^n$ is plotted against photon energy E and extrapolated to determine an optical gap [102, 103]. In strongly excitonic systems, however, this gap reflects the energy to create the lowest bound exciton rather than the single-particle HOMO–LUMO separation, and must be interpreted within the excitonic framework outlined above.
The principles described here form the theoretical foundation for understanding UV–Vis absorption in polymer substrates (e.g. PET) and conjugated polymer semiconductors (e.g. P3HT). In subsequent sub-chapters these concepts will be connected to morphological features, vibronic coupling, and strain-induced optical modifications relevant to flexible organic solar cell architectures. Figure 2.3 depicts the schematic of the UV–Vis spectroscopy.

2.4.1 UV–Vis Absorption in Conjugated Polymer Films and Polymer Substrates

When the principles outlined in Section 2.4 are applied to thin films of conjugated polymers and flexible substrates, the absorption spectrum becomes a sensitive probe

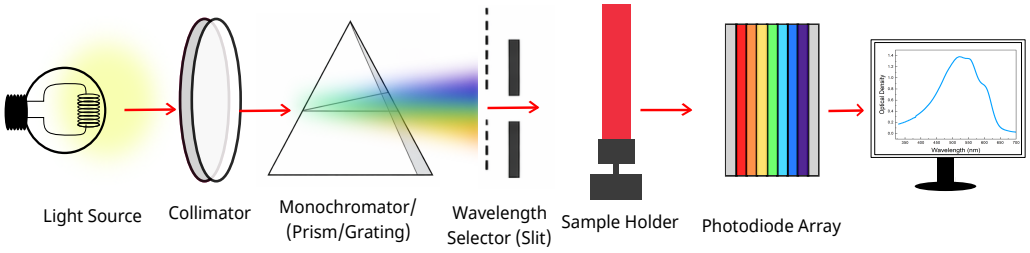

Fig. 2.3: UV-Vis spectroscopy schematic.

of solid-state packing, structural disorder, and microstructural response to mechanical deformation. In conjugated polymers such as P3HT, the lowest-energy absorption band originates from a Frenkel exciton whose energy, lineshape and vibronic structure depend on how polymer chains pack and interact in the condensed phase. The backbone conformation determines the intra-chain conjugation length, while π–π stacking between neighbouring chains controls the magnitude of inter-chain electronic coupling. In this context, "adjacent chromophores" refer to neighbouring conjugated segments—either successive thiophene units along the same polymer chain or overlapping backbone units on different chains—that lie close enough for their electronic transitions to interact. Coupling between such chromophores broadens the excitonic manifold and increases the exciton coherence length, producing characteristic changes in the absorption spectrum [104, 105]

The vibronic progression observed in conjugated polymer films reflects this interplay between intra-chain and inter-chain interactions. In highly ordered regions, the exciton wavefunction delocalises over multiple adjacent chromophores, leading to sharper absorption features and an enhanced intensity of the 0–0 transition relative to higher vibronic peaks. This behaviour is well described by the weakly coupled H-aggregate model, in which the delocalised excitonic states redistribute oscillator strength from the 0–1 transition to the 0–0 transition as structural order increases [94]. In contrast, torsional disorder, paracrystallinity, and variations in local conjugation length localise the exciton and broaden the absorption band, suppressing vibronic structure and shifting the absorption onset to higher energies. These spectral signatures therefore serve as optical fingerprints of the structural hierarchy described earlier in Section 2.3.

Thin-film geometry introduces additional optical effects. Because conjugated polymer films typically have thicknesses on the order of tens to hundreds of nanometres, multiple internal reflections at layer interfaces can generate interference fringes and baseline modulations. The refractive index contrast between the polymer, substrate and any overlying transport layers further modifies the transmitted intensity. Additionally, surface roughness or microstructural heterogeneity leads to wavelength-

dependent scattering, which can distort the absorption edge or mask subtle vibronic features. Accurate interpretation of the absorption coefficient therefore requires careful baseline correction, substrate referencing, and thickness determination [106, 107].

2.5 Principles of Raman Spectroscopy

Raman spectroscopy probes molecular vibrations through the inelastic scattering of light. When monochromatic radiation interacts with a material, the dominant process is Rayleigh scattering, in which photons scatter elastically and retain their original frequency. A much smaller fraction of photons exchange energy with a molecular vibration. If the scattered photon loses energy to the vibration, the process produces a Stokes shift; if it gains energy from an already excited vibration, the scattered photon exhibits an anti-Stokes shift. The frequency difference between the incident and scattered radiation corresponds to the energy of one vibrational quantum, that is, one discrete step in the ladder of vibrational energy levels that characterise a particular molecular vibration [108].

The classical description of Raman scattering begins with the response of a molecule's electron cloud to the oscillating electric field of the incident light. The electric field induces a dipole moment whose magnitude depends on how easily the electron cloud can be distorted, a quantity known as the polarizability. If a vibrational mode causes the polarizability to change periodically as the atoms move, the induced dipole also oscillates at combination frequencies that differ from the incident frequency by the vibrational energy. These shifted components give rise to the Raman spectrum. A vibration is therefore Raman-active if its nuclear motion produces an appreciable change in the molecular polarizability [109].

A quantum mechanical picture offers a complementary interpretation. Under non-resonant excitation conditions, the incident photon energy is not absorbed by the molecule. Inelastic scattering then proceeds through a short-lived virtual state, in which the incident photon perturbs the electron cloud into a transient configuration. As the system relaxes, it may populate a vibrational level with one more or one fewer vibrational quantum than before. The probability of this scattering event depends on how strongly the vibration modifies the polarizability; vibrations that significantly reshape the electron cloud generate strong Raman bands, whereas modes that do not substantially alter the polarizability are weak or absent in the Raman spectrum [110].

Raman peak positions, linewidths and intensities convey information about local bonding and structural disorder. The peak frequency reflects the stiffness of the underlying chemical bond: stronger or shorter bonds vibrate at higher frequencies, whereas weaker or elongated bonds vibrate at lower frequencies. Peak linewidths may broaden due to intrinsic vibrational lifetimes (homogeneous broadening) or structural or environmental variations that give rise to a distribution of slightly different vibrational energies (inhomogeneous broadening). Raman intensities also depend on molecular orientation. Because the polarizability response is anisotropic, the observed signal varies with the angle between the molecular axes and the polarization of the laser and scattered light, making Raman spectroscopy particularly sensitive to chain alignment and orientation in polymeric materials [111, 112].

A powerful extension of the technique is resonance Raman scattering, which occurs when the excitation wavelength approaches an allowed electronic transition of the material. Under these conditions, the virtual intermediate states become energetically close to real electronic states, dramatically enhancing the scattering cross section. In conjugated polymers, excitation near the π–π^* transition preferentially amplifies backbone vibrational modes that couple strongly to the electronic excitation. This resonance effect provides heightened sensitivity to chain planarity, conjugation length and exciton–phonon coupling—features that govern the optoelectronic behaviour of organic semiconductors [113, 114].

These principles make Raman spectroscopy exceptionally informative for flexible electronic materials. Because vibrational energies respond directly to changes in bond lengths, torsional angles and packing geometry, Raman peak positions and intensities are inherently sensitive to mechanical deformation. Tensile strain can elongate bonds, modify conformational order and alter intermolecular coupling, producing characteristic frequency shifts, linewidth changes or variations in relative band intensities. This intrinsic sensitivity underpins the Raman analyses presented later in this thesis, where Raman spectroscopy is used to follow strain-induced structural evolution in both conjugated polymers and polymer substrates. Figure 2.4 depicts the schematic of the UV–Vis spectroscopy.

2.5.1 Raman Signatures in PET and Conjugated Polymers

The Raman spectra of polymeric materials reflect the vibrational modes associated with their backbone chemistry, functional groups, and microstructural organisation. For PET and conjugated polymers such as P3HT, the most diagnostically useful modes are those whose frequencies respond sensitively to conformational order, chain alignment and local bonding environment. These vibrational fingerprints

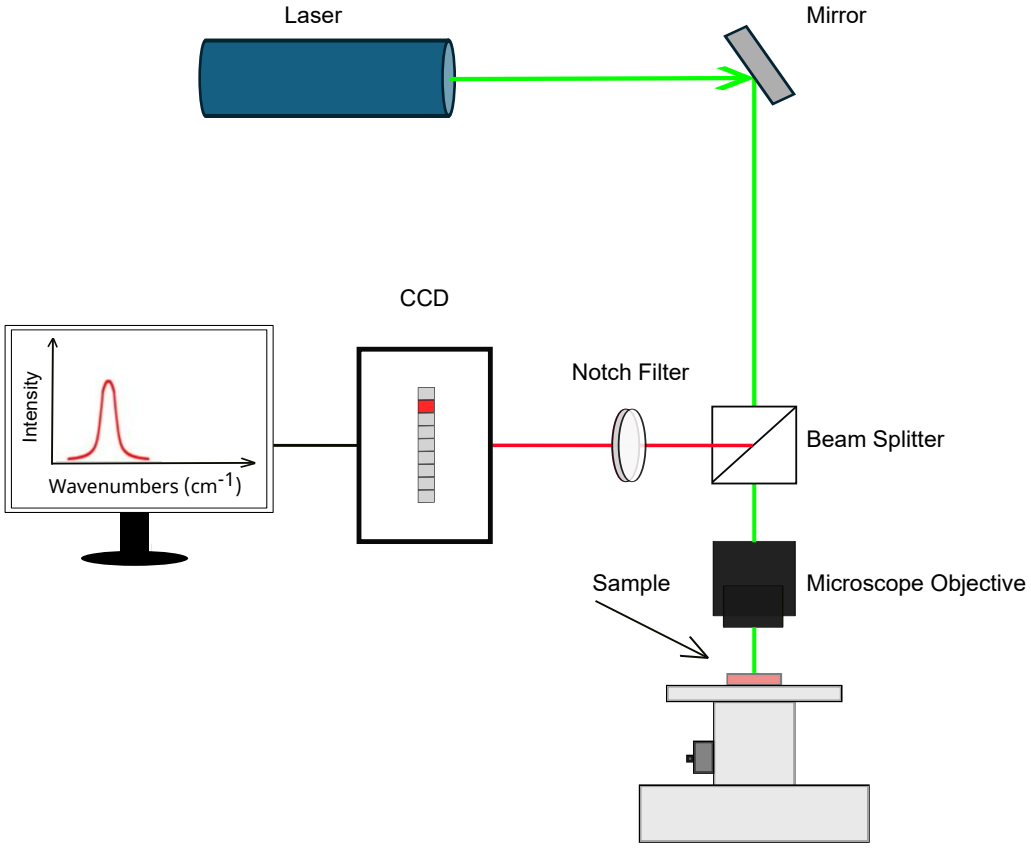

Fig. 2.4: Raman spectroscopy schematic.

form the basis for analysing structural evolution under mechanical strain in later chapters.

In PET, the strongest Raman-active vibrations originate from the aromatic ring, the ester linkage, and the carbonyl group. Prominent modes include the ring-stretching band near 1600–1620 cm^{-1}, the carbonyl C=O stretching mode typically around 1710–1730 cm^{-1}, and several C–O and C–C modes in the 1100–1300 cm^{-1} region. These vibrations involve relatively stiff bonds, making their frequencies highly sensitive to chain orientation and crystalline-to-amorphous ratio in the semi-crystalline matrix [115–118]. Under tensile deformation, PET chains increasingly align along the draw direction, altering the local potential energy landscape of these bonds. As a result, Raman peaks associated with the aromatic and carbonyl groups typically red-shift as the corresponding bonds elongate slightly under load, and peak narrowing may occur if conformational disorder is reduced [119]. These strain-induced spectral signatures provide a quantitative measure of how mechanical stretching reorganises PET's molecular structure.

In P3HT and related conjugated polymers, Raman scattering is dominated by backbone vibrations of the thiophene ring. The most intense feature is the symmet-

ric C=C stretching mode, typically observed between 1440 and 1460 cm^{-1}, which directly reflects backbone planarity, conjugation length and electronic delocalisation. Tensile strain perturbs the thiophene backbone, slightly increasing the C=C bond length and reducing its force constant; this produces a measurable red-shift in the C=C mode. Additional modes include the inter-ring C–C stretch around 1370–1390 cm^{-1} and lower-frequency ring-deformation modes, all of which report on torsional angle, inter-chain coupling and aggregate organisation. Because these vibrations involve the conjugated backbone, their spectral evolution under strain provides a sensitive probe of electronic-structural perturbation in the polymer [93].
The Raman response of P3HT is further influenced by resonance effects when the excitation wavelength approaches the π–π^* absorption band. Under resonance conditions, vibrational modes that couple strongly to the electronic transition are selectively amplified, making the backbone C=C stretch exceptionally intense relative to non-resonant modes. This amplification enhances spectral contrast between ordered and disordered regions: planar, extended backbones exhibit sharper and slightly higher-frequency C=C vibrations, whereas torsionally disordered segments display broader, more red-shifted features. Resonance Raman scattering therefore provides heightened sensitivity to subtle changes in conjugation and aggregate structure [120, 121].
In thin-film geometries, interactions with the substrate and the film morphology can also influence the observed Raman signatures. Surface roughness, molecular orientation relative to the optical axis, and the anisotropy of the Raman tensor all contribute to variations in peak intensities and linewidths. Even without explicit polarization-resolved measurements, partial chain alignment in the film can modify relative band intensities due to the directional nature of the induced dipole. These effects become especially relevant in flexible substrates such as PET, where mechanical deformation alters both molecular orientation and film–substrate interaction [122–124].
Taken together, the Raman-active modes of PET and P3HT provide complementary insights into their molecular structure. The carbonyl and aromatic vibrations in PET sensitively track chain alignment and conformational changes during deformation, while the thiophene backbone modes in P3HT report on conjugation, torsion and aggregate-level order. These vibrational fingerprints form the analytical foundation for the strain-dependent studies presented in subsequent chapters of this thesis.

2.6 Summary

The background developed in this chapter has outlined the essential physical, structural and spectroscopic concepts needed to interpret mechanical and optical behaviour in flexible organic electronic systems. By establishing how excitons are generated, transported and dissociated in conjugated semiconductors, how polymer substrates and active-layer materials organise at the molecular scale, and how UV–Vis and Raman techniques probe these structures, we have built the conceptual basis for analysing how mechanical strain influences both molecular order and optical response at hand.

Together, these foundations enable a rigorous understanding of how deformation can modify chain conformation, intermolecular coupling, vibrational structure and optical transitions in thin-film materials. With this framework in place, we now move from fundamental principles to a broader research context. The following chapter situates this work within the existing scientific literature, examining how current understanding has evolved and where open questions remain, thereby establishing the motivation for the experimental investigations presented later in the thesis.

Chapter 3

State of the Art

Mechanical strain influences the electrical and optical response of organic solar cells, yet the reported effects vary widely because stress distribution depends on several mechanically distinct layers. Device-level measurements alone cannot identify which layer governs a given response. To interpret strain-dependent changes in performance, it is therefore necessary to examine the substrate, the semiconductor thin films, and their molecular structure separately.

This chapter follows that structure. It begins at the device scale, summarizing key findings from tensile strain studies on complete OSC stacks, including changes in Current–Voltage (I–V) characteristics, noise behaviour, and recombination processes. The discussion then moves to the substrate level, where the mechanical and optical response of PET under strain is introduced through prior spectroscopic investigations. The final sections address conjugated polymer thin films, with emphasis on P3HT, and review reported strain effects on its optical bandgap, molecular ordering, and Raman signatures.

Taken together, this organization reflects the hierarchy present in flexible devices: strain is applied to the substrate, transferred into the active layers, and ultimately expressed at the molecular scale.

3.1 Device-Level Strain Effects in Organic Solar Cells

3.1.1 Experimental strain–electrical behaviour in OSCs

OSCs are frequently proposed for applications in which devices bend, stretch, or conform to curved surfaces. Under such conditions, the multilayer stack is subjected to repeated mechanical loading during fabrication and operation. As a result, the electrical response must be examined not only in the unstrained state but also

under applied tensile or bending deformation. The most informative quantities at the device level are the dark and illuminated Current density–Voltage (J–V) characteristics, from which the J_{sc}, V_{oc}, FF, R_s and R_p, ideality factor (η), saturation current (I_0), and the Power Conversion Efficiency (PCE) are obtained. Systematic strain-dependent measurements of these parameters reveal a characteristic trend. Small tensile strain can enhance electrical performance. In contrast, larger strain levels eventually induce cracking, delamination, and electrode failure, leading to device degradation [17, 95].

Several studies have examined roll-to-roll printed OSC modules, which are particularly relevant for large-area and low-cost photovoltaic manufacturing. Salari and co-workers investigated commercial OSC modules with different front electrode materials under uniaxial tensile strain [36]. The modules were mounted on a mechanical stretcher, and strain was applied in controlled microstrain increments. After each step, dark I–V characteristics were recorded, and the device parameters were extracted using a Werner-type small-signal analysis of the diode equation. In this technique, the differential evaluation of the dark I–V characteristics enables independent extraction of the ideality factor, series resistance, and saturation current [125]. For modules employing silver grid electrodes, the R_s decreased under moderate tensile strain. This indicates that the printed silver lines can deform elastically while maintaining efficient lateral conduction. In this strain regime, the extracted I_0 and η remained nearly unchanged, suggesting that the junction properties and bulk recombination processes were still preserved [36]. Once the applied strain surpassed a critical threshold, R_s increased sharply and the diode characteristics deteriorated, which is consistent with microcrack initiation and interfacial damage.

Under illumination, the same group examined the changes in I_{sc}, V_{oc}, FF, and PCE with tensile strain in roll-to-roll printed modules using silver electrodes [35]. For strains in the sub-percent range, the devices exhibited a modest but reproducible improvement in PCE, largely driven by an increase in FF and a smaller rise in I_{sc}. These increases are often attributed to strain-assisted microstructural optimization or improved interfacial contact. However, once the strain exceeded the elastic limit of the stack, the beneficial trend reversed. Both I_{sc} and FF decreased, and the I–V curves became distorted by increased R_s and parasitic pathways introduced by crack formation and delamination within the multilayer structure [35, 95].

To capture the electro-mechanical response at the single-cell level, Ghorab *et al.* performed in situ I–V measurements on a commercial roll-to-roll printed OSC subjected to tensile strain cycles up to 20–30 % elongation [38]. The device was stretched in small increments, and the illuminated I–V characteristics were measured after

each step as well as after strain release. Up to approximately 20 % elongation, all key parameters (I_{sc}, V_{oc}, FF, and PCE) improved relative to the unstrained state. These improvements did not vanish upon releasing the strain; instead, they persisted and became more pronounced in subsequent cycles. This behaviour indicates that a portion of the strain-induced modification is irreversible and reflects permanent microstructural reorganization rather than purely elastic deformation. When the strain reached 30 %, visible cracking appeared in the electrodes and interfaces, accompanied by a sharp deterioration of all electrical parameters. The transition from improved to degraded performance defines the onset of catastrophic failure, separating a pre-catastrophic strain accommodation regime from one dominated by crack propagation and interlayer separation [38, 95].

Low-frequency noise spectroscopy provides complementary insight into strain-induced transport modification. Joodaki and co-workers studied the flicker noise behaviour of OSCs under tensile strain using different electrode materials [37]. For devices with silver electrodes, moderate strain led to a reduction in the 1/f noise level, consistent with improved effective conductivity and reduced fluctuation sources such as interfacial barriers or poorly connected pathways. In contrast, devices employing carbon-based electrodes exhibited increased noise under the same mechanical load. Because flicker noise is highly sensitive to microscopic transport inhomogeneities and defect dynamics, these results underscore the strong dependence of electromechanical stability on electrode composition and its mechanical compliance [37, 95].

Stretchable device architectures provide further insight into the mechanical limits of compliant OSC structures. In their study, Lipomi *et al.* fabricated OSCs on Poly(dimethylsiloxane) (PDMS) substrates incorporating PEDOT:PSS electrodes, with active layers based on P3HT:Phenyl-C_{61}-Butyric Acid Methyl Ester (PCBM) and other donor–acceptor blends. Eutectic gallium–indium served as a compliant top contact [63]. Strain up to 20 % was applied while monitoring photovoltaic parameters and the onset of cracking. The addition of PCBM stiffened P3HT:PCBM films, reducing their crack-onset strain relative to donor-rich blends and making them more susceptible to fracture under repeated stretching. The PEDOT:PSS layer acted as a mechanically robust adhesive between the active layer and the substrate, helping to delay delamination. In these architectures, V_{oc} often increased under tensile strain, while J_{sc} and FF were more sensitive to microcrack formation and electrode distortion [17, 63].

Overall, device-level studies consistently show that mechanical strain affects the electrical response of OSCs in an architecture-dependent manner. Moderate tensile

strain can enhance J_{sc}, V_{oc}, FF, and PCE through strain-induced rearrangements that improve charge transport pathways or interfacial contact. Beyond a mechanically defined threshold, however, crack formation in metallic grids, fracture of brittle transport layers, and delamination at interfaces introduce significant resistive and recombination losses [17, 35–38, 63, 95]. These observations define the experimentally established constraints that any mechanistic model of strain–performance coupling in OSCs must capture and motivate a closer examination of strain–morphology interactions in the active layer.

3.1.2 Strain–morphology interactions in active layers

The electrical response of OSCs under mechanical deformation is closely tied to structural rearrangements within the BHJ active layer. Although several interfaces in the device stack may experience mechanical stress, the D–A blend typically undergoes the most direct and reversible changes when subjected to low or moderate tensile strain. These changes include polymer-chain alignment, variations in the aggregate fraction, shifts in the crystalline–amorphous domain balance, and local rearrangement of donor- and acceptor-rich regions. Each of these processes influences charge transport, recombination, and photogeneration, and therefore affects parameters such as J_{sc}, V_{oc}, FF, and PCE [126, 127].

The influence of strain on polymer ordering has been studied extensively for conjugated polymers. O'Connor and colleagues showed that uniaxial strain induces chain alignment in Regioregular Poly(3-hexylthiophene) (rr-P3HT), enhancing in-plane π–π interactions and increasing crystalline order [128]. Even modest alignment improved the structural coherence of the polymer domains and facilitated more efficient charge transport. Complementary work demonstrated that face-on oriented P3HT crystallites provide particularly favourable pathways for in-plane transport due to their tighter stacking and longer effective conjugation length [129]. Although these results were obtained for neat rr-P3HT films, they provide a clear basis for understanding how low tensile strain may enhance mobility within the BHJ.

In P3HT:PCBM blends, the response to strain involves a more intricate interplay between crystalline and amorphous regions. The morphology consists of semi-crystalline P3HT fibrils embedded in an amorphous polymer–fullerene matrix. Under tensile deformation, crystalline segments can rotate or reorient, while the amorphous domains reorganize to accommodate the applied load. Strain can also modify the level of phase mixing in the D–A network. Partial chain alignment may promote deeper PCBM penetration into P3HT-rich regions in some locations, while simultaneously enhancing P3HT aggregation elsewhere [17, 95]. These competing effects

reshape the nanoscale transport pathways. Even a modest increase in the P3HT aggregate fraction has been shown to significantly reduce the reduced Langevin recombination coefficient ζ and strengthen charge separation at the CT interface [130]. Because ζ is highly sensitive to morphology, these observations provide a direct link between mechanical deformation and changes in recombination dynamics.

At higher tensile strain, microcracks begin to form within the BHJ. These defects are distinct from the catastrophic fractures observed in metallic electrodes or brittle transport layers. Microcracks in the active layer are often narrow and distributed, but they distort the local electric field and interrupt electron and hole percolation pathways. As a result, they cause reductions in J_{sc} and FF, driven by higher effective series resistance and local transport bottlenecks. Such behaviour typically emerges only once the deformation exceeds the reversible regime. At lower strain, morphological adjustments remain elastic or mildly plastic and may even persist beneficially after release, consistent with in-situ measurements on strained OSCs [38].

The link between strain, polymer orientation, and recombination becomes clearer in studies examining band-offset modulation. Ab initio calculations and scanning ultrafast electron microscopy have shown that tensile strain slightly increases the energy offset between the P3HT HOMO and the PCBM LUMO [29, 30]. This shift suppresses certain non-radiative decay pathways and can increase V_{oc}. At the same time, improved polymer ordering reduces recombination losses and enhances charge extraction, which can compensate for the small reduction in optical absorption associated with the widened effective bandgap. These combined effects explain why mild tensile strain often results in higher V_{oc} and FF, while J_{sc} remains stable or slightly improved.

3.1.3 Gaps identified

Research on strain-dependent behaviour in OSCs has expanded significantly, and device-level studies consistently report two regimes of response. Moderate tensile or bending strain is often associated with improvements in J_{sc}, V_{oc}, FF, and PCE, whereas larger deformation leads to cracking, delamination, and performance degradation. At the same time, molecular- and nanoscale investigations demonstrate that mechanical strain modifies chain orientation, crystallinity, aggregate fraction, and energy-level alignment in conjugated polymer D–A systems [29, 30]. These studies establish that mechanical deformation alters both morphology and electronic structure within the BHJ. However, they predominantly probe localized or molecular-

scale phenomena. How these strain-induced material level changes translate into the electrical response of full thin films and operating devices remains insufficiently resolved.

A central gap therefore lies in connecting these material level insights to device level behaviour. Drift–diffusion models accurately describe unstrained OSCs but lack a framework for incorporating strain-induced changes in morphology, energetics (i.e., energy level alignment and density of states), or recombination. Mechanical modeling, typically based on FEM, captures stress and strain distributions in multilayer stacks but remains disconnected from optical and electrical descriptions. As a result, strain-induced enhancements observed experimentally cannot be quantitatively linked to specific material level changes using existing modeling approaches.

An additional limitation arises from the cumulative nature of device level measurements. Mechanical deformation simultaneously affects the flexible substrate, electrodes, transport layers, and the BHJ. Changes in optical interference, series resistance, electrode microstrain, or interfacial stress redistribution can all influence the measured electrical response. Without isolating the contributions of individual layers, it remains difficult to determine how much of the observed strain response originates from the active layer itself.

Finally, the strain-dependent optical and spectroscopic response of individual layers remains insufficiently characterized under device-relevant conditions. Flexible substrates such as PET exhibit their own strain-dependent optical and molecular behaviour, while conjugated polymers such as P3HT show measurable changes in absorption, bandgap, and vibrational signatures when strained. These effects have been explored primarily in isolated films or simplified model systems. A more systematic, layer resolved understanding is therefore required to interpret device level measurements and to provide physically meaningful inputs for strain-aware models.

3.2 PET as a Mechanically Active Flexible Substrate

PET is one of the most widely adopted polymer substrates in flexible and roll-to-roll processed organic electronics. Its combination of high optical transmission in the visible range, chemical stability, low cost, and compatibility with large-area coating makes it a default choice for flexible organic solar cells, organic field-effect transistors, and related optoelectronic systems [27, 131–133]. In such devices, PET typically forms the mechanically dominant layer in the stack. It defines the overall bending stiffness, constrains the strain profile experienced by the functional films,

and is the first medium that interacts with incident light before it reaches the active semiconductor [63, 134]. As a result, the substrate cannot be regarded as a passive mechanical support. Its response to deformation directly conditions both the mechanical reliability and the useful optical throughput of the device.

From a mechanical perspective, PET exhibits a characteristic progression from elastic response at low strain to yielding, strain hardening, and eventual damage at larger deformation, with the details depending on strain rate, temperature, and prior processing history [119, 135–137]. During cold drawing or tensile loading in the solid state, molecular chains rotate and align along the loading direction, which gives rise to anisotropic stiffness and an evolving distribution of amorphous, mesomorphic, and crystalline regions [138–140]. In multilayer flexible electronics, this evolution is important because the substrate stores and redistributes the applied mechanical energy. The strain experienced by brittle or semi-brittle layers, such as transparent electrodes or conjugated polymer films, does not directly equal the externally applied strain. It is also shaped by the nonlinear and history-dependent mechanical response of the PET substrate itself. In strained organic solar cells, key failure modes correlate more strongly with the substrate's mechanical history than with intrinsic material limits. [37, 63, 141].

The molecular rearrangements that determine PET's mechanical response also influence its optical properties. Chain alignment and density fluctuations can modify birefringence, dichroism, and scattering. These effects become pronounced when strain drives the material toward mesophase or partially crystalline states [124, 138, 142, 143]. Because PET lies optically in front of the photoactive or charge transport layers, any strain-induced change in transmittance, refractive index, or anisotropy directly affects how light is delivered into the device interior [27, 131]. For this reason, PET in flexible electronics must be regarded as a mechanically active and optically consequential component. Its coupled mechanical and optical behaviour under realistic deformation conditions forms the basis for the spectroscopic studies reviewed in the following subsections.

3.2.1 Optical spectroscopy under strain

Mechanical stretching induces well-defined optical signatures in PET because the polymer's microstructure evolves toward a more oriented state. Ellipsometry on biaxially drawn films shows that even moderate deformation produces measurable anisotropy in the dielectric function, requiring separate responses along and perpendicular to the draw direction [142]. In the UV–visible range, where PET hosts electronic transitions of the carbonyl and aromatic units, the relative strength and

polarization sensitivity of these bands change with stretching. These variations arise from the reorientation of transition dipoles as chain segments align, and they reflect the gradual development of microstructural order under strain. The emergence of optical anisotropy coincides with the mechanical stiffening that arises from polymer chain alignment [142].

Vibrational spectroscopy provides complementary evidence for this evolution. Infrared measurements on stretched PET reveal polarization-dependent changes in the intensities of backbone and ester-related modes. These reflect the rotation of both crystalline and amorphous segments toward the stretching axes [138, 142]. Orientation distribution analyses confirm that biaxial drawing increases the fraction of chain segments lying parallel to the film plane, while simultaneously narrowing their angular distribution. These structural changes do not significantly alter PET's visible transparency, but they do modify how the film absorbs and polarizes mid-infrared radiation [138].

Raman scattering further illustrates how local symmetry and chain conformation evolve under load. Polarized Raman studies show systematic variations in the intensities of aromatic ring and carbonyl modes as the scattering geometry is rotated relative to the draw direction. This behaviour is a signature of increased molecular alignment and enhanced local ordering induced by strain. Considering that the Raman selection rules are sensitive to the orientation of polarizable units, these measurements reveal subtle differences between amorphous and more ordered regions that form during stretching [124].

3.2.2 Strain-Induced Molecular Rearrangement at Elevated Strain

Mechanical loading of PET does not simply stretch the macroscopic film; it drives a cascade of irreversible molecular rearrangements that alter both the mechanical state of the substrate and its optical response. At low strain, chain segments primarily undergo affine rotation and limited straightening, and the optical effects are small. Beyond a threshold—typically a few percent depending on thermal history—deformation begins to reorganize the semicrystalline architecture in ways that do not fully relax upon unloading [138].

In this region, PET develops a progressively anisotropic microstructure. Chain segments in the amorphous phase orient toward the loading direction, mesophase regions grow, and existing crystallites undergo rotation and limited reorganization. Stress promotes densification of certain domains and expansion of others, yielding

a heterogeneous distribution of molecular environments. Bin *et al.* showed that these orientation processes are only partially reversible. Once polymer chains rotate or become partially aligned under strain, back-relaxation upon unloading is incomplete. As a result, a residual preferred orientation remains, along with a modified balance between amorphous and more ordered fractions [138].
These microstructural changes alter the optical response. Strain driven ordering affects birefringence, dichroism, and the directional dependence of the refractive index. Zhou *et al.* observed that even moderate deformation produces a measurable rotation of the optical axis and an increase in stress induced birefringence that does not fully recover after the strain is released [143]. Similar partial irreversibility was identified by Laskarakis *et al.*, who reported that deformation modifies the dielectric tensor of PET in a manner consistent with increased chain alignment and the emergence of additional optically anisotropic domains [142].
Although the details of these rearrangements are determined by processing history, temperature, and strain rate, a consistent picture emerges, showing that PET accumulates a strain-dependent optical memory.

3.2.3 Gap Identified

While PET has been widely characterized mechanically and optically, a unified quantitative understanding of its response to moderate, device-relevant strain remains lacking. In particular, the combined optical response under such conditions has not been systematically resolved. Raman studies tend to focus on angular anisotropy or high-strain crystallization effects. Consequently, subtle spectral changes within the low-strain regime are often overlooked. Optical measurements reveal strain-induced anisotropy. However, these approaches are frequently disconnected from molecular-level vibrational information and are rarely applied across controlled, systematic strain series relevant to flexible optoelectronics [27, 131].
As a result, no prior study has linked macroscopic optical behaviour measured by UV–Vis spectroscopy with microscopic structural changes accessed by Raman spectroscopy. This gap is particularly evident under small to moderate tensile strains. Such strain levels are routinely imposed in flexible electronic devices. Most available reports focus on strain levels far beyond operational conditions or address deformation-induced crystallization rather than optical shifts. Others examine UV–Vis and Raman responses in isolation. Consequently, the field lacks a strain-resolved optical framework capable of describing how PET's electronic absorption and vibrational symmetry evolve simultaneously under realistic deformation.
The absence of such an integrated analysis motivates the study performed in this the-

sis. Here, we combine controlled mechanical deformation with synchronized UV–Vis and Raman spectroscopy. This approach enables quantification of PET's strain-dependent optical response within the operational strain window of flexible and stretchable organic electronic systems.

The strain-dependent optical behaviour of PET sets the boundary conditions for any thin semiconductor film deposited on top of it. As Section 3.2 showed, PET does not simply transmit applied deformation. Its molecular alignment, birefringence, and density changes, reshape how light enters the device stack and how strain is redistributed across the functional layers. In practical flexible devices, this means that any apparent optical or electronic change in a conjugated polymer film must be interpreted in the context of a substrate whose properties evolve under load.

These coupled effects raise an important question. To what extent do conjugated polymers themselves exhibit intrinsic bandgap modulation under mechanical strain, independent of substrate-induced optical changes? Section 3.3 addresses this point by reviewing prior studies on strain-dependent absorption and energy level shifts in conjugated polymer thin films and assessing their relevance to realistic deformation conditions in flexible organic electronics.

3.3 Experimental Studies of Optical Bandgap Under Mechanical Deformation

Mechanical strain can perturb the electronic structure of conjugated polymers, and several experimental approaches have attempted to capture these changes at different spatial and temporal scales. Nanoscale insight into such perturbations has been provided by scanning ultrafast electron microscopy, where localized mechanical deformation was shown to alter the excitonic response of semiconducting polymer domains on sub-picosecond timescales [30]. In these measurements, transient spatial modulations in the effective bandgap of P3HT aggregates emerged following the introduction of a strain field. These observations demonstrate that tensile deformation can perturb local packing and modify the exciton dissociation landscape. Although highly localized and inherently transient, these observations revealed the intrinsic sensitivity of conjugated polymer electronic states to mechanical perturbation. Complementary studies at the device scale have focused on macroscopic bending or stretching of polymer thin films. Here, changes in optical absorption are often subtle and intertwined with mechanical relaxation. This behaviour is consistent with broader reports showing that moderate strain primarily influences chain orientation, lamellar ordering, and crystallinity, while leaving the steady-state

absorption edge largely intact [28]. Together, these findings suggest that polymer electronic structure can be modulated by mechanical forces, but that observable changes in thin-film absorption, depends sensitively on the spatial and temporal characteristics of deformation.

A complementary perspective on strain–bandgap coupling arises from theoretical work that isolates the molecular and interfacial origins of energetic shifts. Menichetti and co-workers used density functional theory to examine how tensile deformation affects the HOMO and LUMO levels of P3HT chains and the corresponding band offsets at a P3HT/PCBM interface [29]. Their calculations showed that mechanical strain perturbs backbone geometry, modifies π-orbital overlap, and shifts D–A energy alignment. Although the predicted energetic variations were modest, the results clarified a mechanistic route by which tensile deformation could influence exciton separation and photovoltage. Importantly, these predictions were obtained for isolated chains and idealized interfaces, indicating that molecular scale strain effects are fundamentally accessible but may not directly translate to thin-film behaviour, where intermolecular packing, semicrystalline texture, and substrate constraints govern the overall response.

Mechanically induced bandgap modulation has also been documented in small molecule organic crystals, where the response to strain is more pronounced. Studies on rubrene and pentacene crystals have shown that uniaxial compression or tension reorganizes intermolecular spacing and alters frontier orbital coupling, resulting in measurable shifts in optical absorption and photoluminescence. These systems exhibit strong electron lattice interactions and highly anisotropic packing, which amplify the effect of mechanical deformation on their electronic structure. These observations underscore the intrinsic ability of organic semiconductors to undergo strain-dependent bandgap modulation. However, the crystalline architecture of these materials differs substantially from that of conjugated polymer thin films. In particular, conjugated polymers exist in a semicrystalline, structurally disordered environment that is not captured by highly ordered model systems. Their behaviour thus provides mechanistic insight but cannot be directly extrapolated to technologically relevant polymer systems processed on flexible substrates [28].

In thin conjugated polymer films, experimental reports examining absorption changes under macroscopic bending or stretching generally reveal only minor modifications to the spectral profile. The absorption onset is often preserved within experimental uncertainty, even though deformation can influence chain alignment and aggregate structure [28]. This behaviour is consistent with the moderate conformational flexibility of polymer backbones and the ability of semicrystalline domains to redistribute

strain without undergoing major electronic reconfiguration.

3.3.1 Limitations of prior work

The studies outlined above establish that mechanical deformation can perturb the electronic structure of organic semiconductors, yet they do so under conditions that differ substantially from those encountered in semicrystalline conjugated polymer thin films used in practical photovoltaic devices. A major fraction of the literature focuses on highly ordered or crystalline systems. Studies on rubrene and pentacene probe either single crystals or well-oriented thin films on rigid substrates [144, 145]. These highly controlled model platforms are valuable for isolating fundamental strain–electronic-structure coupling, but they do not capture the microstructural heterogeneity or thin-film confinement present in semicrystalline donor polymers.

A second limitation is that much of the existing work concerns transient or highly idealized perturbations. Scanning ultrafast electron microscopy resolves femtosecond to nanosecond modulation of band edge energetics under pulsed excitation rather than residual strain states [30]. Density Functional Theory (DFT) studies typically compute band edge shifts for static configurations of short repeat units without accounting for the distribution of chain conformations, side chain disorder or morphological defects that are characteristic of thin films [29]. The Work Function (WF) measurements on rubrene demonstrate that elastic and plastic strains can strongly modify the electronic landscape of an organic crystal [144]. However, these measurements do not involve conjugated polymer chains or semicrystalline morphologies typical of OSC donor layers.

There is also a geometry and substrate mismatch. Many strain-dependent studies employ rigid substrates such as silicon or glass, where deformation is introduced through thermal expansion mismatch or controlled bending [144, 145]. In contrast, polymer semiconductor thin films used in flexible photovoltaics are deposited on compliant substrates such as PET. Here the strain field is governed by polymer–substrate adhesion, film thickness and semicrystalline microstructure. Broader mechanical studies of conjugated polymers focus on stiffness, yielding and ductility, sometimes using molecular dynamics simulations to quantify chain reorientation or backbone deformation under stress [146]. These works provide important insights into deformation mechanisms but do not measure optical absorption or extract an optical bandgap under load.

3.3.2 Gap identified

Taken together, the limitations discussed in subsection 3.3.1 reveal a clear and unresolved gap in the current literature. While prior studies establish that mechanical deformation can influence electronic structure at the molecular or crystalline scale, no work has systematically examined the stability of the optical bandgap in semicrystalline conjugated polymer thin films under controlled tensile strain.
This absence is particularly significant for donor polymers used in flexible organic photovoltaic devices. In these systems, moderate uniaxial strain is intrinsic to operation. The resulting optoelectronic response emerges from a heterogeneous microstructure rather than from a well-defined crystalline lattice. As a result, it remains unclear whether the optical bandgap of a technologically relevant polymer thin film remains invariant under strain or undergoes measurable modification within experimentally accessible deformation regimes.
Addressing this gap requires direct, strain-resolved optical characterization of semicrystalline conjugated polymer thin films deposited on flexible substrates, using a reproducible and quantitative band-gap extraction methodology. Such an investigation is necessary to establish the degree of band-gap stability that can be expected in flexible organic electronic applications.

3.4 Raman Spectroscopy of Conjugated Polymers Under Strain

Raman spectroscopy is widely employed as a structure-sensitive probe for conjugated polymers because the vibrational modes of the π-conjugated backbone are directly coupled to molecular geometry and electronic delocalization. In polythiophene-based systems, several prominent Raman-active modes originate from in-plane skeletal motions of the conjugated backbone. The frequencies and linewidths of these modes respond sensitively to changes in backbone planarity, torsional disorder, and effective conjugation length. As a result, Raman spectra encode information not only about chemical identity but also about the degree of molecular order and alignment within thin films, making the technique particularly suitable for studying structurally heterogeneous polymer semiconductors [147].
Systematic studies have established quantitative correlations between specific Raman modes and the underlying structural state of conjugated polymer films. In P3HT, the C–C and C=C stretching modes in the 1300–1500 cm^{-1} range have been shown to shift and narrow as molecular order and π-electron delocalization increase,

reflecting enhanced backbone planarity and interchain packing [93]. More recent work has generalized this interpretation by demonstrating that Raman signatures track changes in electronic delocalization across a broad class of polythiophene-based systems. This reinforces the view that Raman shifts should be understood as probes of conjugation and electronic structure rather than simple bond-stiffness variations [148]. At the same time, studies of chemically doped P3HT have clarified that electronic reorganization alone can also modify Raman line shapes, highlighting the need for physically informed interpretation when using Raman spectroscopy to infer structural order [149]. Collectively, these works establish Raman spectroscopy as a powerful and nuanced tool for monitoring alignment, conjugation, and molecular order in conjugated polymer thin films.

3.4.1 Existing strain-dependent Raman studies in conjugated polymers

Raman spectroscopy has been employed in a limited but informative set of studies to investigate how mechanical deformation alters the molecular structure of conjugated polymers. Early work in this area largely focused on identifying whether tensile strain could induce backbone alignment or modify electronic conjugation, rather than providing a comprehensive picture of strain accommodation in realistic thin-film geometries. As a result, the existing literature remains fragmented across different material systems, deformation regimes, and experimental configurations.

Several studies have reported strain-induced Raman shifts in P3HT and closely related conjugated polymers, often interpreting these shifts in terms of backbone planarization or loss of effective conjugation. Computational and model-system investigations on P3HT oligomers and MEH-PPV under uniaxial stretching showed that small elongations along the polymer backbone can alter frontier orbital localization and vibrational frequencies, whereas larger deformations rapidly lead to electronic localization and degradation of optoelectronic properties [150]. While these results are mechanistically insightful, they are obtained under idealized stretching conditions at the single-chain or oligomer level and therefore do not directly capture the heterogeneous deformation pathways operative in semicrystalline thin films.

Experimentally, Raman studies on strained conjugated polymer films have demonstrated that the dominant backbone modes, particularly the C–C and C=C stretching vibrations, respond measurably to tensile loading. In P3HT-based systems, changes in the linewidth and position of modes in the 1300–1500 cm^{-1} range have been associated with evolving backbone torsion and effective conjugation length [151]. However, many of these experiments were performed either on as-cast films,

on pre-stretched elastomeric substrates, or under deformation conditions optimized for stretchability rather than structural analysis [63]. While such configurations are valuable for identifying macroscopic crack onset and device failure, they conflate intrinsic molecular response with substrate-dominated mechanics and do not isolate how strain is accommodated within semicrystalline P3HT domains themselves.

More recent work has extended Raman analysis to donor–acceptor and DPP-based polymers, revealing that strain can produce qualitatively different spectral responses depending on backbone rigidity and crystallinity. In these systems, modest strain levels may induce small, reversible Raman shifts consistent with elastic deformation, whereas higher strain leads to pronounced linewidth broadening indicative of heterogeneous microstrain and defect formation [152]. Importantly, these studies show that Raman signatures associated with increased order and those arising from mechanical damage can overlap spectrally, underscoring the need for careful interpretation of strain-induced redshifts and linewidth changes. These findings are general to conjugated polymers and are not specific to P3HT, but they highlight a key limitation of attributing Raman shifts solely to backbone planarization.

A small number of studies have begun to exploit spatially resolved Raman measurements to visualize mechanical heterogeneity under strain. Raman mapping experiments on stretched conductive polymer films have revealed that strain-induced spectral changes are often highly localized. These changes correlate with crack initiation sites, interfacial delamination, or regions of strain concentration near defects [151]. Together, these observations demonstrate that Raman spectroscopy can act as a local probe of mechanical heterogeneity. However, existing studies typically focus on identifying damage or failure. They do not systematically quantify how molecular order evolves as a function of strain, temperature, and processing history. Moreover, these studies are generally conducted under a single thermal condition, limiting their relevance to processing dependent microstructural evolution.

Raman investigations that explicitly consider how thermal processing history conditions the molecular response to mechanical strain remain particularly rare. Existing Raman studies of P3HT have established that thermal annealing alone narrows backbone Raman modes and shifts the C=C stretch to lower wavenumber as crystallinity and π-electron delocalization increase [93]. Separately, chemically or electronically induced reorganization, such as molecular p-doping, has been shown to modify Raman line shapes through electronic effects without necessarily improving structural order [149]. However, these insights have not been systematically integrated into strain-dependent Raman studies, leaving open the question of how thermal history modifies the molecular response of P3HT under mechanical load.

Taken together, the existing literature demonstrates that Raman spectroscopy is sensitive to strain-induced changes in conjugated polymers, but it also reveals substantial gaps. Most studies examine either strain or temperature in isolation, focus on single-layer films, and rely on qualitative interpretations of Raman shifts without disentangling elastic alignment from irreversible microstructural damage. For P3HT in particular, there is no comprehensive Raman study that evaluates how processing temperature, strain magnitude, and interfacial mechanics collectively govern backbone order and mechanical stability. This limitation directly motivates a more systematic investigation of strain–temperature interplay in device-relevant P3HT stacks.

3.4.2 Limitations of prior works

While strain-dependent Raman spectroscopy has yielded important qualitative insights into how conjugated polymers respond to mechanical deformation, the existing body of work remains limited in its ability to isolate and interpret specific deformation mechanisms in device-relevant thin films. These limitations do not imply that prior studies are incomplete or flawed in isolation. Rather, they reflect a set of recurring methodological simplifications that restrict the physical questions that can be addressed simultaneously. As a result, current Raman studies tend to illuminate individual aspects of strain response, without resolving how these aspects interact within realistic processing and device contexts.

A central limitation is the widespread separation of mechanical strain from thermal processing history. In many computational and model-based studies, strain is applied to idealized molecular backbones or small oligomers whose geometry does not reflect the semicrystalline morphology established during film formation [150]. In parallel, experimental Raman studies have demonstrated that thermal annealing alone can substantially modify backbone planarity, conjugation length, and spectral linewidths in P3HT [93], yet these thermally conditioned microstructures are rarely examined under subsequent mechanical load. Consequently, it remains unclear how strain-induced molecular reorganization depends on whether the polymer network is initially soft and heterogeneous or rigidified by prior thermal ordering.

A recurring limitation concerns the mechanical context within which strain-dependent Raman measurements are interpreted. While Raman studies themselves are typically performed on rigid or semi-rigid substrates to ensure optical and mechanical stability, a substantial body of mechanical and device level literature demonstrates that substrate compliance strongly influences how strain is transmitted to

conjugated polymer films [63]. In elastomer-supported systems, such as those based on PDMS, a significant fraction of the applied deformation is accommodated by the substrate through elastic and viscoelastic relaxation, leading to non-uniform and non-affine strain transfer to the semiconducting layer. Although Raman spectroscopy is rarely applied directly in these elastomeric configurations, the associated mechanical behaviours are well established. They underscore that the strain experienced by a polymer backbone can differ markedly from the nominal macroscopic strain [126]. This insight has important implications for Raman based studies conducted on stiffer substrates. In such cases, strain-induced spectral changes must be interpreted within the specific mechanical regime defined by the substrate, interface, and film morphology. Without explicitly accounting for these factors, comparisons across studies performed under different mechanical boundary conditions remain inherently ambiguous.

Interpretation of Raman spectral changes under strain presents an additional challenge. Similar shifts in band position or changes in linewidth can originate from fundamentally different physical processes, including elastic backbone alignment, increased torsional disorder, electronic localization, or the formation of microstructural defects [152]. This ambiguity is compounded by evidence that purely electronic modifications, such as those induced by chemical doping, can alter Raman line shapes in ways that resemble signatures of increased structural order [149]. Without systematic control over processing history and mechanical environment, Raman spectra alone do not provide an unambiguous distinction between reversible alignment and irreversible damage.

Finally, most existing studies do not explicitly discriminate between in-situ strain response and residual structural changes after strain release. Raman measurements are typically reported either under applied load or after deformation, but rarely tracked continuously across loading and unloading [151]. This limits insight into whether observed spectral changes correspond to transient conformational adjustments or to permanent microstructural reorganization. For flexible electronic applications, where repeated deformation and mechanical fatigue are critical concerns, this distinction is particularly important.

Taken together, these considerations indicate that current strain-dependent Raman studies address isolated facets of polymer deformation rather than their combined influence. In particular, the simultaneous roles of thermal processing history, strain magnitude, interfacial mechanics, and reversibility have not been examined within a single experimental framework. Clarifying how these factors interact is therefore essential for interpreting Raman signatures of strain in conjugated polymer thin

films and for assessing their mechanical reliability in flexible device architectures.

3.4.3 Gap identified

The existing Raman literature demonstrates sensitivity to both thermal processing and mechanical deformation in conjugated polymers, but these effects have largely been examined in isolation. Strain-dependent Raman studies typically probe mechanical deformation without explicit control over prior microstructural conditioning. Thermal-ordering studies, in contrast, rarely extend their analysis to subsequent mechanical loading [93, 151, 152]. In parallel, model-based approaches often impose strain on idealized backbones that do not capture the semicrystalline morphology of processed thin films [150]. As a result, it remains unresolved how strain-induced Raman signatures depend on the thermally established mechanical state of the polymer network.

A further unresolved aspect concerns the role of interfaces and supporting substrates in conditioning the molecular response to strain. Mechanical and device-level studies have demonstrated that substrate compliance and interfacial coupling strongly influence how deformation is transmitted to organic semiconductor layers [63]. However, this insight has not been systematically integrated into Raman-based analyses of strain. Without explicitly considering interfacial layers and multilayer stacks, it remains difficult to assess how molecular scale Raman signatures relate to the actual mechanical environment experienced by the active polymer layer in flexible devices.

The interpretation of strain-induced Raman spectral changes is further complicated by the fact that similar shifts in peak position or linewidth can arise from distinct physical mechanisms. Elastic backbone alignment, increased torsional disorder, electronic localization, and the formation of microstructural defects can all produce overlapping spectral signatures [152]. This ambiguity is reinforced by evidence that purely electronic reorganization, such as molecular p-doping, can modify Raman line shapes in ways that resemble signatures of increased structural order [149]. Without systematic control over both processing history and mechanical boundary conditions, Raman spectra alone cannot unambiguously distinguish reversible molecular rearrangement from irreversible damage.

Finally, most previous studies do not explicitly discriminate between in situ strain response and residual structural changes after strain release. Raman measurements are typically reported either under applied load or after deformation, but rarely tracked continuously across loading and unloading cycles [151]. This limits insight into whether observed spectral changes reflect transient conformational adjustments or permanent microstructural reorganization. For flexible electronic applications,

where repeated deformation and mechanical fatigue are central reliability concerns, this distinction remains largely unexplored.

Taken together, these gaps indicate that the combined influence of thermal processing history, strain magnitude, interfacial mechanics, and reversibility on the Raman response of P3HT thin films has not been examined within a single, coherent experimental framework. Addressing this gap is essential for establishing a physically grounded interpretation of strain-dependent Raman signatures in conjugated polymer semiconductors and for linking molecular-scale observations to mechanical stability in flexible device architectures.

Chapter 4

Methodology and Experimental Framework

4.1 Introduction to Methodological Approach

The methodological approach adopted in this thesis is motivated by a central limitation in the existing literature: although strain-dependent optical and electrical properties have been extensively studied, the applied deformation schemes and material systems often differ substantially from those experienced in fabricated OSCs. This limits both the interpretation of experimental observations and the predictive capability of device-scale models.

Beyond this conceptual gap, an additional limitation emerges when strain effects are treated within a modeling framework. As an initial step, a physics-based FEM framework was developed in COMSOL Multiphysics [153]. The model was used to examine how strain-induced morphological alterations in the active layer translate into changes in device-level optoelectronic performance. It combined full-wave optical simulations with a drift–diffusion electrical description of a benchmark P3HT:PCBM architecture. This enabled systematic evaluation of performance sensitivity to electronically meaningful surrogate parameters. In this approach, mechanical strain was not introduced as an explicit mechanical field. Instead, its experimentally inferred consequences were represented through controlled modulation of key electrical descriptors, namely the effective bandgap E_g and the reduced Langevin recombination prefactor ζ.

Within this modeling framework, it became evident that quantitative strain-dependent material parameters are required to constrain and validate such simulations. These parameters are largely unavailable under realistic processing and deformation conditions. To address this operational limitation, the methodology was therefore

extended to targeted experimental characterization at the material level. The focus was placed on isolating and quantifying strain-induced responses in representative constituent materials. Specifically, this work investigates P3HT, a widely used benchmark photoactive polymer, and PET, a common flexible substrate material. Together, these materials capture the essential optical and mechanical roles present in flexible OSC architectures while enabling controlled and interpretable analysis.
The selection of PET and P3HT was further motivated by their status as important reference materials within the flexible organic electronics community. While recent research increasingly explores more chemically complex or engineered semiconductors, the use of well-established materials provides a critical methodological advantage for foundational investigations. Their optical signatures, vibrational modes, and structure–property relationships are extensively documented under unstrained conditions. This enables the strain-induced deviations to be identified and interpreted with minimal ambiguity. This methodological choice prioritizes interpretability and mechanistic clarity over material novelty. By establishing strain–response relationships in benchmark systems, the present work aims to construct a transferable reference framework that can be systematically extended to emerging materials and more complex device architectures. The emphasis on canonical materials further ensures that observed strain-induced phenomena can be directly contextualized within the broader literature, facilitating meaningful comparison, reproducibility, and cross-study validation.
Mechanical deformation was applied in the form of uniaxial tensile strain. Although more complex loading modes—such as biaxial deformation, cyclic fatigue, or bending—are relevant to real-world applications, uniaxial strain provides the most direct and physically interpretable framework for establishing baseline strain property relationships. In the absence of comprehensive material level data, this approach enables strain-induced optical and structural changes to be attributed unambiguously to deformation along a single axis, thereby forming a necessary foundation for subsequent studies involving more complex mechanical configurations.
All measurements were conducted at room temperature. This choice reflects both practical operating conditions and application relevance, particularly for indoor and low-power IoT photovoltaic systems. In these applications, OSCs are expected to operate without thermal activation. By avoiding elevated temperatures, the methodology isolates mechanically driven effects. This approach prevents convolution with thermally induced relaxation or morphological reorganization. As a result, strain-induced responses are examined in a regime directly relevant to the intended applications.

This chapter details the experimental implementation of this methodology through complementary spectroscopic techniques applied under controlled mechanical strain, enabling systematic investigation of strain-induced optical and molecular-level transformations in each material.

4.2 Rationale for Spectroscopic Methodologies

The UV–Vis absorption and Raman spectroscopy were chosen as the primary experimental techniques in this thesis. This choice is rooted in their distinct yet highly complementary capabilities for probing different facets of material response in both individual films (e.g., PET) and stacked layers (e.g., PET/P3HT, and PET/PEDOT:PSS/P3HT):

- **UV–Vis Spectroscopy** was selected for its ability to quantitatively assess changes in the optical transmission and absorption characteristics of films. For substrates like PET, and equally for photoactive layers like P3HT, maintaining optical fidelity under strain is crucial for maximizing light transmission and absorption within the device. UV–Vis absorption spectroscopy directly reveals how strain impacts the material's electronic structure, leading to observable shifts in absorption bands or changes in overall transparency. These changes directly translate to variations in light harvesting efficiency for optoelectronic applications. This technique offers a straightforward and rapid method for initial assessment of these macroscopic optical changes.

- **Raman Spectroscopy**, in contrast, was chosen for its unparalleled capability to provide molecular level structural and conformational information. By analyzing the shifts, broadening, and intensity changes of specific vibrational modes, Raman allows for direct inference about alterations in bond lengths, backbone planarity, effective conjugation length, and intermolecular packing. This detailed molecular insight is crucial for elucidating the underlying mechanisms responsible for any observed optical changes and understanding how strain propagates through the material at an molecular scale. Crucially, the ability to perform in-situ Raman measurements while the sample is under applied strain was a decisive factor, enabling real-time observation of dynamic molecular responses and avoiding relaxation effects inherent to ex-situ measurements.

The synergistic application of these two techniques is therefore pivotal: UV–Vis

identifies what changes occur at the macroscopic optical level (e.g., reduced transparency, altered bandgap), while Raman provides the molecular level understanding of why those changes occur (e.g., specific conformational rearrangements, altered crystallinity, or molecular alignment). This dual modality approach is essential for establishing a robust correlation between macroscopic device performance and microscopic material behaviour under mechanical stress. This is a core objective of this thesis. The effectiveness and insights gained from employing these techniques in related prior studies involving P3HT and PET further reinforced their selection for this comprehensive investigation.
Furthermore, practical constraints within the laboratory environment significantly influenced the experimental approach. Consequently, an ex-situ UV–Vis approach was adopted for both PET and P3HT-based samples. This strategy enabled the characterization of persistent optical modifications. It also allowed residual, strain-induced changes to be identified after mechanical relaxation. By contrast, the in-situ capability of the Raman spectrometer enabled real-time monitoring of molecular dynamics during strain application. This proved invaluable. This capability directly supported the thesis objective of probing strain-induced physical mechanisms. The custom-built stretcher device accommodated both ex-situ UV–Vis absorption spectroscopy and in-situ Raman measurements. This design allowed instrumental limitations to be managed while maintaining consistent experimental objectives across all materials. As a result, key material-level insights into strain-induced optical and structural transformations were obtained reliably.

4.3 Design and Implementation of a Custom Mechanical Strain Device

Precise control over mechanical deformation is paramount for understanding strain-induced phenomena in flexible electronic materials. To enable systematic investigations of both optical and molecular transformations under controlled uniaxial tensile strain, a custom-built mechanical stretching device was designed and fabricated. This device serves as a critical experimental platform, facilitating the application of well-defined and repeatable strain profiles to thin polymer films, and crucially, allowing for direct integration with advanced spectroscopic measurement techniques. The mechanical backbone of the custom stretcher is an industrial-grade RATTMMOTOR ZBX80 Computer Numerical Control (CNC) Linear Guide Actuator (Model: ZBX80), specifically selected for its inherent precision and robust construction. Fabricated from high-strength aluminum alloy with an anodized surface, this linear stage

ensures structural integrity and minimal friction during operation. The actuator features an effective stroke length of 400 mm, providing ample range for the applied tensile strain. Its motion is precisely actuated by an SFU1605 ball screw, characterized by a 16 mm diameter and a 5 mm pitch, integrated with a flange thread nut. The moving carriage is supported by a double linear rail construction, further enhancing the mechanical stability, wear resistance, and smooth operation critical for high-resolution spectroscopic measurements. The design incorporates M5 mounting holes on its sides and bottom, offering versatile integration points for various components. The total length of the linear drive, including its integrated motor, is 630 mm, with a base plate length of 519 mm, providing a compact yet robust platform for mechanical testing.

To securely hold the polymer sample during tensile deformation, a custom clamping system was constructed and mounted atop the linear actuator base and its moving stage. Two parallel steel clamping edges were rigidly fixed to the linear actuator components, ensuring stable and repeatable positioning. The polymer film was inserted between these two clamping edges, with a well-defined free gauge length exposed between the clamps. To prevent slippage of the polymer film under applied load, detachable rough-textured black anodized aluminium inserts were placed between the inner faces of the clamps and the sample surface, providing high static friction and promoting uniform strain transfer across the gauge length.

The actuation system is powered by a National Electrical Manufacturers Association (motor frame standard) (NEMA)23 stepper motor (57 mm frame size), integrated directly into the linear guide. This specific motor operates with a fundamental step angle of 1.8° (200 full steps per revolution) and is rated for a current of 2.8 A, delivering a holding torque of 1.26 N·m. Control of this stepper motor is managed by a Twotrees TB6600 stepper motor driver, an improved version designed for bipolar stepper motors. This driver accepts a Direct Current (DC) input voltage ranging from 9 V to 42 V and provides an adjustable output current, configured in this setup to 2 A. Crucially for fine strain control, the TB6600 driver is configured for 1/4 microstepping, which translates the motor's full-step resolution into finer angular increments. This configuration yields a precise linear displacement of 6.25 μm per microstep (calculated as 5 mm/revolution divided by (200 full steps/revolution $\times$ 4 microsteps/full step) = 6.25 μm/microstep). The selected output current of 2 A ensures reliable and thermally stable operation of the NEMA23 motor, well within its rated specifications. The driver's high-speed photoelectric isolation of input signals also contributes to mitigating electromagnetic interference, a critical consideration for noise-sensitive spectroscopic measurements.

The control electronics for the strain device are centered around an ELEGOO Mega 2560 R3 Microcontroller Board, which is 100% compatible with the Arduino Integrated Development Environment (IDE). This board, based on the ATmega2560 microcontroller and interfaced via an Atmega16U2 Universal Serial Bus (USB)-to-serial converter, operates at 5 V with a 16 MHz clock frequency. It provides a rich set of digital Input/Output (I/O) pins (54, including 15 Pulse-Width Modulation (PWM) outputs) and analog input pins (16), offering ample resources for controlling the stepper driver and accommodating future sensor integration (e.g., limit switches, optical encoders). A custom-written Arduino sketch interprets serial commands transmitted from a host computer via USB, generating the precise step and direction pulses required by the TB6600 driver to actuate the linear guide. The stepper driver's enable signal is also controlled by the Arduino, allowing for active motor holding during measurements to prevent backdriving or accidental displacement. The control system operates in an open-loop configuration, where strain levels are determined solely by the commanded number of microsteps. While no limit switches were implemented, the system relies on careful manual initial positioning and precise step counting for accurate strain application. The constant linear motion of the actuator is set to a speed of 30 steps per second, resulting in a linear velocity of 187.5 μm/s, with no implemented acceleration or deceleration ramps during strain application.

A meticulous calibration procedure was performed to establish the precise relationship between commanded microsteps and applied linear displacement. This involved commanding a known number of microsteps (typically 1000) and externally measuring the resulting linear displacement using a high-precision caliper or micrometer. This experimental validation confirmed the calculated 6.25 μm/microstep displacement. The strain (ϵ) applied to the polymer films was then precisely calculated as the percentage elongation relative to the initial length (L_0) of the sample segment between the two clamping edges: $\epsilon = (\Delta L/L_0) \times 100\%$, where ΔL is the total linear displacement (number of microsteps $\times$ 6.25 μm). This calibration was repeated for various initial sample lengths to ensure consistency and robustness across different experimental conditions, guaranteeing high reproducibility and accuracy in the applied strain.

The custom mechanical strain device is integral to the experimental framework, specifically facilitating both in-situ Raman spectroscopy and ex-situ UV–Vis absorption measurements. For in-situ Raman analysis, the compact design and the double linear rail construction of the actuator minimize vibrations and ensure stable optical access, allowing the sample to remain clamped and under precisely con-

trolled strain during spectral acquisition. This capability is critical for capturing dynamic molecular responses without artifacts from stress relaxation. For UV–Vis measurements, while in-situ integration with the spectrophotometer chamber was not mechanically feasible, the stretcher's ability to precisely apply and maintain strain, followed by controlled release, enabled reliable ex-situ characterization of persistent optical modifications. This custom device, therefore, provides a highly controlled and adaptable platform, essential for correlating macroscopic mechanical deformation with the microscopic optical and molecular transformations in flexible organic electronic materials.

4.4 Sample Preparation

The study utilized two primary sample types: bare PET films and P3HT thin films spin-coated onto PET or onto PET coated with PEDOT:PSS substrates.
An industrially sourced PET roll, specifically manufactured as a transparent substrate for OSC applications, served as the base material. For experimental use, 5 cm × 5 cm pieces were precisely cut from this PET roll. To ensure optimal cleanliness, these PET pieces were thoroughly cleaned by wiping with cleanroom towels wet by a propanol and acetone mixture (3 parts propanol to 2 parts acetone), with nitrogen gun drying performed after each solution rinse.
For the preparation of P3HT-coated PET substrates, a robust adhesion layer was first established on a rigid glass support. Standard 5 cm × 5 cm glass substrates were rigorously cleaned by wiping with cleanroom cloth with the same propanol and acetone mixture, followed by nitrogen gun drying after each solution application. Subsequently, pieces of a specific thermally activated double-sided tape, also cut to 5 cm × 5 cm dimensions, were meticulously adhered to the cleaned glass substrates. The adhesion process was carefully controlled in two steps to minimize bubble formation and maximize interfacial contact. Initially, after ensuring no bubbles were present between the tape and the glass, the assembly underwent a first annealing step on a hot plate at 75°C for 5 minutes. Any forming bubbles were then carefully removed by gradually applying pressure across the sample surface using a sturdy plastic card. Following this, the substrate was transferred to an oven pre-heated to 130°C for 40 minutes for a second annealing step. After oven annealing, any remaining bubbles were meticulously removed. Finally, the thoroughly cleaned PET film (prepared as described above) was adhered to this activated double-sided tape after its protective top layer was removed.
For the active layer preparation, P3HT solutions were prepared at a concentration of

33 mg/mL in anhydrous chlorobenzene. To ensure complete dissolution and homogeneity, the P3HT solution was stirred overnight at 50°C prior to spin-coating. To promote uniform film acquisition, the glass-backed PET substrates were pre-heated on a hot plate at 75°C for 10 minutes immediately before being transferred to the spin coater. P3HT thin films were then deposited via spin-coating using 400 μL of the prepared solution onto each 5 cm × 5 cm substrate. The spin-coating parameters were set to 1500 rpm with an acceleration of 3000 rpm for a duration of 30 seconds. Following spin-coating, post-deposition annealing was applied to distinct test groups under three different conditions: no annealing, annealing at 50°C, and at 75°C for 5 minutes each.

In addition to the single-layer samples, bilayer structures incorporating a thin PEDOT:PSS hole-transport layer were fabricated. PEDOT:PSS primarily served as an adhesion-promoting interlayer to enhance mechanical coupling between PET and P3HT. The dispersion (98% PEDOT, 2% surfactant additive) was spin-coated at 5000 rpm for 60 seconds using 1000 µL per sample, followed by annealing at 130 °C for 30 minutes to remove residual solvent. The P3HT layer was then deposited under the same spin-coating conditions, yielding PET/PEDOT:PSS/P3HT stacks with improved mechanical stability.

4.4.1 Sample Dimensions for Testing and Strain Application Protocol

After the respective annealing treatments (for P3HT and PEDOT:PSS/P3HT films) or initial cleaning (for bare PET films), test samples with standardized dimensions of 15 mm × 33 mm were precisely cut from the larger 5 cm × 5 cm substrates. These dimensions were optimized for compatibility with the custom-built mechanical stretcher device and the spectroscopic measurement setups.

The uniaxial tensile strain was applied incrementally using the custom-built mechanical strain device. For all experimental tests, a consistent initial gauge length (L_0) of 25 mm was established. The remaining 4 mm on each side of the 33 mm length were used for clamping, ensuring a secure and stable hold of the polymer film. The precise linear displacement (ΔL) for each strain level was achieved by controlling the number of microsteps of the linear actuator, with each microstep corresponding to 6.25 μm, as established through meticulous calibration. Strain levels for bare PET films ranged from 1% to 30% elongation. For P3HT-coated samples, the applied strain was limited to a range of 1% to 10%. This limitation was implemented because preliminary results from bare PET indicated significant structural variations and enhanced absorption beyond 10% strain, which could potentially overshadow

the subtle P3HT responses and lead to material failure in the composite system.
A critical distinction in the strain application and measurement protocol existed between the spectroscopic techniques:

- For **ex-situ UV–Vis absorption measurements**, samples were subjected to a specified strain level on the custom stretcher and held for a relaxation period of 30 minutes. After this period, the sample was released from strain and immediately transferred to the spectrophotometer for absorbance acquisition. A new, unstretched film was used for each strain value in UV–Vis measurements to ensure consistent and independent observations of persistent optical modifications.

- For **in-situ Raman spectroscopy**, the samples remained mounted and under continuous mechanical strain on the custom stretcher throughout the measurement process. Raman spectra were acquired at regular 5-minute intervals during the 30-minute strain application, capturing transient molecular adjustments and dynamic responses to the applied deformation.

4.5 Spectroscopic Characterization Protocols

4.5.1 UV–Vis Absorption Spectroscopy Setup and Protocol

UV–Vis absorption measurements were conducted using a PerkinElmer Lambda 12 spectrophotometer. The instrument was utilized to assess changes in the absorbance and transmittance of the films across the 200–1000 nm wavelength range. Samples were positioned directly in the optical beam path, and all measurements were performed using unpolarized light, capturing the intrinsic, orientation-averaged absorption behaviour. Baseline correction was applied using air as a reference.

- For **bare PET films**, to obtain a representative average optical response, four spectra were initially recorded from each unstretched sample, involving rotating the film by 180° to capture two measurement areas (11 mm in length and 0.5 mm in width) on both sides of the sample center. An identical rotational approach was employed after strain application and release, with spectra subsequently averaged.

- For **P3HT-coated samples (on bare PET and PET/PEDOT:PSS)**, precise sample positioning within the spectrophotometer's beam path was ensured by utilizing two stages with different heights designed to bring the sample

into the optimal optical path, and the final reported spectral response was an average of three collected spectra.

4.5.2 Raman Spectroscopy Setup and Protocol

In-situ Raman spectra were acquired using a sophisticated setup featuring the 514 nm line of an argon-ion laser (Innova 308 series, Coherent, U.S.A.) as the primary excitation source. The laser beam was focused onto the sample surface using an ultra-long working distance objective (50× Ultra-Long Working Distance (objective) (ULWD), N.A. 0.50, Olympus, Japan), which simultaneously facilitated efficient collection of scattered light. Laser power at the sample surface was approximately 5 mW.

The scattered light was directed into a Triax 550 single monochromator (Jobin Yvon, France), equipped with a 1200 grooves/mm diffraction grating. The entrance slit width was set to 100 μm, yielding a spectral resolution of 3 cm^{-1} at 514 nm. Broadband detection was accomplished using liquid nitrogen-cooled Charge-Coupled Device (CCD) detectors (CCD 3500, Jobin Yvon, France). Raman spectra were recorded in a back-scattering geometry. Wavenumber calibration was performed using the aromatic toluene breathing mode at 1003.7 cm^{-1}. The excitation laser's polarization was fixed parallel to the strain axis.

The in-situ protocol for Raman spectroscopy involved taking measurements directly on the strained films at regular intervals of 5 minutes during the 30-minute strain application, capturing transient molecular adjustments and dynamic responses. For P3HT-coated samples, similar spectroscopic settings and the in-situ measurement protocol were strictly adhered to, ensuring the comparability of molecular insights between the bare PET and the composite PET/P3HT and PET/PEDOT:PSS/P3HT systems. Raman spectra data were analysed to extract line positions, FWHM, and intensity variations for key vibration modes.

Chapter 5

Electrical Modeling of Strain-Induced Morphological Alterations in Organic Solar Cells

5.1 Introduction to Simulation Approach and Rationale

As highlighted in the Introduction (1), a significant challenge in advancing strain resilient OSC lies in the limited fundamental understanding of how mechanical strain directly modifies the material-level optical and electrical properties within individual functional layers. This knowledge gap, in turn, critically hinders the development of accurate predictive models and the rational design of next generation flexible devices. This chapter directly addresses this challenge by detailing the initial computational efforts, employing FEM, to rigorously model the electrical effects of applied mechanical strain specifically on the active layer of organic solar cells. This foundational modeling work, described in Chapter 4, was instrumental in identifying specific material-level parameter gaps. These gaps directly informed the design of the experimental investigations presented in later chapters. This chapter is published in IEEE-NANO 2024 conference article [141].

M. Ghorab, V. Wagner, and M. Joodaki. "Electrical Modeling of Active Layer Morphology Alterations in Response to Applied Mechanical Strain in Organic Solar Cells". Proceedings of the 2024 IEEE 24th International Conference on Nanotechnology (NANO), 2024, pp. 97–102.

5.1.1 Device Architecture Description

In order to rigorously model the coupled optical and electrical behaviour of OSCs subjected to mechanical strain, it is essential to begin with a well-defined and experimentally grounded device architecture. This study adopts a prototypical BHJ configuration incorporating a P3HT:PCBM active layer, selected for its historical significance and continued relevance as a benchmark system in organic photovoltaics. The multilayer structure, optimized based on established design principles and prior fabrication data, forms the basis for FEM simulations conducted in COMSOL Multiphysics [153]. This framework enables high resolution spatial modeling of strain-induced variations in optoelectronic behaviour across the active layer.
Figure 5.1 shows the modeled OSC. It consists of a six-layer stack arranged on a semi-infinite glass substrate, progressing upward through functional layers selected for their complementary optoelectronic roles. At the base, a 200 nm layer of ITO serves as the transparent anode. It offers both high optical transmittance and efficient hole extraction. This is followed by a 30 nm Zinc Oxide (ZnO) layer, functioning as the Electron Transport Layer (ETL). This material was chosen for its favorable energy alignment with fullerene acceptors and its low temperature processability. The core of the device comprises a 200 nm active layer formed by a P3HT:PCBM blend in a bulk heterojunction morphology, enabling efficient exciton dissociation and charge separation. Above this, a 40 nm layer of PEDOT:PSS is employed as a Hole Transport Layer (HTL), enhancing interfacial contact and reducing energetic barriers at the anode interface. The stack is completed by a 100 nm silver (Ag) electrode, which acts both as the cathode and an optical mirror, reflecting unabsorbed photons back into the active layer to enhance light-harvesting efficiency.

The material choices for this device architecture reflect a deliberate emphasis on established performance, reproducibility, and physical interpretability. The P3HT:PCBM blend remains one of the most thoroughly characterized donor–acceptor systems in organic photovoltaics. It offers well resolved optical constants, predictable nanoscale morphology, and consistent charge transport behaviour across a wide range of processing conditions. Its continued use as a model system facilitates meaningful comparison with both prior studies and emerging materials. The ZnO electron transport layer is widely adopted due to its favorable conduction band alignment with PCBM and its high electron mobility. Its inherent transparency in the visible spectrum further makes it well suited for both inverted and conventional OSC architectures. PEDOT:PSS, despite its susceptibility to humidity and acidity, remains a

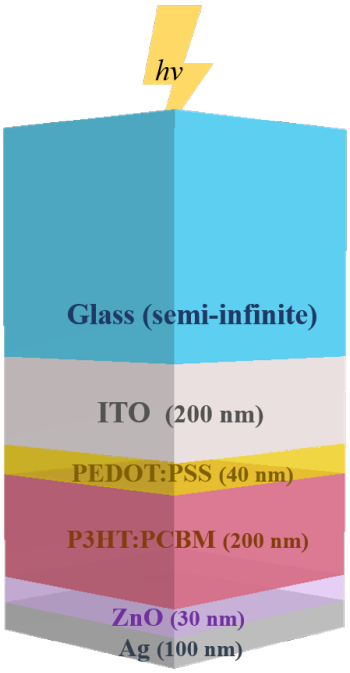

Fig. 5.1: OSC structure represents the different layer thickness and materials.

benchmark hole transport material. This is due to its solution processability, mechanical flexibility, and work function compatibility with ITO. The inclusion of Ag as the reflective cathode is consistent with conventional design strategies aimed at enhancing optical path length within the active layer. Collectively, these materials form a canonical structure that serves as a robust platform for exploring strain-dependent optoelectronic phenomena through simulation [132].

The multilayer architecture described above is particularly well suited for FEM. This is due to its geometric uniformity, well-characterized interfaces, and the availability of established material parameters from prior experimental studies. In the present study, mechanical strain is not simulated explicitly as a mechanical field. Instead, its experimentally inferred effects—such as reductions in bimolecular recombination, modeled via a decreased Langevin pre-factor (ζ), and modest increases in the effective bandgap (E_g)—are implemented as parameter modifications within the electrical model. This strategy enables a controlled investigation of how tensile strain–induced morphological changes in the active layer affect macroscopic device performance. It does so without introducing confounding effects from layer delamination or structural failure. As such, the model serves as an effective approximation of early stage strain-induced enhancements, complementing subsequent experimental investigations.

5.2 2-Dimensional Optical Modeling Methodology

5.2.1 Theoretical Framework: Maxwell's Equations in Layered Media

The optical modeling framework employed in this study is grounded in the solution of frequency-domain Maxwell's equations, which provide a comprehensive description of electromagnetic wave propagation in stratified media. This formalism is particularly well suited for analyzing thin-film OSCs, where optical interference, resonant absorption, and spatial field variation critically influence photogeneration efficiency.

Within the Wave Optics Module of COMSOL Multiphysics, the multilayer OSC stack is treated as a linear, isotropic, and non-magnetic medium. Under these assumptions, the electric and magnetic field distributions are derived from the source free curl equations in the frequency domain:

$$\nabla \times \vec{H}_{\text{opt}} = j2\pi\nu\epsilon_r(\nu)\epsilon_0\vec{E}_{\text{opt}} \tag{1}$$

$$\nabla \times \vec{E}_{\text{opt}} = -j2\pi\nu\mu_0\vec{H}_{\text{opt}} \tag{2}$$

Here, $\vec{E}_{\text{opt}}$ and $\vec{H}_{\text{opt}}$ denote the time-harmonic electric and magnetic field vectors at optical frequency ν. The complex, frequency-dependent relative permittivity $\epsilon_r(\nu) = \epsilon_1 - j\epsilon_2$ captures both refractive (real part) and absorptive (imaginary part) characteristics of each layer, based on interpolated experimental data [154]. By solving these equations across the layered domain, the model yields a spatially resolved optical field intensity profile that inherently accounts for interference effects, field localization, and resonant absorption phenomena that arise in nanostructured multilayer devices. These effects are particularly significant in OSCs due to their sub-micron active layers and optically thin charge transport layers. This rigorous full-wave approach enables accurate computation of local power absorption within the photoactive blend. This quantity is an essential precursor for quantifying exciton generation rates and evaluating internal quantum efficiency. Unlike simplified ray-optics approximations, this method provides precise insight into how device architecture and material dispersion govern light-harvesting behaviour in realistic organic photovoltaic stacks.

5.2.2 Optical Constants and Material Parameters

The fidelity of optical simulations in OSCs hinges on the accurate representation of frequency-dependent dielectric constant for each constituent layer. In this model, each material is characterized by a complex relative permittivity $\epsilon_r(\nu) = \epsilon_1 - j\epsilon_2$, where ϵ_1 represents the real part (refractive index contribution) and ϵ_2 accounts for the imaginary part (absorption losses). These values were obtained from literature reported experimental ellipsometry data and incorporated into the simulation as interpolated datasets [155]. The dielectric properties of the active layer—comprising a BHJ blend of P3HT and PCBM—were approximated using a linear weighted average of the individual dielectric constant of pristine P3HT and PCBM. This approach is widely adopted in full-field optical modeling. It assumes that the nanoscale phase separation within the blend can be effectively treated as a homogeneous medium for optical field propagation. While this approximation neglects interfacial effects and local field variations, it offers substantial computational efficiency and adequately captures the macroscopic absorption behaviour of the active layer [156]. The effective dielectric constant of the blend was used as an input to the model to compute the spatial absorption profile and to estimate the corresponding polaron generation rate. For the remaining functional layers, literature values were similarly used for ITO, PEDOT:PSS, ZnO, and Ag, with particular care taken to select wavelength resolved datasets that spanned the entire solar spectrum. This comprehensive material parameterization ensures consistency in the optical response across all layers. It also enables a physically accurate simulation of light–matter interactions within the OSC stack [157].

5.2.3 Computation of Polaron Generation Rate

In organic photovoltaic systems, optical absorption in the active layer produces tightly bound excitons that must dissociate at D–A interfaces to form free carriers [158, 159]. To model this process numerically, the polaron generation rate is computed based on the spatial and spectral distribution of absorbed optical power. The spectrally resolved absorbed power density, $Q_{\text{abs}}(x, y, \nu)$, is given by:

$$Q_{\text{abs}}(x, y, \nu) = \frac{1}{2}\,\epsilon_0\,\nu\,\epsilon_2(x, y, \nu)\,|E_{\text{opt}}(x, y, \nu)|^2 \tag{3}$$

Here, $\epsilon_2(x, y, \nu)$ is the imaginary part of the complex permittivity, ν is the optical frequency, and $E_{\text{opt}}(x, y, \nu)$ is the local optical electric field amplitude. The local polaron generation rate at a given frequency is then calculated as:

$$G(x, y, \nu) = \frac{Q_{\text{abs}}(x, y, \nu)}{h\nu} \tag{4}$$

To compute the total polaron generation rate under Standard Solar Spectrum (Air Mass 1.5) (AM1.5) solar illumination, the frequency-resolved rate is integrated over the incident solar spectrum:

$$G_{\text{tot}}(x, y) = \int_{\nu} \frac{Q_{\text{abs}}(x, y, \nu)}{h\nu} \cdot S(\nu) \cdot T_{\text{N}}(\nu)\, d\nu \tag{5}$$

In this expression, $S(\nu)$ represents the spectral photon flux density of the AM1.5 Global spectrum, expressed in units of photons.m^{-2}.s^{-1}.Hz^{-1}. The factor $T_{\text{N}}(\nu)$ accounts for the normalized spectral transmission into the device and is defined as:

$$T_{\text{N}}(\nu) = 1 - R_{\text{N}}(\nu) \tag{5.1}$$

where $R_{\text{N}}(\nu)$ is the spectral reflectance of the glass/air interface, computed using Fresnel equations [155, 160]. For unpolarized light at normal incidence, and assuming a typical glass refractive index of $n_{\text{glass}} \approx 1.5$, the transmission coefficient simplifies to:

$$T_{\text{N}}(\nu) \approx 0.961 \tag{5.2}$$

5.3 Charge Dissociation Model

The process of exciton dissociation in OSCs fundamentally governs the efficiency of free carrier generation and is a primary bottleneck in optimizing charge collection. Historically, the theoretical foundation for describing charge separation was laid by Onsager in 1938. He treated ion pair dissociation under an applied electric field in a polar solvent as a thermally activated escape process governed by Coulombic attraction. His model yielded an expression for the dissociation probability $P_{\text{Ons}}(E, r)$ based on the pair separation distance r, the field strength E, and the dielectric permittivity ε of the medium. The Onsager approach, however, assumed isotropic media and infinite charge mobility, which limits its applicability to modern low-mobility, disordered semiconductors [161, 162].

In 1984, Braun refined this formalism to account for the finite lifetime of bound electron–hole pairs (geminate excitons) in molecular semiconductors. The resulting

Onsager–Braun model introduced a rate equation approach, incorporating both the field-assisted escape and geminate recombination rates:

$$P_{\text{Braun}} = \frac{k_d(E)}{k_d(E) + k_f}$$

where $k_d(E)$ is the field-dependent dissociation rate and k_f is the exciton decay rate. While this modification allowed some alignment with the experimental behaviour of early OSCs, it still assumed spherical symmetry and neglected the influence of molecular architecture or electronic structure [163].

Despite the historical significance of these models, they fail to fully capture the physics of high-efficiency BHJ solar cells based on blends such as P3HT:PCBM. These modern OSCs exhibit near-unity dissociation yields under modest internal fields (on the order of 10^5–10^6 V/m) and low exciton binding energies (<0.2 eV), indicating that alternative microscopic mechanisms dominate. As discussed by Liraz and Tessler, the applicability of Onsager-based models is largely limited to inefficient or thick-film systems. In contemporary OSCs, charge separation is often field-independent, entropy-assisted, and occurs over length scales comparable to the D–A interface (∼1–2 nm) [164].

To account for this, we adopt the Arkhipov–Baranovskii model, which better reflects the microscopic dynamics at the polymer–fullerene interface [165, 166]. This model postulates that after photoexcitation, the exciton rapidly localizes at the donor–acceptor interface to form a CT state. Dissociation proceeds via thermally assisted hopping of one carrier, typically the electron, into the acceptor domain.

In the context of our P3HT:PCBM active layer, the average internal electric field of $\sim 10^6$ V/m under illumination was calculated in COMSOL Multiphysics. This value is consistent with reported operating conditions of thin-film devices. According to Arkhipov and Baranovskii's model (as plotted in [166]), and assuming comparable effective masses for electrons and holes (i.e., $m_e^* = m_h^*$), the charge separation efficiency exceeds 80% at this field. We therefore adopt a constant dissociation probability $P = 0.8$ throughout our device simulation as a first-order approximation, consistent with experimental electroluminescence quenching and photocurrent saturation studies on similar blends.

Furthermore, the Liraz–Tessler review provides strong theoretical justification for using a constant high-yield model [164]. They highlight that in well optimized OSCs, dissociation is entropically favored and promoted by:

- Molecular orbital delocalization
- Short D–A domain spacing (<2 nm)

- High local permittivity due to PCBM clustering
- Interface-induced hybridization of electronic states

As such, attempts to fit device scale data using field dependent Onsager models can systematically underestimate the yield and fail to capture the observed weak dependence on bias.
In light of this, the Arkhipov–Baranovskii formalism serves as a more physically accurate and computationally tractable approach. It bridges the conceptual gap between classical field-driven escape and quantum-mechanical CT-state splitting. This dissociation model is therefore integrated directly into the drift–diffusion simulations.

5.4 2-Dimensional Charge Transport Model (Drift-Diffusion)

To simulate charge transport behaviour within the OSC under optical excitation, a drift-diffusion model was employed. This continuum approach was originally developed for crystalline semiconductors. It has since been widely adapted for organic systems due to its computational efficiency. When appropriately parameterized, it provides reasonable accuracy in predicting device scale electrostatic and transport behaviour.
Given the need to resolve carrier dynamics at nanometer-to-micrometer scales, while also preserving computational tractability, the model domain was reduced to encompass only the semiconductor functional core: PEDOT:PSS (hole transport layer), P3HT:PCBM (active layer), and ZnO (electron transport layer). The electrodes (ITO and Ag) were excluded from the meshed domain due to their strong work-function alignment with the adjacent layers. This allowed them to be idealized as Ohmic contacts, a common and well validated assumption in OSC modeling.
Charge carrier motion was described using the coupled drift-diffusion and Poisson equations, capturing both field driven drift and thermally induced diffusion processes. The steady state expressions for carrier current densities are:

$$J_n = q\mu_n nE + qD_n \nabla n \tag{5.3}$$

$$J_p = q\mu_p pE - qD_p \nabla p \tag{5.4}$$

where $\mu_{n,p}$ are field-independent mobilities (assumed constant), and $D_{n,p}$ are linked via the Einstein relation $D = \mu V_T$, with V_T as the thermal voltage (kT/q). Electro-

static self-consistency is maintained through Poisson's equation:

$$\nabla^2 V = \frac{q}{\epsilon_0 \epsilon_{r0}}(n - p). \tag{5.5}$$

The dielectric permittivity ε_r was spatially defined per material layer. This coupling ensures dynamic field redistribution in response to photogeneration and recombination.

Steady-state continuity is enforced via:

$$\frac{1}{q}\nabla J_{\mathrm{n}} = PG_{\mathrm{tot}} - (1-P)R, \quad \frac{1}{q}\nabla J_{\mathrm{p}} = -PG_{\mathrm{tot}} - (1-P)R. \tag{5.6}$$

where:

- G_{tot}: total polaron generation rate (via optical modeling),
- P: exciton dissociation probability (modeled via Arkhipov-Baranovskii formalism),
- R: net recombination rate.

Boundary conditions at the PEDOT:PSS and ZnO interfaces implement Dirichlet constraints for potential and carrier densities, consistent with the Ohmic approximation. These assumptions are justified by experimental data showing negligible injection barriers and fast carrier extraction at these interfaces in optimized P3HT:PCBM systems.

5.5 Charge Recombination Mechanisms

Charge recombination fundamentally limits the PCE of OSCs by acting as a loss pathway for photogenerated charge carriers. In drift–diffusion models, accurate representation of recombination processes is critical. This is particularly true when strain-induced morphological or electronic changes are modeled through parametric modulation of transport properties. The present model includes two dominant mechanisms: Trap-Assisted Recombination (TAR) and bimolecular (band-to-band) recombination. These mechanisms are treated separately, enabling nuanced control over the material and interfacial parameters most sensitive to device processing and morphological alterations.

5.5.1 TAR: A Disorder-Driven Mechanism

TAR is modeled here as a first-order Shockley–Read–Hall (recombination) (SRH) process mediated by localized states within the energy gap. In OSCs, such trap states often emerge from structural disorder, incomplete D–A mixing, residual solvent effects, or chemical impurities, which are intrinsic to solution-processed active layers. These states typically lie 0.35–0.6 eV below the transport level and act as recombination centers that facilitate carrier decay via thermally activated capture and re-emission processes. Although the model does not explicitly resolve the Density of States (DOS) distribution, it incorporates an effective trap density in the range of $10^{16} - 10^{17}\,\mathrm{cm}^{-3}$. This range is consistent with spectroscopic measurements and transport studies of annealed P3HT:PCBM films [167–169]. This approximation allows the simulation to capture the macroscopic consequences of material disorder and suppressed fill factors while remaining computationally tractable.

5.5.2 Bimolecular Recombination and the Modified Langevin Framework

Bimolecular or band-to-band recombination arises from the Coulombic interaction between free electrons and holes and in low mobility disorder materials is described by Langevin theory:

$$R = \zeta \cdot \gamma(np - n_i^2) \tag{5.7}$$

where

- $\gamma = \frac{q(\mu_n+\mu_p)}{\varepsilon_0\varepsilon_r}$ is the Langevin recombination prefactor,
- μ_n and μ_p are the electron and hole mobilities,
- ε_0 and ε_r denote vacuum and relative permittivity,
- and ζ is the reduction factor, introduced to account for the known overestimation of recombination rates by classical Langevin theory in polymer:fullerene blends.

Numerous studies have shown that the spatial heterogeneity of BHJ morphologies originating from phase segregation and percolation limited transport significantly suppresses recombination relative to the Langevin prediction. This is because electrons and holes are typically confined within discrete phases (e.g., electrons in PCBM-rich domains, holes in P3HT), and recombination only occurs at the interfacial boundary regions. Thus, the actual rate is governed not only by carrier

densities and mobilities but also by interfacial surface area, domain purity, and carrier diffusion lengths [170]. In this work, ζ is treated as a morphology-sensitive tuning parameter, set at 0.02 for baseline simulation [171]. Crucially, this parameter is later modulated in the strain dependent simulations to reflect changes in D–A interpenetration and polymer chain alignment.

5.6 Simulation Parameters and Model Calibration

To ensure that the electrical simulation framework accurately captures the steady-state behaviour of the OSC, this section details the physical parameters adopted for the P3HT:PCBM active layer. Each parameter was chosen based on the experimentally grounded values. The material parameters used in the semiconductor transport simulation are presented in Table 5.1 (Simulation Parameters for P3HT:PCBM Active Layer).

The electron and hole mobilities were both set to $1.0 \times 10^{-4}\,\mathrm{cm}^2/\mathrm{V{\cdot}s}$, which reflect typical values found in regioregular P3HT and fullerene rich PCBM blends. This symmetric assumption simplifies numerical convergence while retaining physical relevance. The relative permittivity was assigned a value of 3.4, representing an effective medium approximation for the bulk P3HT:PCBM blend. Local polarization effects within the heterogeneous D–A domains were not explicitly resolved. Moreover, the effective ban dgap of the P3HT:PCBM blend was calculated as the energy difference between the HOMO of P3HT and the LUMO of PCBM, reflecting the CT mechanism that governs exciton dissociation and charge generation in bulk heterojunction systems. Carrier effective DOS for the conduction and valence bands were each set to $1.0 \times 10^{18}\,\mathrm{cm}^{-3}$, consistent with values used in drift-diffusion modeling of disordered organic materials [132].

The charge recombination dynamics were modeled using the conventional Langevin mechanism. A reduced recombination prefactor introduced by the empirical factor ζ, set at 0.02, which accounts for the reported deviations between theoretical Langevin rates and experimentally observed recombination behaviour in BHJ architectures [170]. Furthermore, TAR was incorporated through an effective trap density of $5.0 \times 10^{16}\,\mathrm{cm}^{-3}$, representing localized defect states within the tail of the DOS distribution [167, 168]. The exciton dissociation probability was fixed at 0.8, in alignment with predictions from the Arkhipov–Baranovskii model [165, 166]. All simulations were performed at room temperature (300 K) under AM1.5 solar illumination conditions.

The simulation of electrical behaviour was implemented using the Semiconductor

Table 5.1: Active layer material (P3HT:PCBM) parameters employed for the FEM simulation

P3HT:PCBM simulation parameters	**Symbols**	**Values**	**References**
Bandgap	E_g	1.5 [eV]	[132]
Electron affinity	E_a	3.7 [eV]	[132]
Effective DOS conduction (valence) band	$N_{C(V)}$	10^{18} [cm^{-3}]	[132]
Electron (hole) mobility	$\mu_{n(p)}$	7.6×10^{-4} [$cm^2/(V\,s)$]	[132]
Effective relative permittivity	ϵ_r	3.4	[132]
Langevin recombination factor	γ	0.805×10^{-15}	[132]
Reduced Langevin recombination pre-factor	ζ	2×10^{-2}	[171]
Trap number density	N_t	5×10^{16} [cm^{-3}]	[167, 169]
Gaussian trap distribution center point from conduction band	$E_{t,0}$	0.35 [eV]	[167, 169]
Gaussian trap distribution width	σ	0.1 [eV]	[167, 169]

Module of COMSOL Multiphysics, employing a time-independent (steady-state) solver to compute the coupled nonlinear partial differential equations governing carrier transport. These include the Poisson equation for electrostatic potential distribution and the improved continuity equations for electron and hole densities, as well as exciton dissociation probability. To ensure convergence and numerical stability, a fully coupled Newton-Raphson iterative method was employed, with adaptive damping and a maximum iteration threshold of 50 steps per load increment. Mesh refinement was performed using a non-uniform, physics-controlled distribution. Finer resolution was applied at the PEDOT:PSS/P3HT:PCBM and P3HT:PCBM/ZnO interfaces, where sharp potential gradients and carrier concentration transitions occur. Dirichlet boundary conditions were applied at the electrode interfaces to model Ohmic contact behaviour, with the anode grounded and a variable potential applied at the cathode to sweep the J–V characteristics. The initial electrostatic potential was set uniformly to zero, and the carrier concentrations were initialized to equilibrium values derived from the intrinsic, doping-free assumption. No explicit recombination velocity terms were used at the interfaces due to the strong injection assumption and absence of significant contact barriers in this simplified model.
Figure 5.2 presents the J–V characteristics curve of the simulated structure. As shown the simulation yields a J_{sc} of 13.169 mA/cm², V_{oc} of 0.6008 V, FF of 53.39%, and PCE of 4.2242%. These values are in strong agreement with experimentally

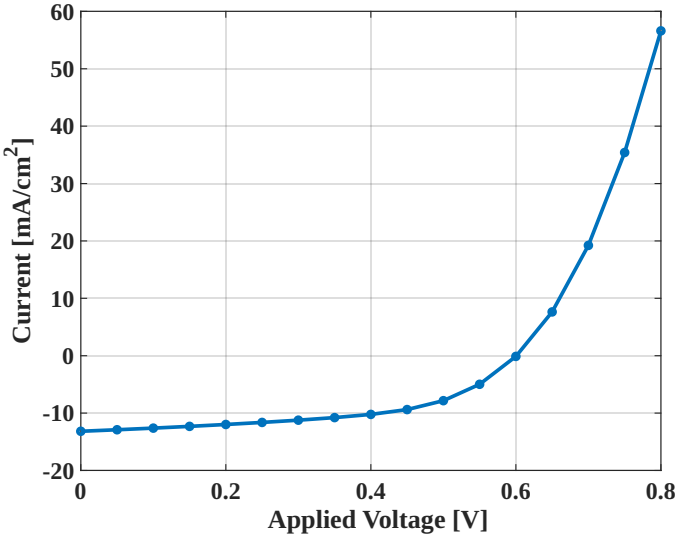

Fig. 5.2: Simulated J–V curve of the baseline P3HT:PCBM device under AM1.5 illumination.

reported figures for P3HT:PCBM devices fabricated under standard atmospheric conditions. Hence, the simulation framework was considered as the platform for exploring how perturbations to parameters such as recombination prefactors would modulate the electrical response of the device.

5.7 Modeling the Effect of Strain on Active Layer Performance

5.7.1 Strain Regimes and Morphological Interpretation

Mechanical deformation of OSCs initiates a complex series of structural transformations within the active layer that are highly dependent on morphology and manifest non-linearly in device performance. Spectroscopic and non-spectroscopic observations reveal two distinct response regimes to uniaxial tensile strain:

- **Pre-catastrophic Regime:** In this domain, low to moderate uniaxial strain introduces anisotropic deformation in the polymer matrix without breaching the mechanical limits of the multilayer stack. Structurally, the system undergoes morphological reordering, characterized by enhanced crystallinity, increased polymer chain alignment, and potential modulation of interfacial orientation. The characteristic of this regime is that these changes are beneficial for device performance and can be observed in improvements of J_{sc}, V_{oc}, FF, and PCE [95].

- **Catastrophic Regime:** Beyond a critical strain threshold, which can vary depending on the layer stack and constituent materials, the active layer enters a mechanically unstable regime. Here, the stored elastic energy exceeds the cohesive forces that govern the molecular packing and interfacial adhesion. The consequence is irreversible disruption of the active layer morphology, including interfacial delamination, polymer chain scission, phase decohesion, and in some cases, crack formation in encapsulation layers. Optical anisotropy and mechanical spectroscopy confirm the onset of structural fatigue and loss of percolated charge transport pathways. Electrical performance degrades rapidly, typically exhibiting suppressed V_{oc} and FF, increased leakage current, and hysteresis in J–V curves [95].

5.7.2 Mechanisms of Enhancement in the Pre-Catastrophic Regime

The following interconnected phenomena have been discussed as to rationalize the enhancements observed within the pre-catastrophic regime,

- **Polymer Chain Alignment:** Mechanical strain aligns polymer chains along the axis of deformation, a phenomenon governed by enthalpic penalization of chain bending and the anisotropic response of semicrystalline domains. For π-conjugated polymers like P3HT, this realignment increases the effective conjugation length, reduces torsional disorder between thiophene rings, and enhances intra-chain charge delocalization [172, 173]. At the morphological level, strain-induced alignment also reduces inter-domain misorientation, allowing for the formation of percolated pathways along the strain axis. This enhances directional charge carrier mobility, which is particularly beneficial for vertically structured OSCs. Grazing-Incidence Wide-Angle X-ray Scattering (GIWAXS) studies consistently demonstrate narrowing of the π–π stacking peak under strain, indicating increased coherence length and crystallographic ordering [128, 172, 174].

- **Orientation Transition: Edge-on to Face-on:** The orientation of polymer backbones relative to the substrate plane plays a pivotal role in vertical charge transport. In an "edge-on" orientation, the conjugated backbone lies parallel to the substrate with π-stacks perpendicular, favoring in-plane transport but hindering vertical extraction. In contrast, the "face-on" configuration aligns the π-stacks along the substrate normal. This directly enhances out-of-plane carrier mobility and the overlap between light absorption and the

electric field. Strain has been shown to induce partial reorientation of polymer crystallites from edge-on to face-on, particularly near the polymer/substrate interface where shear stress concentrates. This transition arises from the minimization of strain energy under anisotropic modulus conditions between the amorphous and crystalline domains [175].

- **Enhanced Aggregation and Crystallinity:** Mechanical deformation also serves as a kinetic facilitator for molecular rearrangement and crystallite growth. Under strain, polymer chains in the amorphous matrix experience anisotropic tension, which can lower the free energy barrier for nucleation and promote alignment into ordered aggregates. Moreover, increased aggregation improves inter-chain hopping integrals by bringing π-systems into closer proximity. The resulting effect is an increase in both the DOS at the band edges and the electronic coupling strength, which jointly enhance charge mobility and reduce dispersive transport [128, 176].

Collectively, these phenomena provide a compelling physical basis for the experimentally observed strain-induced enhancement in OSC performance within the pre-catastrophic regime. In the simulation framework developed herein, these effects are not directly modeled as structural transformations, but rather embedded into the model via tunable electronic parameters. The next section details how variations in recombination prefactor and bandgap were introduced to mimic these morphological effects and quantitatively capture the strain–performance relationship.

5.8 Parameterization of Morphology via Electrical Surrogates

Tensile strain induces morphological changes across multiple length scales that cannot be explicitly resolved within a computationally manageable framework. Instead of directly simulating the strain-dependent microstructure, we captured its dominant functional consequences using two effective electronic surrogate parameters.
This strategy does not assume a one-to-one correspondence between morphology and model variables. Rather, it evaluates whether experimentally plausible strain-induced modifications in (i) recombination kinetics and (ii) D–A energetic alignment are sufficient to reproduce the observed device performance trends.
The two chosen surrogates are therefore:

- The Langevin recombination prefactor, ζ, representing morphology-dependent suppression of bimolecular recombination.
- The effective bandgap, E_g, representing strain-induced modulation of electronic energy alignment.

Moreover, this parameterization does not imply that morphology affects only recombination and energetic alignment. Rather, these two quantities were selected as minimal, physically interpretable levers within the current model that allow strain-induced structural effects to be explored without introducing additional unverified transport assumptions.

5.8.1 Modulating the Langevin Prefactor ζ: Proxy for Recombination Dynamics

As mentioned earlier, ζ in the modified Langevin framework captures morphology-induced suppression of bimolecular recombination in bulk heterojunction systems. Awartani *et al.* reported that tensile strain enhances P3HT aggregation and promotes increased PCBM interpenetration within amorphous regions [177, 178]. Such reorganization improves percolation pathways and can reduce the effective overlap of electron and hole populations within mixed regions [130]. Within a reduced Langevin recombination framework, such structural evolution would be expected to manifest as a decrease in the effective recombination prefactor (ζ).
In the baseline configuration, ζ was set to 0.02, consistent with experimentally reported reduced-Langevin values for P3HT:PCBM blends and with values previously measured in the research group [171]. To simulate strain-induced suppression of bimolecular recombination in the pre-catastrophic regime, ζ was reduced to 2×10^{-3}. Importantly, this reduction remains fully within the experimentally reported reduced-Langevin range for P3HT:PCBM systems. The variation therefore represents a controlled exploration of physically plausible parameter space rather than a direct extraction from strain-resolved recombination measurements [170].

5.8.2 Bandgap Tuning as a Marker for Strain-Induced Modulation of D–A Energy Alignment

Mechanical strain has been shown to modify the electronic structure of conjugated polymer systems at both molecular and interfacial scales. Experimental investigations by Kim *et al.* demonstrate strain-dependent modulation of the elec-

tronic response in P3HT [30]. Complementary DFT calculations by Menichetti *et al.* show that uniaxial strain modifies both the intrinsic donor bandgap and the HOMO(P3HT)–LUMO(PCBM) energy offset in PCBM:P3HT systems. [29].
Menichetti *et al.* report variations in the effective HOMO(P3HT)–LUMO(PCBM) energy difference on the order of ~ 0.08 eV per $\sim 1\%$ uniaxial strain. This indicates that strain-induced energetic shifts on the scale of several tens of meV can arise from molecular deformation and interfacial reconfiguration.
To represent this effect at the device scale, the effective bandgap E_g in the model was increased from 1.50 eV to 1.59 eV ($\Delta E_g = 0.09$ eV). This perturbation is comparable in magnitude to the strain-induced energetic variations predicted by DFT calculations.
It is important to emphasize that the energetic variations reported by Menichetti *et al.* were obtained from molecular-scale calculations of specific D–A configurations. In contrast, the presented drift–diffusion model treats the active layer as an effective bulk heterojunction medium without explicit molecular resolution. The applied ΔE_g should therefore be interpreted as a continuum-level representation of strain-sensitive energetic modulation, rather than a direct quantitative mapping from a single molecular geometry.
When implemented in the device model, the increase in the effective E_g leads primarily to an elevation of V_{oc}. This is shifting the simulated performance closer to the strain-enhanced experimental values observed in the previous work. The energetic perturbation was applied uniformly across the active layer. In this study, the spatial strain gradients and local interfacial dipoles are not explicitly resolved.

5.9 Simulation Results: Impact of Parameter Variation

We examined whether the surrogate parameters introduced in Section 5.8 are sufficient to reproduce the experimentally observed strain response. This was done through controlled parameter variations within the calibrated drift–diffusion–Poisson framework.
Three configurations were examined:

1. Baseline device: $E_g = 1.50$ eV, $\zeta = 2 \times 10^{-2}$
2. Energetic modulation only: $E_g = 1.59$ eV, $\zeta = 2 \times 10^{-2}$
3. Combined energetic and recombination modulation: $E_g = 1.59$ eV, $\zeta = 2 \times$

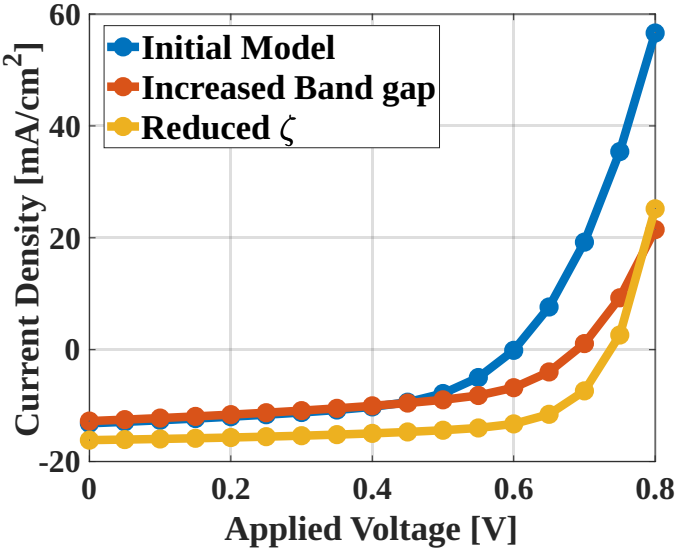

Fig. 5.3: J − V characteristics for (i) baseline conditions (labeled as: Initial Model) ($E_g = 1.50$ eV, $\zeta = 2 \times 10^{-2}$), (ii) energetic modulation only (labeled as: Increased Band gap) ($E_g = 1.59$ eV, $\zeta = 2 \times 10^{-2}$), and (iii) combined energetic and recombination modulation (labeled as: Reduced ζ) ($E_g = 1.59$ eV, $\zeta = 2 \times 10^{-3}$). Strain effects are represented by a +0.09 eV shift in E_g and a one-order-of-magnitude reduction in ζ.

10^{-3}

For each case, steady-state J–V characteristics were computed under AM1.5 illumination. The extracted performance metrics are summarized in Table 5.2. The corresponding J–V curves are shown in Figure 5.3.

The baseline device exhibits behaviour consistent with experimentally fabricated pristine P3HT:PCBM cells. Increasing E_g from 1.50 eV to 1.59 eV primarily enhances V_{oc}. The voltage rises from 0.6008 V to 0.6893 V. The change in J_{sc} is comparatively small. This behaviour reflects the role of energetic alignment in determining the quasi-Fermi level splitting under illumination. When ζ is additionally reduced from 2×10^{-2} to 2×10^{-3}, both J_{sc} and FF increase significantly. This is consistent with suppressed bimolecular recombination and improved carrier extraction.

The combined modification increases the PCE from 4.22% to 7.96%, corresponding to an 88.5% relative enhancement. The simulated relative increases in J_{sc}, V_{oc}, and FF (22.7%, 22.8%, and 24.9%, respectively) closely match the experimentally observed strain-induced enhancements (21%, 22.5%, and 24%).

The model reproduces the measured strain response when both energetic alignment and recombination are adjusted simultaneously. Importantly, the required parameter changes remain within values reported in the literature.

The present model does not account for strain-dependent mobility, trap-state evolu-

Table 5.2: Electrical model variation in response to strain-induced morphological changes

Modeled parameter variation	J_{sc} (mA cm^{-2})	V_{oc} (V)	FF	PCE (%)
$E_g = 1.50$ eV, $\zeta = 2 \times 10^{-2}$	13.169	0.6008	0.5339	4.2242
$E_g = 1.59$ eV, $\zeta = 2 \times 10^{-2}$	12.766	0.6893	0.5121	4.5055
$E_g = 1.59$ eV, $\zeta = 2 \times 10^{-3}$	16.169	0.7369	0.6673	7.9620
Parameter enhancement (Simulation)	22.7%	22.8%	24.9%	88.5%
Parameter enhancement (Experiments)	21%	22.5%	24%	85%

tion, or spatial strain gradients. The results should therefore be viewed as a test of whether the proposed mechanisms are sufficient to explain the observed behavior, rather than as a detailed microscopic reconstruction.

Taken together, Table 5.2 and Figure 5.3 establish a quantitative link between strain-induced structural modifications and device-scale electrical behaviour. The surrogate parameter approach provides a controlled framework for exploring strain-dependent performance trends in flexible organic photovoltaic systems.

Chapter 6

Strain-Induced Optical and Molecular Transformations in PET Films for Organic Electronic Applications

The contents of this chapter are adapted with the copyright permission from the journal "Advanced Photonic Research." The text has been edited to avoid repetition, particularly in the Introduction, State of the Art, and Methodology sections.

"M. Ghorab, A. K. Ranga, P. Donfack, A. Materny, V. Wagner, and M. Joodaki. "Strain-Induced Optical and Molecular Transformations in Poly(Ethylene Terephthalate) Films for Organic Electronic Applications". Advanced Photonics Research (2025), p. 2500081. doi:10.1002/adpr.202500081."

6.1 Abstract

PET films are widely used in flexible electronics and optoelectronics, where mechanical durability and optical performance under strain are essential for device reliability. This study investigates the effects of cold drawing amorphous PET under ambient conditions. The resulting optical and molecular characteristics are examined using UV–Vis and Raman spectroscopy. It examines how varying strain levels, from 0% (unstretched) to 30%, affect transparency, vibrational modes, and molecular reorganization. UV–Vis absorbance measurements, performed ex-situ after strain release, reveal persistent changes in light transmission, including up to 100% increased absorption in the UVA and visible regions, particularly following large deformations.

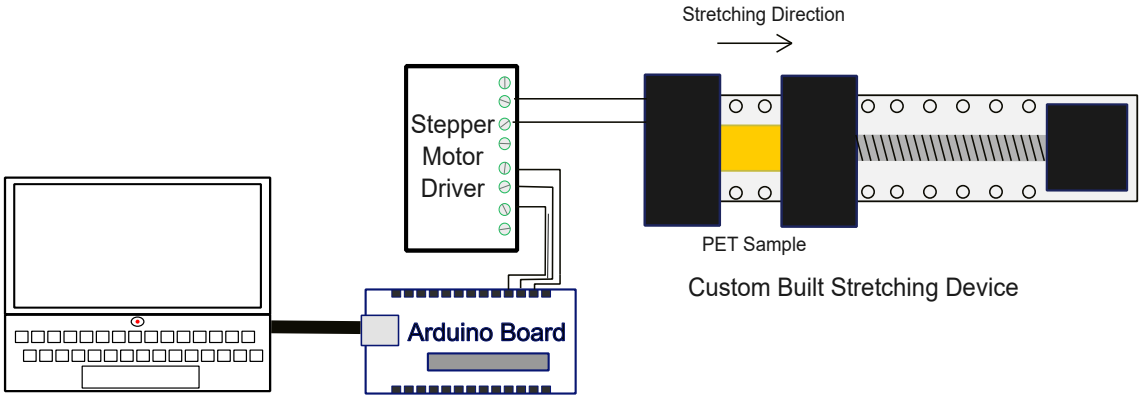

Fig. 6.1: Custom-built stretching device; the stretcher is controlled by an Arduino board, via a motor controller.

Raman spectra show that strains above 5% cause irreversible shifts in vibrational lines and increased FWHM. These spectral changes suggest partial molecular reorientation and emerging structural order, consistent with prior reports on cold-drawn amorphous PET. The phonon mode coupled with C–O stretching [O–CH_2] shows the strongest response to mechanical stress. This work provides insight into strain-induced optical and structural changes in PET, informing strategies to improve the performance of PET-based devices in strain-sensitive applications such as OSCs, Organic Light-Emitting Diodes (OLEDs), and flexible sensors.

6.2 Experimental Methods and Setup

This work has utilized UV–Vis absorption and Raman spectroscopy to examine the optical and vibrational responses of PET films under mechanical strain.
Figure 6.1 illustrates the custom-built stretcher device designed to apply precise, controlled tensile strain to PET samples. Measurements were performed both in-situ and ex-situ, depending on the experimental technique. The device is controlled by an Arduino board, which regulates the application of strain. PET films were securely clamped at both ends of the stretcher and incrementally strained at levels of 1%, 2%, 3%, 4%, 5%, 10%, 15%, 20%, 25%, and 30%.
UV–Vis absorbance measurements were performed on the PET film after each strain exposure. The PET roll used in this study was sourced industrially, originally manufactured as a transparent substrate for OSCs applications, with a density of 16.8×10^5 g/m^3. Owing to its intended use in optoelectronic devices, the material exhibits an amorphous morphology optimized for maximal optical clarity. The films were cut into standardized dimensions of 15 mm × 33 mm to fit the UV–Vis device sample holder size and ensure uniformity throughout the experiments. Each strain level was

maintained for 30 minutes for structural relaxation and accurate spectral measurements. A new, unstretched film was used for each strain value to ensure consistent and independent measurements. The strain was calculated as the percentage elongation relative to the original film length ($\epsilon = \frac{\Delta L}{L}$).

Although in-situ UV–Vis absorption spectroscopy under applied strain would provide real-time insights into optical responses, it was not feasible in the present study due to instrumental constraints. Specifically, the mechanical stretcher could not be integrated within the UV–Vis spectrometer chamber. As an alternative, we employed an ex-situ approach, acquiring absorption spectra immediately after the application and release of mechanical strain. While this method does not capture transient or fully reversible phenomena, it offers valuable insight into persistent optical modifications, residual stress, and strain-induced changes that remain after mechanical relaxation. These observations are particularly relevant for evaluating the stability and optical reliability of polymer substrates under mechanical deformation in flexible optoelectronic devices. Figure 6.2 presents the cross-section of the PET samples before and after strain exposure. Applying strain values greater than 20% induces distortions in the structure, making thickness measurements with an optical microscope difficult due to the appearance of shadows. The thickness of the sample was measured at different positions and an average thickness was calculated from these values (see Fig.6.2). It reduced from an average value of 57.271 μm to 44.342 μm responding to strain.

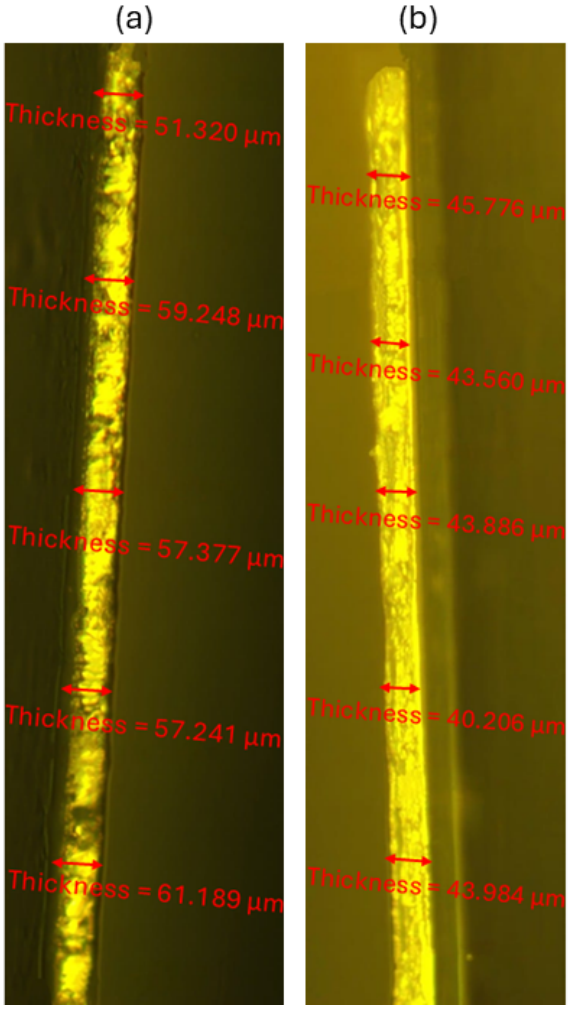

Fig. 6.2: The PET sample's thickness was measured at different positions. (a) without stretching and (b) after 20% stretching; the thickness deduction resulting from the strain exposure is observed. The images were captured using a Carl Zeiss Axiotech 100HD light microscope equipped with an Axiocam 105 color camera.

6.3 Optical and Molecular Responses of PET Under Strain

The interplay between mechanical strain and PET's optical properties is the key focus of this study to gain insights into how structural changes at the molecular level translate to observable optical behaviour. These implications are particularly significant for applications that balance mechanical flexibility and optical device performance, such as OSCs, flexible electronics, and strain sensors [179].
The results are presented in two parts: First, UV–Vis absorption spectroscopy explores how strain affects the optical transparency of PET films, focusing on changes in absorbance across different strain levels. However, while UV–Vis reveals the transparency alterations, it does not provide insight into the underlying molecular mechanisms. To address this, in-situ Raman spectroscopy is employed to uncover the changes observed from vibration modes most sensitive to mechanical deformation, linking molecular reorganization to observed optical variations. These results are discussed in the second part.

6.3.1 Strain-Induced Optical Variations

Panel (a) of Fig. 6.3 shows the UV–Vis absorbance characteristics of an unstretched PET sample at room temperature. Given the transparency of PET in the visible region (400-700 nm), only minimal absorbance is observed. Panel (b) of Fig. 6.3 presents the absorbance spectra of all thin-film PET samples subjected to varying strain levels after stress release. It reflects PET's typical behaviour and intrinsic properties, where the absorption is stronger near the UV region and decreases for higher wavelengths, moving toward the visible spectrum. However, as the strain percentage increases from 1 to 30%, there is a general increase in the absorbance for the UV–Vis spectrum. Increasing strain would lead to higher absorbance values for the PET films, which is particularly noticeable in the mid-range wavelengths (around 400-500 nm). This effect would interrupt the light transmission to the active layer, potentially decreasing the OSCs's efficiency. Figure 6.4 illustrates the absorbance variation in the UV–Vis spectrum. To produce this graph, the wavelength range between 320 and 700 nm was divided into smaller segments, each corresponding to a specific color band of the visible spectrum. The absorbance values within these ranges were summed and normalized to the unstretched values (0%) to represent each color region's overall contribution. These regions were categorized as follows: dark violet range 320-400 nm, purple range 400–450 nm, blue range from 450–495 nm, green range from 495–570 nm, yellow range from 570–590 nm, orange

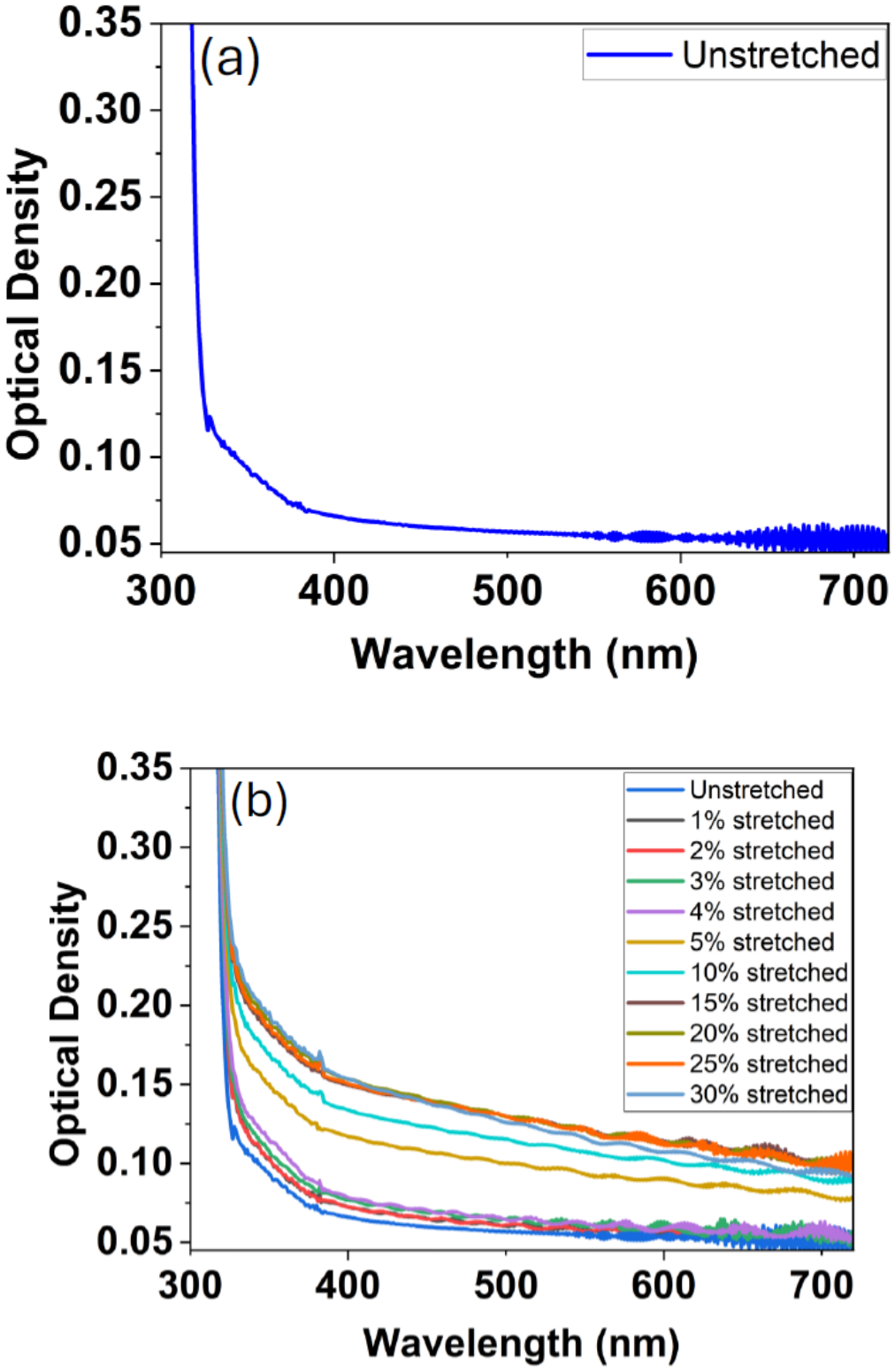

Fig. 6.3: UV–Vis absorbance plots of PET samples: (a) unstretched PET and (b) strained PET.

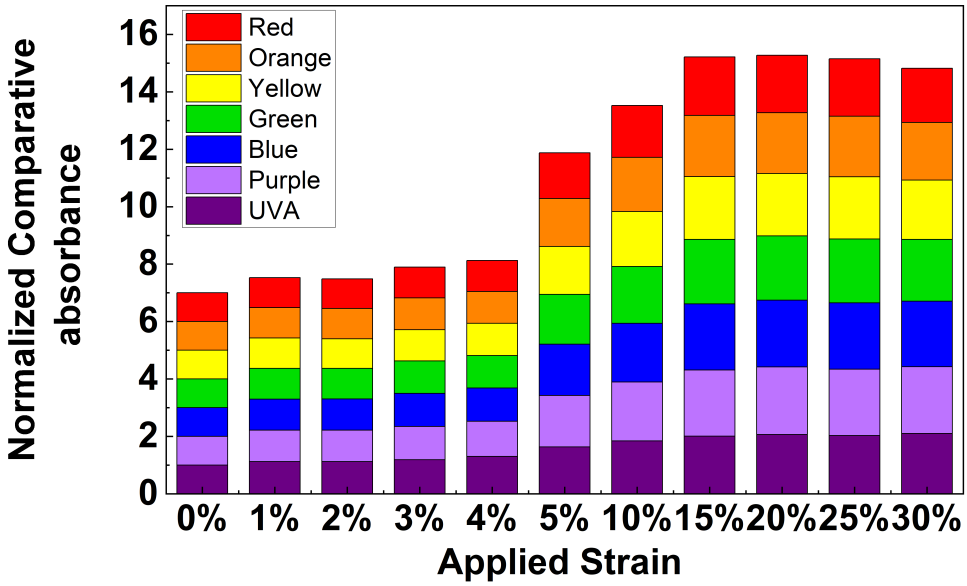

Fig. 6.4: Normalized UV–Vis absorbance of PET films across different visible and UV spectral regions in response to varying residual applied strain. The bar graph highlights the absorbance contributions of specific wavelength ranges (dark violet, purple, blue, green, yellow, orange, and red; see also main text) at strain levels from 0 to 30%, showing a trend of increasing absorbance with higher strain.

range from 590–620 nm, and red range from 620–700 nm. The bars in the graph are color-coded to align with the visible spectrum, visually linking the wavelength ranges to their respective colors. This approach allowed for a clear comparison of the absorbance response of PET thin films under varying applied strains, emphasizing differences in absorbance across the spectral regions. As the strain level increases from 0% (unstretched) to 30%, there is a notable increase in absorbance values, especially for purple and blue wavelengths.

The observed increase in visible light absorption is likely linked to strain-induced structural alterations at the molecular level. Previous studies on stretched PET suggest the formation of localized defects or energy states, which could account for increased visible absorption. However, detailed structural characterization (e.g., spectroscopy at cryogenic temperatures or defect-sensitive electron microscopy) is necessary to confirm the exact nature and presence of such localized states [138, 142]. Furthermore, strain-induced variations in local structural organization—such as partial molecular alignment or the formation of a mesophase—could enhance optical scattering and reduce transparency [115, 139, 140]. Direct verification through complementary structural characterization techniques (e.g., small-angle X-ray scattering, birefringence) is necessary for definitive conclusions regarding crystallinity

or alignment changes. In addition, in-situ UV–Vis absorption spectroscopy, though not employed in the present study, could offer further insight into reversible optical responses during active deformation, particularly in the elastic regime. While our focus remains on persistent, post-deformation optical changes, future studies can benefit from integrating in-situ UV–Vis spectroscopy to better capture transient phenomena associated with strain application.

Furthermore, there is a notable sudden increase in absorbance values, particularly beyond 5% strain. This suggests the presence of a threshold beyond which structural changes in PET—such as mesophase development, increased chain alignment, or a higher density of local packing irregularities—result in significantly elevated light absorption and/or scattering. These effects likely reflect the onset of trans-rich conformational domains and optical anisotropy, phenomena commonly reported in cold-drawn PET systems [115, 139].

6.3.2 Strain-Induced Molecular Variations Probed by Raman Spectroscopy

In applications like OSCs where PET is used as a substrate, the observed changes in optical properties could affect the efficiency of light absorption and conversion, especially under mechanical stress. The transparency reduction in critical wavelengths is important for solar absorption since it reduces the overall performance of the solar cells. These data offer preliminary quantitative insights into how mechanical stress influences the optical response of PET, serving as a basis for future investigations and contributing to the understanding of material behaviour in applications where mechanical and optical properties are coupled.

As mentioned above, in addition to the UV–Vis absorption measurements, we have conducted in-situ Raman spectroscopy on the stretched samples to gain deeper insights into structural alterations under applied strain. This analysis allows us to identify which molecular regions experience greater strain-induced changes and observe the PET molecule's evolution over time while exposed to external strain. We discuss the results in the following section.

The Raman spectroscopy data depicts changes in the orientation of polymer chains, crystallinity, or other structural aspects. Figure 6.5 shows a Raman spectrum of an unstretched piece of PET foil. In this spectrum, 13 main modes are identified, listed in Table 6.1. The modes' response to applied strain is analysed by fitting Voigt profiles to the acquired spectra (see next section). Figure 6.6 presents the demonstration of the corresponding bonds that contribute to the main Raman modes in

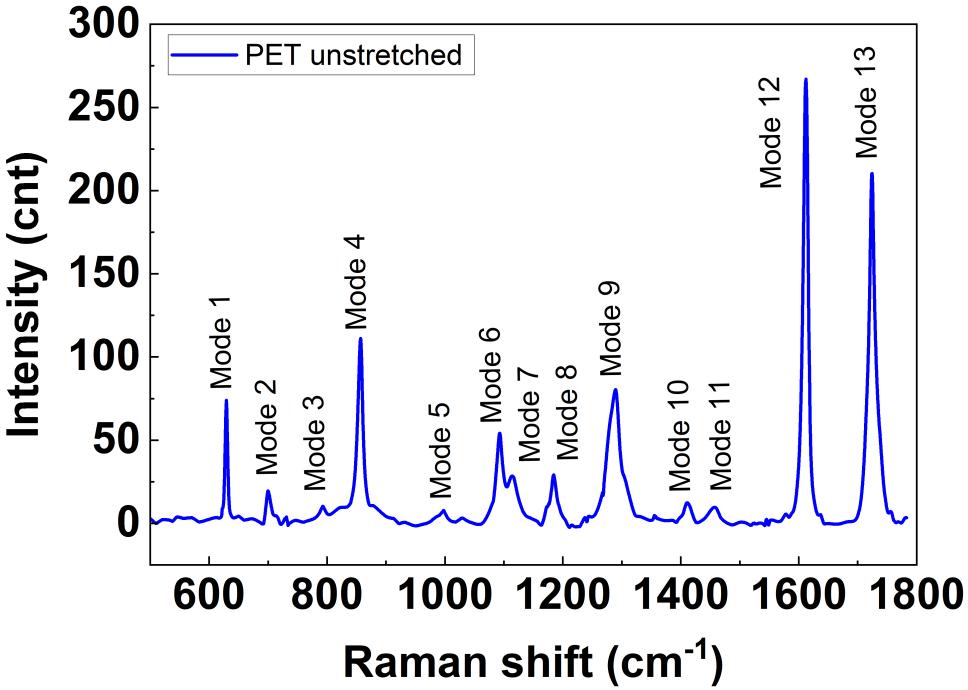

Fig. 6.5: Raman spectrum of an unstretched PET film.

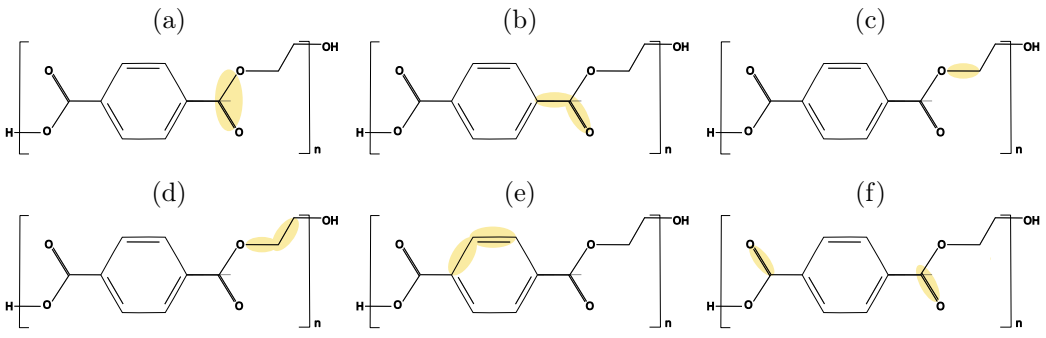

Fig. 6.6: The schematics highlight the affected bonds for each mode, (a) corresponds to mode 1, (b) mode 3, (c) mode 5, (d) mode 6, (e) mode 12, and (f) mode 13.

Table 6.1: Detected main modes in the Raman spectra of a PET sample

Mode order	Vibration mode	Raman shift (cm^{-1})	Conformation
1	Scissors O–C–O [115]	∼637	–
2	–	∼705	–
3	C=O and ring ester C–C out-of-plane bending and ring torsion [118, 180]	∼797	Gauche conformation [115]
4	Ester C(O)–O bending modes [180]	∼858	–
5	C–O stretching [O–CH_2] [118]	∼997	Trans conformation
6	Ester C(O)–O, ethylene glycol C–C stretching [117, 180]	∼1095	Trans conformation
7	Ring C–H in-plane bending, ester C(O)–O and ethylene glycol C–C stretching [117]	∼1119	Gauche conformation
8	CH_2 twisting mode [115]	∼1186	–
9	C(O)–O stretching [117, 180]	∼1292	–
10	C–H bending out of the plane of the benzene ring [117, 180]	∼1417	–
11	CH_2 vibration bending [117, 180]	∼1464	–
12	C–C/C=C stretching modes [180]	∼1613	–
13	Stretching vibration C=O [180]	∼1725	Trans conformation

the PET structure [124].

6.3.2.1 Raman Modes Wavenumber Variation in Response to Applied Strain

Spectra were initially recorded in the unstretched state, followed by strain measurements at 5-minute intervals for 30 minutes (transitional state T_1 to T_6). Additional spectra were captured immediately after applying the strain (T_0) as the first transition state during strain application, and after releasing the sample from stress (labeled Relea. in heatmaps), resulting in a total of 9 recorded spectra per sample, including the unstretched state (labeled Unstrt. in heatmaps). All mode shifts and FWHM values were calculated by subtracting the corresponding unstretched values to assess the deviations. For intensity measurements, the data were normalized to the unstretched state for each sample to better understand the variations induced by stretching.

The Raman modes of the molecules in the sample correspond to specific atomic movements within the molecular structure, such as stretching, bending, twisting, or rocking of molecular bonds (see Table 6.1). The line positions indicate the energy of the vibration mode, which gives information on the strength of the bonds and the changed interactions [181].

Figure 6.7 illustrates the variation of each line in response to strain across different transitional states. A uniform scale was applied across all heatmaps to ensure comparability. The results reveal that the behaviour of the lines varies significantly, some exhibit only minor changes, while others undergo substantial variations when subjected to strain. At low strain levels (1 to 4%), deviations in Raman mode positions are minimal and localized, affecting mainly specific modes such as 5 and 7 (see Table 6.1), corresponding to C-O stretching [$O - CH_2$] and C-C stretching of the ethylene glycol unit. These vibration modes show high susceptibility to minimal mechanical deformation. However, after releasing the strain, most modes return to their original positions, indicating elastic behaviour with high reversibility. As the applied strain increases from 1% to 4%, modest spectral shifts become more pronounced, though they remain limited to a subset of vibrational modes. No evidence of substantial structural reorganization is detected, indicating that the material largely preserves its molecular integrity within this deformation range. This reversible behaviour reflects the resilience and ability of the material to absorb minor mechanical stress without significant structural disruption.

For the moderate strain range (5-10%), the Raman wavenumber shifts become more pronounced, as residual shifts persist after strain release. These shifts suggest the

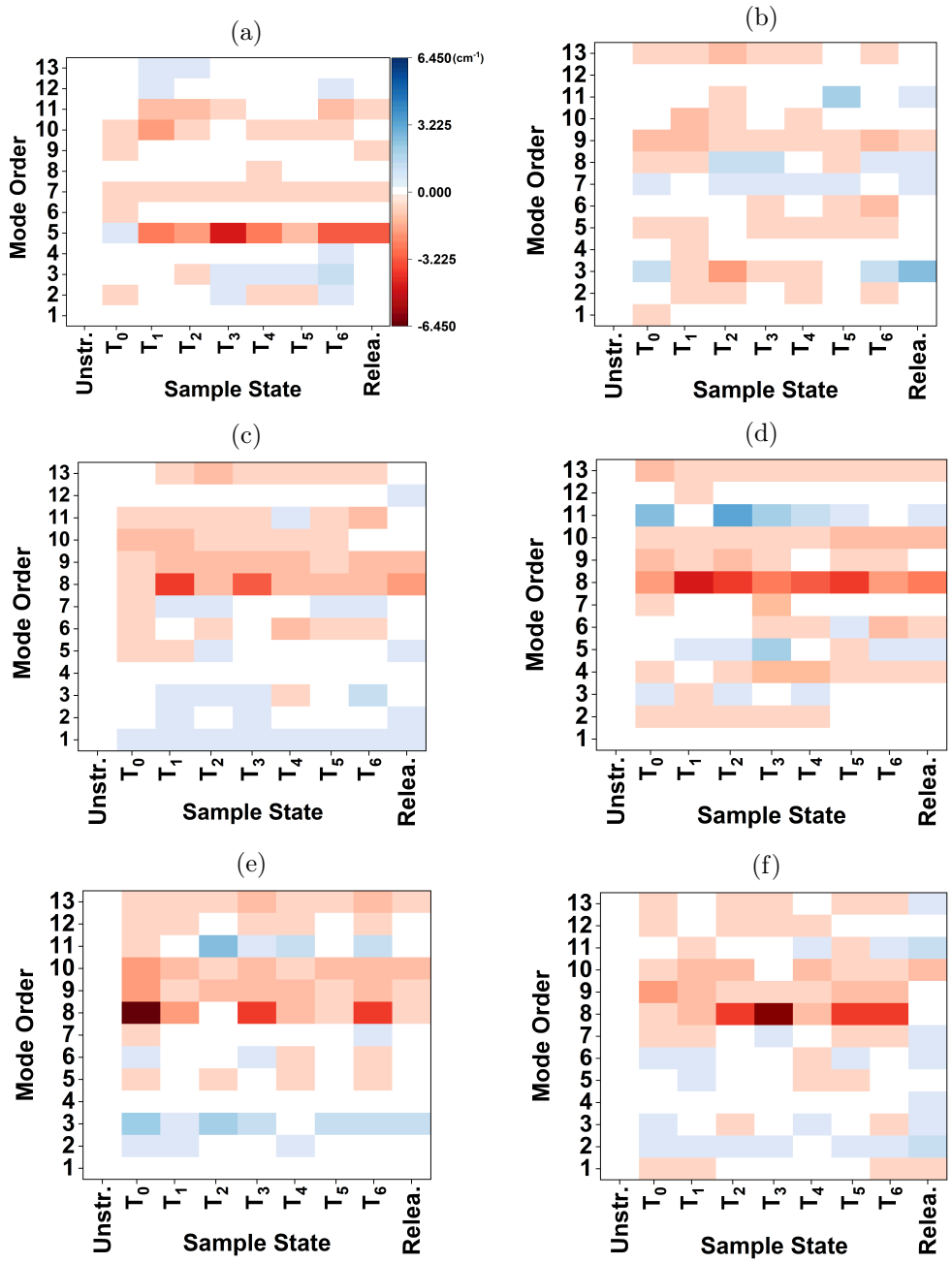

Fig. 6.7: The graphs present the state evolution of relative Raman spectra mode positions for PET under (a) 1% (b) 5%, (c) 10%, (d) 15%, (e) 20%, and (f) 25% applied tensile strain. The heatmaps compare the mode positions at various transitional states (x-axis) from T_0 to T_6 during strain application and after strain release (Relea.) The color bar is unified across different heatmaps. For each sample state, the measured value of each mode is subtracted from the corresponding value in the unstretched state.

onset of molecular reconfiguration, which gradually transitions to more noticeable structural effects. By 5%, the deviations have stabilized across more modes, with cumulative structural effects becoming evident. The eighth mode, associated with CH_2, shows particular sensitivity, marking the transition toward localized but more significant molecular changes. At 10% strain, the shifts become more widespread, impacting multiple modes such as C=O and ring ester C-C out-of-plane bending and ring torsion (mode 3), ethylene glycol C–C and C-O stretching (mode 6), CH_2 twisting (mode 8), and the ester O-C stretching (mode 9). Compared to lower strain levels, the range of spectral deviations narrows slightly but becomes more uniformly distributed across vibrational modes, suggesting a transition from localized to more widespread structural changes. Moreover, the ability of the material to recover baseline spectral positions upon strain release is progressively diminished. This molecular reorganization is accompanied by partial anisotropy, altering optical properties such as transparency (see UV–Vis response). Localized molecular alignment as well as the creation of defects would lead to light scattering and reduced transparency. Modes such as the ninth and eleventh (O-C stretching), which have shown minimal deviations at lower strains, now exhibit significant shifts, suggesting broader structural disruption.

At higher strain levels (15–30%), Raman shifts become pronounced and persist even after strain release, particularly in vibrational modes 5 and 8, consistent with previous reports indicating sensitivity to stress-induced structural rearrangements in PET [182, 183]. Residual spectral deviations suggest permanent structural modifications; however, direct structural characterization (e.g., Wide-Angle X-ray Diffraction (WAXD), electron microscopy) is required to unequivocally confirm the extent and nature of these transformations. At 30% strain, the material is exhibiting a complete transition from elastic to plastic behaviour. Table 6.2 presents a comprehensive overview of the variation in the position of the modes in response to applied stress.

6.3.2.2 Raman Modes FWHM Variation in Response to Applied Strain

The shapes of Raman lines are typically described by Voigt profiles, which are convolutions of Gaussian and Lorentz line shapes. This also considers inhomogeneous broadening mechanisms. In the case of a solid sample, the degree of FWHM broadening is often associated with structural disorder or heterogeneity in the material. As already reflected in the observed wavenumber shifts of the different vibrational modes, strain can introduce various local distortions, such as changes in the lengths or angles of the bonds within the polymer structure [181]. These local variations

Table 6.2: Strain-level effects on Raman line wavenumber positions

Strain Level	**Key Modes Affected**	**Shift Patterns**	**Reversibility After Release**	**Conclusion**
1%	5, 7	Large shifts, localized	High reversibility	Elastic behaviour with minimal residual effects.
2%	5, 7, 10	Minor shifts, more modes affected	Partial reversibility	Increased sensitivity of modes; minimal residual effect.
3%	5, 7, 11	Moderate shifts, more spread across modes	Partial return to baseline	Further deviations, signs of increased sensitivity.
4%	5, 7, 10, 11	Noticeable shift increase with broader deviations	Limited return	Higher structural sensitivity with noticeable changes in mode behaviour.
5%	3, 5, 8	Minor shifts, spread across most modes	Residual shifts remain	Signs of permanent changes, increased structural alterations.
10%	3, 6, 8, 9	Consistent shifts across multiple modes	Strong residual effects	Non-reversible response, extensive molecular changes start.
15%	8, 10, 11	Broader, strong deviations across many modes	Very limited return	High level of alteration with dominant irreversible effects.
20%	3, 8, 9, 10, 11	Large deviations, intense mode shifts	No recovery observed	Severe, likely permanent deformation across molecular structure.
25%	8, 9, 10	Consistent deviations across all modes	No recovery	Extensive reorganization, clear irreversible changes.
30%	All modes	Broad deviations, complete departure	No recovery	Permanent structural alteration, total loss of elasticity.

could shift the mode and broaden it, as the material under strain exhibits a range of slightly different vibration wavenumber due to the nonuniform stress distribution. Since strain often affects each molecular environment differently, the FWHM is sensitive to these subtle differences which can result in larger variations compared to wavenumber mode shifts. FWHM captures the "spread" of stress-induced vibration states while wavenumber shifts reflect overall bond stiffening or softening and slight bond length adjustment, which leads to a shift in the vibration wavenumber. However, this effect is generally more uniform and subtle, reflecting an average change in bond lengths across the material rather than the localized variations contributing to broadening. Therefore, while the wavenumber shift shows a consistent structural adjustment under strain, it does not capture the localized disorder as effectively as FWHM, which is more sensitive to minor variations in molecular structure in response to strain [184] These structural changes are of importance since they can strongly affect the electronic properties of the samples as has been demonstrated earlier [185].

Figure 6.8 shows the variation of FWHM response to different strain values. For a small amount of strain (1 to 4%) relatively strong broadening of FWHM is observed, which is primarily localized to the modes 3 and 5. Broadening stabilizes early around T_4 and show minimal recovery after release.

For midrange strain values (5-10%) a noticeable broadening begins across most modes. At the 5% stretch, it has intensified across modes 3, 8, and 11. Persistent broadening after T_4 with partial recovery occurs after release. This stage can be considered as the initial step for the material to begin its transition from elastic to plastic deformation. Stress spreads across various modes, and strain-induced heterogeneity develops. For 10% stretch, FWHM values remain elevated with minimal but consistent residual effects. showing further structural sensitivity and permanent changes.

At elevated strain (15–30%), Raman mode broadening becomes pronounced and irreversible, suggesting that irreversible deformation dominates, characterized by localized conformational distortions and extensive molecular reorganization. These distortions reflect a breakdown in uniform chain alignment, resulting in permanent structural misalignments that compromise the material's elasticity and lead to long-term mechanical and optical changes. While the observed spectral broadening aligns with known indicators of molecular-level disruptions, complementary structural characterization would be necessary to definitively confirm widespread molecular reorganization [119, 124, 182]. Loss of elasticity and permanent structural changes are observable. Table 6.3 presents a comprehensive overview of the

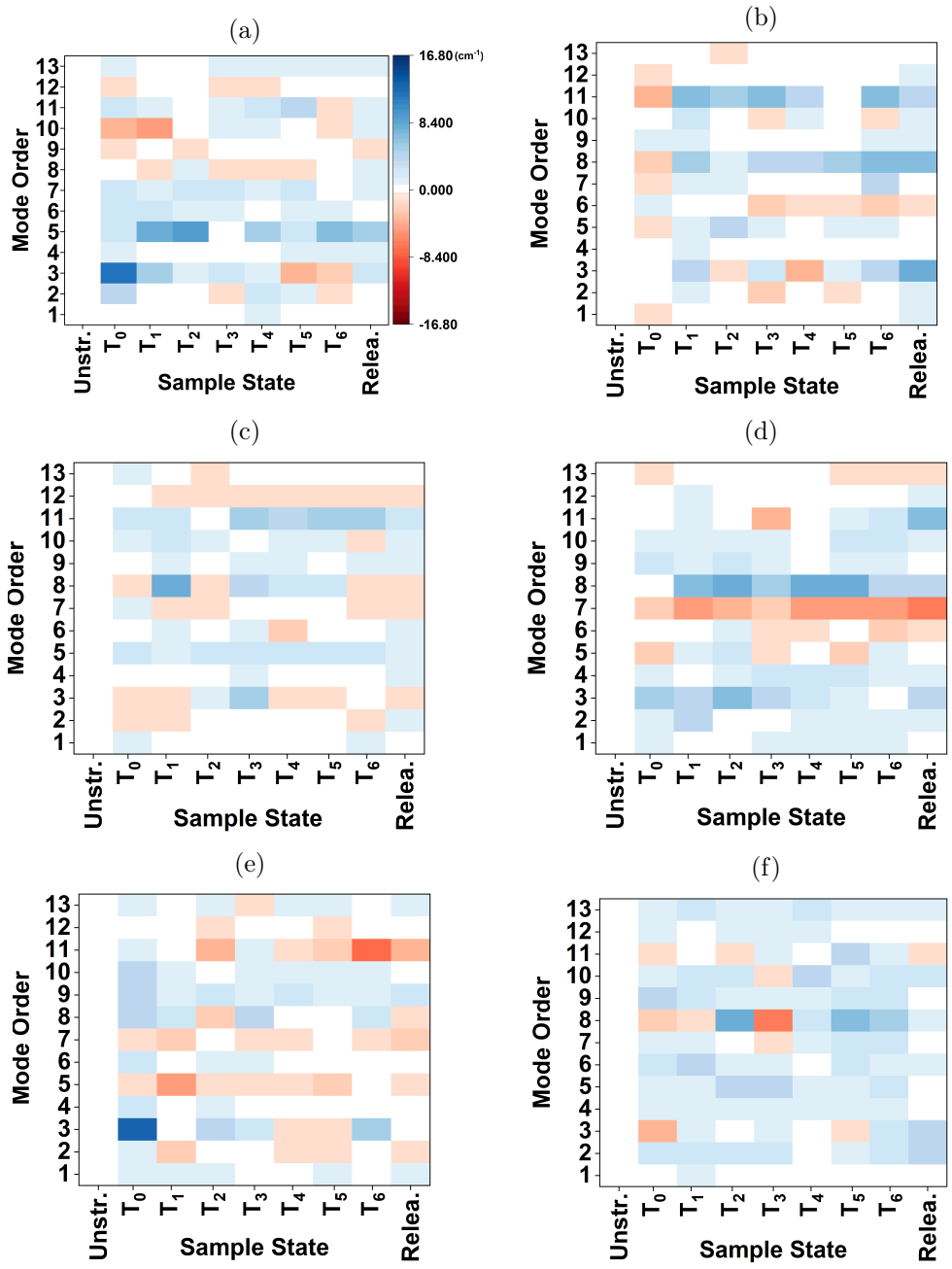

Fig. 6.8: The graphs present the state evolution of relative Raman mode's FWHM variations for PET under (a) 1% (b) 5%, (c) 10%, (d) 15%, (e) 20%, and (f) 25% applied tensile strain. The heatmaps compare the mode's FWHM at various transional states (x-axis) from T_0 to T_6 during strain application and after strain release (Relea.) The color bar is unified across different heatmaps. For each sample state, the measured value of each mode is subtracted from the corresponding value in the unstretched state.

Table 6.3: Summary of strain-level effects and their impact on Raman mode FWHM broadening

Strain Level	**Key modes Affected**	**Shift Patterns**	**Reversibility After Release**	**Conclusion**
1%	3, 5	Large shifts, localized	High reversibility	Elastic behaviour with minimal residual effects.
2%	3, 5, 7	Moderate shifts, mainly localized	Partial reversibility	Early signs of structural sensitivity to strain.
3%	3, 5, 11	Moderate shifts, mainly localized	Partial return to baseline	Increased molecular perturbations, sensitivity rising.
4%	3, 5, 7, 11	Noticeable shifts	Limited return	Enhanced structural changes, limited elasticity.
5%	3, 8, 11	Moderate shifts	Residual broadening remains	Onset of permanent structural alterations.
10%	3, 5, 8, 11	Broad, minimal deviations	Strong residual effects	Major irreversible alterations with dominant effects.
15%	3, 5, 7, 8	Broad, with strong deviations for certain peaks	Very limited return	Major irreversible alterations with dominant effects.
20%	Nearly all modes affected	Small shifts across all modes	No recovery observed	Permanent deformation, structural reorganization.
25%	Nearly all modes affected	Severe, consistent deviations	No recovery	Extensive reorganization, clear irreversible changes.
30%	All modes	Moderate shifts and broadening across all modes	No recovery	Permanent structural alteration, total loss of elasticity.

response to the FWHM variations in the observed mode.

6.3.2.3 Raman Modes Intensity Variation in Response to Applied Strain

The Raman mode intensity is related to the polarizability tensor, which describes how the electron cloud in a molecule deforms in response to incident light. Strain application would cause a change in the Raman intensity due to an alteration in the molecular symmetry of the molecule or crystalline parts of the polymer structure, which affects specific elements of this tensor. In our study, the laser excitation polarization is fixed parallel to the strain axis; therefore, only a subset of the polarizability tensor elements is probed. Under this configuration, the tensor component aligned with the strain direction dominates the response, whereas off-diagonal elements (e.g., α_{xy}) would require polarization rotation or more complex experimental geometries to be accessed [181].

By focusing on a fixed polarization, this study has isolated and examined the strain effects of the Raman-active modes directly along the strain axis. This provides a clear and reproducible dataset without adding the complexity of polarization rotation. Since we have already discussed wavenumber shifts and FWHM variations, adding intensity data completes the picture of the strain impacts on the Raman spectrum. Figure 6.9 presents the intensity heatmaps for various levels of strain. Stretching by 1% causes slight intensity variations initially, but an intense increase when the sample is exposed for a longer time, particularly after the initial 25 minutes (T_5) and after the release. The fifths and eleventh modes exhibit noticeable intensity changes (increased intensity) relative to the unstretched state. At 3% strain, the intensity variations become more pronounced, and all the modes show strong intensity reduction from T_3 to T_6. Despite the wavenumber and FWHM, mostly returning to their initial values after strain release, the intensity does not fully recover to its original level.

For midrange strain values (5 to 10%), strain application results in a decrease in the intensity of modes. 5% strain introduces more intensity fluctuations across multiple modes. Notably, modes 3, 5, and 8 begin to exhibit stronger intensity reduction. The elastic behaviour of the material at low strains likely redistributes the Raman active modes, leading to slight polarization-related intensity shifts. Most changes are reversible upon strain release, while certain modes including 2, 3, and 7 experience an increase in the line intensity. Increasing the strain to 10% leads to a wide reduction in intensity, with modes 2, 3, and 11 showing a pronounced decrease.

At 15% strain, the overall intensity distribution becomes irregular. While the intensity distinctly increases in the low-wavenumber modes including modes 2 and 3,

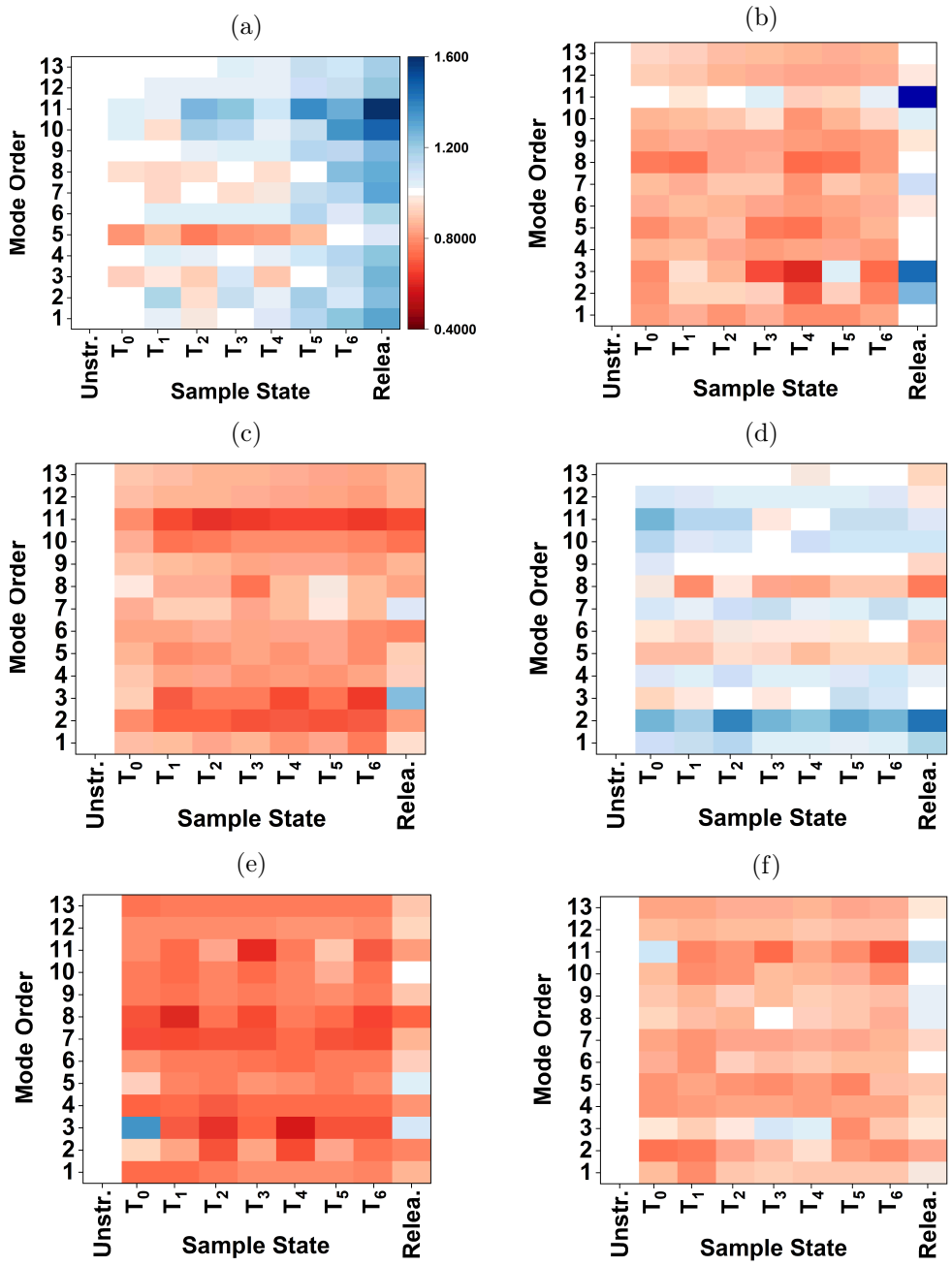

Fig. 6.9: The graphs present the state evolution of normalized Raman line's intensity variations for PET under (a) 1% (b) 5%, (c) 10%, (d) 15%, (e) 20%, and (f) 25% applied tensile strain. The heatmaps compare the mode's intensity at various transitional states (x-axis) from T_0 to T_6 during strain application and after strain release (Relea.) The color bar is unified across different heatmaps. For each sample state, the measured value of each mode is normalized to the corresponding value in the unstretched state.

Table 6.4: Summary of strain-level effects and their impact on Raman mode intensity variation

Strain Level	**Key modes Affected**	**Intensity Patterns**	**Reversibility After Release**	**Conclusion**
1%	5	Minimal intensity changes for low wavenumbers, localized to specific modes	Minimal reversibility	Early signs of molecular alignment; strain-induced changes begin.
2%	5, 11	Small increases in intensity for sensitive modes	Minimal reversibility	–
3%	All modes	High-intensity decrease with broader spread	Partial return to baseline	Increased molecular perturbations affecting polarizability.
4%	5, 7, 11	Noticeable intensity fluctuations across modes	Limited return	Enhanced alignment along the strain axis; tensor alterations visible.
5%	All modes	Intensity changes stabilize	Partial residual changes remain	Onset of permanent molecular rearrangement; altered polarizability.
10%	All modes	Significant intensity deviations	Moderate residual effects	Irreversible alignment and structural deformation dominate the response.
15%	2, 5, 8	Broad intensity changes, concentrated in sensitive modes	Very limited recovery	Major structural reorganization impacts the polarizability tensor.
20%	All modes	Intense deviations with permanent changes across modes	No recovery	Severe deformation, permanent polarizability alterations evident.
25%	6, 10, 11	Strong, consistent intensity deviations across the spectrum	Very limited recovery	Irreversible structural reorganization and strong defect formation.
30%	All modes	Maximum intensity changes, broad and irreversible deviations	No recovery	Total loss of elasticity, complete reconfiguration of polarizability.

modes like 5, 6, and 8 experience a reduction. Limited reversibility is observed upon release. At 20-30% strain, nearly all modes exhibit substantial intensity drop. At 30% strain, the intensity heatmap shows a reduction in intensity for most modes, except the 5, which experiences a strong increase in all states. This suggests selective loss of Raman activity in certain vibration modes while the polarizability of mode 5 is increasing. The near-total loss of reversibility in FWHM and wavenumber data is consistent with the irreversible nature of intensity alterations. Strain-induced molecular alignment creates directional optical properties, which may benefit certain polarization-sensitive applications but compromise isotropic transparency. Table 6.4 presents a comprehensive overview of the observed mode intensity variations response.

6.3.2.4 Analysis of Gauche, Trans, and Amorphous Conformations Under Strain in PET

In PET, the ethylene glycol units exhibit conformational flexibility due to rotation about the central C–C bond. Two primary observed conformations are the trans and the gauche configurations. The trans conformation corresponds to a more extended chain geometry that facilitates intermolecular packing. In contrast, the gauche conformation arises from bond rotation and produces a locally bent structure. The relative population of these conformations directly influences the degree of structural order. Trans conformers favor crystalline or oriented domains, whereas gauche conformers are predominantly associated with amorphous regions.

Modes Associated with Gauche and Trans Conformations

The 1119 cm^{-1} band (mode 7), related to the gauche conformation of ethylene glycol units, exhibits alternating red and blue shifts, with the blue shift dominating for most strain values within the examined range. These shifts reflect the heterogeneous response of PET, where localized chain alignment restricts the rotational freedom of gauche conformers, consistent with the emergence of a mesophase. This phase represents a transitional structural regime between amorphous and crystalline states, distinguished by an increase in trans conformers and partial segmental alignment of polymer chains under strain. This intermediate state has been variously characterized in the literature, most notably as the TX (trans-rich disordered) phase by Cole *et al.* [115], based on Infrared (IR) spectral decomposition, and as a smectic-like mesophase by Keum *et al.* [139] through WAXD analysis of cold-drawn PET fibers. Despite differences in terminology, these studies converge on the recognition of a conformationally ordered yet non-crystalline molecular arrangement that emerges under mechanical deformation. This description more accurately captures

the spectroscopic features and structural characteristics observed in our strained PET samples, without invoking assumptions of specific crystallographic symmetry. Furthermore, in the context of PET's response to strain, heterogeneity refers to the localized and non-uniform molecular behaviour within the material. For mode 7, the observed redshifts are more pronounced at higher strain values, suggesting a slight disruption in intermolecular packing. The FWHM decrease of this mode at low strains is another indicator consistent with the partial alignment of molecular chains.

The 998 cm^{-1} band (mode 5), associated with the trans C–C bond, predominantly exhibits redshifts across all strain levels. At low strains, a pronounced red shift indicates a weakening of intermolecular interactions and packing density. Furthermore, the broadening of FWHM in this mode reflects localized strain-induced distortions.

The 1095 cm^{-1} band (mode 6), associated with C–O stretching in trans conformers, displays smaller but consistent redshifts across all strain levels. This mode represents structurally stable regions, with its FWHM and intensity varying minimally compared to other modes, suggesting that C–O bonds are more resistant to strain-induced disruptions. However, the slight broadening of FWHM remains consistent with the previously mentioned strain-induced distortions.

Modes Associated with Amorphous and PET Structural Integrity

The 1186 cm^{-1} band (mode 8), attributed to CH_2 twisting and associated with amorphous PET, exhibits distinct behaviour under strain. At low strain levels (1–5%), its intensity fluctuates slightly, alternating between increases and decreases relative to the initial value, reflecting localized amorphous regions with a heterogeneous response. This behaviour is consistent with the emergence of a trans-rich mesophase, where some amorphous regions persist while localized alignment initiates. At higher strain levels ($> 5\%$), the intensity consistently decreases, indicating a progressive loss of amorphous character as chain orientation becomes more dominant. Additionally, the FWHM of mode 8 decreases across all strain levels, further reflecting the gradual transition from amorphous disorder to localized molecular alignment and more ordered states. Regarding the wavenumber shifts, alternating red and blue shifts are observed at low strains (1–5%), serving as another indicator of the heterogeneous response of amorphous regions. Beyond 5% strain, pronounced red shifts dominate, signaling significant packing disruptions and molecular bond elongation.

The 1725 cm^{-1} band associated with the carbonyl (C=O) stretching mode is sensitive to the degree of crystallinity in PET, with higher frequencies and sharper peaks indicating a more crystalline structure. At low strain levels (1–5%), the band exhibits minor variations responding to strain. As the strain increases beyond 5%,

a redshift becomes more pronounced, indicating a significant weakening of the intermolecular interactions and an increased disruption of the density of the packing of chains. The reduction in the intensity of this band at higher strain levels aligns with growing disorder within the molecular structure, consistent with transitions observed in other vibrational modes.

6.4 Correlation of Raman and Absorption Spectroscopy Findings

The optical properties of PET under strain are intrinsically linked to its molecular structure, particularly the interplay between its amorphous and crystalline states, as well as strain-induced perturbations in molecular conformations and functional groups. In the amorphous state, PET consists of disordered polymer chains with a uniform refractive index, minimizing light scattering and maintaining high transparency. In contrast, the crystalline state introduces highly ordered and densely packed polymer chains, forming crystalline domains with refractive indices distinct from the surrounding amorphous regions. These boundaries scatter light, progressively reducing transparency as the degree of crystallinity increases. Strain exacerbates this effect by inducing structural transitions, creating defects, and perturbing chain packing, further enhancing light scattering and reducing transparency [119].
The integration of Raman and UV–Vis findings underscores the critical role of strain-induced molecular alignment and phase transitions in governing PET's optical behaviour. The detailed behaviour of key vibrational modes—the 998 cm^{-1} (mode 5), 1095 cm^{-1} (mode 6), 1119 cm^{-1} (mode 7), 1186 cm^{-1} (mode 8), and 1725 cm^{-1} (mode 13) bands—provides a molecular-level understanding of how strain influences structural evolution.
At low strain levels (1–4%), PET maintains its transparency with negligible changes in optical properties. The Raman spectra suggest minimal molecular reorientation and negligible phase transitions, aligning with the absence of significant variations (up to 20%) in the UV–Vis absorption spectra, indicating preserved transparency and molecular integrity.
As strain increases to intermediate levels (5–10%), PET's optical properties begin to show measurable changes. The Raman study offers a unique perspective on molecular-level order sensitivity in the response of PET to mechanical strain. This paves the way for future research to explore polarization-dependent measurements and the engineering of PET films with controlled molecular orientations, which introduce variations in the refractive index and result in light scattering and reduced

transparency. UV–Vis spectra corroborate these findings, showing an increase in absorbance to up to 90% for the 10% applied strain in the visible spectrum, particularly in the blue and purple regions, due to structural transitions.

At higher strain levels (15–30%), irreversible spectral features including substantial peak broadening and intensity reduction in critical vibrational modes strongly suggest disruptions in molecular organization and partial structural disorder. Similar Raman signatures have been previously correlated with structural rearrangements in mechanically strained PET. However, explicit confirmation of the detailed structural transformations described here requires additional characterization, which we recommend for future investigations [182, 183]. UV–Vis absorption spectroscopy reveals an increase in absorbance exceeding 100% relative to the unstrained state, which is attributed to enhanced optical scattering and possible changes in molecular packing. This may reflect the development of mesophase ordering or conformational rearrangements that reduce the optical bandgap, potentially due to increased local packing irregularities or strain-induced electronic inhomogeneities. The observed spectral changes suggest that residual stresses and associated structural heterogeneity induced by strain could contribute to the observed significant transparency loss and reduced optical clarity. This interpretation is supported by previous findings correlating stress-induced optical degradation with structural non-uniformities in PET [138, 142]. Additionally, optical anisotropy becomes pronounced, as strain-induced molecular alignment creates directionally dependent optical properties. Raman intensity variations further emphasize PET's sensitivity to strain, with an average 30% reduction in Raman line intensity across all modes at 20% applied strain.

As mentioned earlier, the Raman spectroscopy measurements were conducted while the PET samples were held under strain for 30 minutes at room temperature. Instead of a single transient state, multiple transient states were observed in the intermediate spectra, reflecting ongoing molecular adjustments. This behaviour can be attributed to the inherent rigidity of PET at room temperature, which influences molecular mobility and limits immediate large-scale rearrangements. The observations suggest that PET's molecular response under strain at room temperature primarily involves localized and gradual adjustments, rather than long-range relaxations occurring within a short time frame. This structural rigidity may also explain the dominance of heterogeneous responses in key Raman modes, as strain-induced changes in the amorphous and crystalline regions remain localized.

Beyond the spectroscopic interpretation, these findings also carry practical implications for applications where mechanical deformation influences optical or molecular behaviour. Manufacturers can develop PET films with improved strain resistance,

ensuring reliability in demanding environments by understanding the strain thresholds at which irreversible changes occur (e.g., above 10–15% strain). The pronounced intensity, FWHM, and wavenumber variations in Raman spectra under strain could be harnessed to create susceptible, polarization-dependent Raman sensors [186]. These sensors would be capable of precisely detecting localized stress or strain, making them ideal for applications in structural health monitoring or wearable electronics. By correlating strain-induced structural changes with optical degradation, the study offers a framework for predicting the operational stability of PET-based devices, allowing for better material selection and design [63].
Moreover, the implications of this work can extend to other industries where PET is widely used, such as packaging and structural films. In mechanical engineering, PET's robustness under strain is crucial for applications like protective films and load-bearing components. The insights from this study can guide the development of PET materials with enhanced mechanical properties, such as higher tensile strength and improved elasticity. Understanding how strain impacts PET at a molecular level can aid in designing packaging materials that maintain transparency and durability under various stresses, contributing to sustainable and high-performance solutions. The study's focus on fixed polarization provides insight into the anisotropic Raman response of PET under mechanical strain. These findings suggest that polarization-dependent Raman configurations could be strategically optimized to enhance strain sensitivity in future sensing applications. Furthermore, controlling molecular orientation in PET films may enable the tailoring of optical and mechanical properties for application-specific requirements.

6.5 Conclusion

This study offers preliminary but scientifically grounded insights into the optical and structural responses of PET films subjected to mechanical strain under strictly ambient (room-temperature) conditions, without thermal annealing. By integrating UV–Vis absorption and Raman spectroscopy, the work elucidates the interplay between molecular conformation and optical behaviour, capturing strain-induced effects that are distinct from those observed under elevated-temperature processing. At strain levels below 5%, PET maintains its optical transparency and molecular integrity, exhibiting only minor conformational adjustments and minimal chain alignment. These characteristics underscore its suitability for low-deformation applications such as optical coatings and flexible sensors. Beyond this threshold, more pronounced structural transitions occur, including increased chain orientation and

the emergence of mesophase-like order, which contribute to optical anisotropy and enhanced light scattering, thereby reducing transparency. These observations are critical for informing strain thresholds in applications such as flexible displays and photovoltaic layers, where optical performance is tightly constrained.

At higher strain levels (15–30%), the material undergoes irreversible structural reorganization, characterized by disrupted packing, conformational heterogeneity, and a breakdown of isotropic optical properties. These changes result in diminished transparency and elasticity but suggest promising utility for PET in strain-sensitive and polarization-dependent optical devices.

In summary, this work contributes to the growing understanding of strain-induced molecular reordering in PET under non-thermal, realistic processing conditions, a regime often underrepresented in the literature. While structural confirmation via advanced techniques lies beyond the present scope, the spectroscopic findings are consistent with prior studies reporting trans-rich conformational transitions and mesophase formation in similarly treated PET systems. Future work incorporating wide-angle X-ray diffraction, microscopy, birefringence analysis is encouraged to further validate and extend the insights established here.

Chapter 7

Assessing bandgap Stability of Poly(3-hexylthiophene-2,5-diyl)(P3HT) Thin-Films Under Uniaxial Tensile Strain for Flexible Electronic Applications

The contents of this chapter are adapted, with the permission of all authors, from a manuscript that has been resubmitted to the journal IEEE Access after the first round of review. The text has been edited to avoid repetition, particularly in the Introduction, State of the Art, and Methodology sections.

"M. Ghorab, A. K. Ranga, A. Materny, V. Wagner, and M. Joodaki. "Assessing bandgap Stability of Poly(3-hexylthiophene-2,5-diyl) (P3HT) Thin-Films Under Uniaxial Tensile Strain for Flexible Electronic Applications. IEEE Access, vol. 14, pp. 48672-48682, 2026, doi: 10.1109/ACCESS.2026.3678138"

7.1 Abstract

Organic semiconductors intended for flexible electronic applications must retain stable optoelectronic properties under mechanical deformation. Since the optical bandgap governs exciton generation and constrains photovoltaic voltage, its robustness under strain is a critical requirement for reliable device operation. In this work, we investigate strain-induced bandgap variations in P3HT thin-films deposited on flexible PET substrates, studied both as single layers and in PEDOT:PSS/P3HT

stacks. The samples were subjected to controlled uniaxial tensile strains in the range of 1%–10%.
The optical bandgap was extracted from ultraviolet–visible (UV–Vis) absorption spectra using a standardized Tauc analysis, with statistical validation based on robust regression and equivalence testing. For all stacking configurations and annealing conditions, the bandgap remains unchanged within experimental resolution up to 7% strain. At 10% strain, a small but consistent increase of approximately 4–5 meV is observed. This threshold-like response indicates a transition from mechanical strain accommodation dominated by morphological relaxation to a regime in which electronic perturbation becomes detectable.
These results establish a quantitative strain window over which P3HT-based thin-films can be regarded as optically stable and provide practical guidance for mechanical modeling and the design of flexible organic optoelectronic devices.

7.2 Introduction

In this study, we investigate whether mechanical strain in the range of 0–10% alters the optical bandgap of P3HT thin-films deposited on flexible PET substrates, both as single layer and in PEDOT:PSS /P3HT stacks. In practical applications such as foldable displays or wearable electronics, the tensile strain experienced by polymer substrates and electrode stacks is typically only a few percent. Values in the range of 1–5% are most commonly reported as the limit for reliable operation before mechanical degradation sets in [187].
The 1–7% window investigated in this study therefore encompasses and slightly exceeds realistic device conditions. By contrast, the 10% condition represents a deliberately severe deformation, included here to reveal the strain threshold at which measurable electronic changes begin to appear. To this end, we applied controlled tensile deformation using a custom-built stretcher and performed UV–Vis absorption spectroscopy before and after stretching, extracting the bandgap through a standardized Tauc analysis. This framework enables a quantitative assessment of bandgap stability under macroscopic strain, allowing us to distinguish between a strain-invariant operating regime and the emergence of a threshold-like electronic response at higher deformation. As such, the present study provides a device-relevant benchmark for the optical robustness of P3HT-based thin-films under tensile strain.

7.3 Experimental Setup and Methods

In this study, strain values of 1%, 3%, 5%, 7% and 10% were applied. The strain (ε) was calculated as the ratio of the applied elongation ΔL to the initial gauge length L_0 ($\varepsilon = \Delta L/L_0$). All stretching and optical measurements were performed under ambient room temperature conditions, ensuring no softening or morphological changes associated with elevated temperatures.

To ensure that the reported absorption spectra reflect only the active organic layers, the optical contribution of the PET substrate was explicitly accounted for. In a previous study, we characterized the strain response of bare PET under the same tensile conditions used here [31]. That dataset was used to subtract the PET baseline from all spectra collected in this work. As a result, the reported absorption and extracted bandgaps correspond solely to P3HT or PEDOT:PSS/P3HT films, with any PET-related absorption or strain effects removed.

Strain application in this work followed a strain protocol as follows: each sample was first measured in its pristine state, then subjected to a fixed tensile strain for 30 minutes using the stretcher. After this period, the strain was released, and the film was immediately transferred back to the spectrometer for re-measurement. Importantly, no relaxation time was allowed between strain release and optical characterization, ensuring that the spectra captured the post-deformation state of the film. To avoid artifacts from strain history, a fresh film was used for each strain level. Fig. 7.1, depicts the schematic of this setup.

Mechanical strain in thin-film organic semiconductors can be investigated using several complementary experimental modalities, including in-situ measurements under applied load, cyclic or fatigue deformation, localized strain-induced by bending radius or buckling, hydrostatic or pressure-based loading, and post-deformation analyses that probe persistent structural changes after unloading. Each approach emphasizes different aspects of the strain–property relationship and addresses distinct physical and device-relevant questions [144, 188, 189].

In this study, we focus on the post-deformation case. Here, “residual strain” refers to structural modifications in the organic layer that persist after the release of an applied tensile load, rather than a direct measurement of sample elongation before and after stretching. This ex-situ approach probes the optical response of the film in its post-deformation state, capturing changes that remain after mechanical loading. By performing the measurement after unloading, it isolates structural contributions to the optical response from instantaneous mechanical perturbations. This makes it possible to determine whether deformation leaves a measurable electronic signature in the film. Such a framework is particularly relevant for evaluating the practical

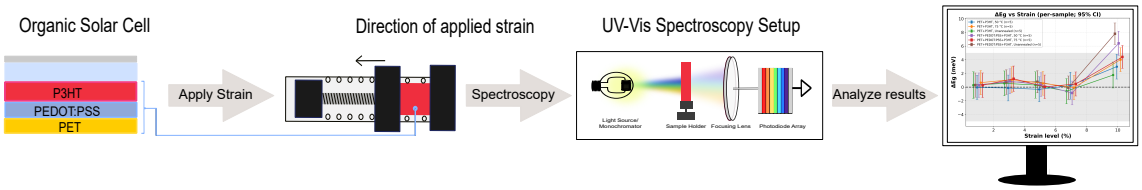

(a)

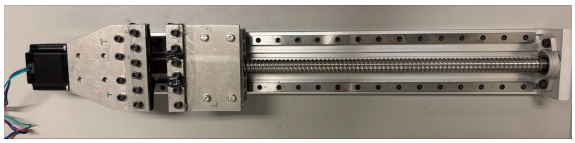

(b)

Fig. 7.1: Two-panel overview of the measurement workflow and apparatus. **(a)** Schematic illustration of the experimental workflow. Samples were first characterized by UV–Vis spectroscopy in their unstretched state, then subjected to tensile strain for 30 minutes using a motorized stretcher, and subsequently transferred back to the spectrometer for a second UV–Vis measurement. **(b)** Photograph of the custom motorized stretcher used to apply strain. Note that the mechanical straining and optical measurements were performed sequentially (ex-situ).

strain tolerance of thin-film devices. It allows the identification of a strain window over which the bandgap remains effectively invariant, as well as the onset of a threshold beyond which persistent changes become detectable. Because the UV–Vis measurements are performed ex/situ, this approach does not resolve transient electronic responses during active deformation and does not separate instantaneous strain effects from those accumulated during loading. In-situ measurements under applied strain are therefore of fundamental interest but fall outside the scope of the present work.

7.3.1 Tauc Analysis and Optical bandgap Extraction

The electronic bandgap in organic semiconductors can be characterized through multiple, complementary approaches. The fundamental gap, defined as the energy difference between the Valence Band Maximum (VBM) and Conduction Band Minimum (CBM), represents the intrinsic electronic structure of the material. This quantity can be accessed via first-principles band-structure calculations, or experimentally through the combination of Photoelectron Spectroscopy (PES) and Inverse Photoelectron Spectroscopy (IPES), which directly probe the ionization and electron affinity levels, respectively [190]. In contrast, electrochemical techniques such as Cyclic Voltammetry (CV) produce the transport gap, corresponding to the en-

ergy required to generate free charge carriers, defined by the difference between the Ionization Potential (IP) and Electron Affinity (EA) [191].
In conjugated polymers, optical excitation typically generates bound excitons rather than free charges, due to the low dielectric screening and strong Coulomb interactions [192]. As a result, the optical gap, which dictates the absorption onset, is systematically smaller than the transport gap by the exciton binding energy. This optical transition plays a central role in defining the spectral window for photon harvesting and constrains the achievable V_{oc} in organic photovoltaics [89]. Optical properties of P3HT can be deduced in reflection geometry by ellipsometry or modulation spectroscopy [193], or more convenient in transmission by UV–Vis absorption. However, precise extraction of the optical gap from UV–Vis absorption spectra is often hindered by vibronic fine structure and inhomogeneous broadening arising from energetic disorder [87].
To determine the optical bandgap, we employed the Tauc method [102, 103]. Although this method was originally formulated for interband transitions in inorganic semiconductors, it remains the standard approach for extracting a comparative optical gap in conjugated polymers, including P3HT. Since these materials exhibit bound excitons and vibronic structure, the Tauc-derived E_g represents an effective onset energy rather than a fundamental excitonic transition. Nevertheless, its widespread use in the OSC literature provides a consistent and reproducible framework for comparing bandgap shifts across processing conditions and strain levels. This method relates the absorption coefficient α to photon energy $h\nu$ as:

$$(\alpha h\nu)^{\frac{1}{n}} = B(h\nu - E_g), \tag{7.1}$$

where α is the absorption coefficient, h is Planck's constant, ν is the photon frequency, E_g is the optical bandgap, B is a proportionality constant, and n is the transition exponent that depends on the nature of the electronic transition ($n = \frac{1}{2}$ for direct allowed transitions and $n = 2$ for indirect allowed transitions) [194–199]. In this study, decadic absorbance A was used in place of the absorption coefficient α to eliminate the influence of film thickness variations on the bandgap determination. Since $\alpha = (2.303/d)A$, where d is the film thickness. In this work, film thickness was verified by stylus profilometry on representative samples prepared under identical processing conditions, yielding nominal thicknesses of approximately 200 nm for P3HT and 25 nm for PEDOT:PSS, consistent with prior reports under similar deposition conditions [132]. The film thickness was not measured individually for every specimen analysed, which is acknowledged as an experimental limitation. However, since the optical bandgap is extracted from the intercept of the Tauc con-

struction, using the absorbance (A) directly in place of the absorption coefficient (α) merely rescales the vertical axis of the Tauc plot without affecting the x-intercept that defines E_g. As a result, residual sample-to-sample thickness variations, which is typically on the order of tens of nanometers for solution-processed films, do not influence the reported E_g values. This approach therefore provides a more robust and reproducible basis for comparative bandgap analysis while decoupling the results from uncertainties associated with precise thickness determination.

For P3HT we adopted $n = 1/2$, which is considered for direct bandgap semiconductors [89, 200]. For each specimen, three spectra were recorded, averaged, and smoothed with a Savitzky–Golay filter (polynomial degree 3). The absorbance spectrum was converted to photon energy using $h\nu\ [eV] = 1240/\lambda\ [\text{nm}]$, where λ is the wavelength, and the Tauc variables were defined as $x = h\nu$ and $y = (Ah\nu)^2$. To ensure a robust and reproducible determination of the optical bandgap, the Tauc analysis was performed within a fixed energy interval from 1.90 to 2.026 eV. This interval was chosen to capture the lowest-energy linear rise associated with the absorption onset of P3HT, while excluding sub-gap tail states at lower energies and vibronically structured absorption at higher energies. Within this interval, multiple equally sized sub-windows were systematically evaluated.

Linear fits were performed using Ordinary Least Squares (OLS) in centered form:

$$y = m(x - \bar{x}) + b_c, \tag{7.2}$$

where $\bar{x}$ is the mean energy in the window, m the slope, and b_c the centered intercept. The bandgap was obtained from the x-intercept:

$$E_g = \bar{x} - \frac{b_c}{m}. \tag{7.3}$$

Uncertainty in E_g was estimated by error propagation (delta method) from the regression covariance matrix of m and b_c, using:

$$\frac{\partial E_g}{\partial m} = \frac{b_c}{m^2}, \qquad \frac{\partial E_g}{\partial b_c} = -\frac{1}{m}. \tag{7.4}$$

This yielded standard errors (SEs) and 95% confidence intervals (CI) for each fit. Among all fixed-length windows within the chosen interval, the optimal fit was defined as the one with the smallest SE, provided that the coefficient of determination (R^2) exceeded 0.995 and the residuals showed no curvature. This window selection procedure was applied consistently across all samples and strain conditions, ensuring that the extracted bandgap values are not biased by window selection or non-linear

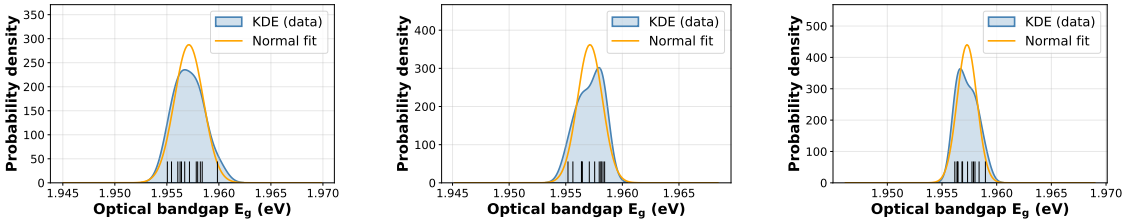

(a) Unannealed (b) 50°C (c) 75°C

Fig. 7.2: KDEs of the optical band gap E_g under three annealing conditions, with fitted normal distributions for reference. KDEs use a Gaussian kernel (base function) and Scott's bandwidth rule ($h = \sigma n^{-1/5}, n = 12$) [201]. Rug marks along the axis show the 12 measured E_g values for each condition.

spectral regions. To account for instrument resolution, the 1 nm spectral resolution (≈ 3–5 meV at the P3HT onset) was adopted as the detection limit.

Twelve independent spectra were analysed for each annealing condition (unannealed, 50 °C, 75 °C), reflecting the total number of experiments conducted per condition and stacking configuration. The extracted bandgap values were then aggregated into condition-specific descriptor sets. For each set, the arithmetic mean bandgap ($\overline{E}_g$) was reported as the central value, with the sample standard deviation (SD, σ) and variance (σ^2) quantifying variability arising from sample-to-sample fabrication differences. A 95% CI for the mean was calculated using the Student's t-distribution, $\overline{E}_g \pm t_{0.975,n-1} \cdot \sigma/\sqrt{n}$, to capture statistical uncertainty.

In parallel, R^2 values from individual linear fits were averaged to provide an overall metric of fit quality. Fig. 7.2 visualizes the distribution of E_g values across annealing conditions, kernel density estimates (Kernel Density Estimates (KDEs)) were plotted and overlaid with fitted normal distributions. These plots reveal narrowly distributed profiles that closely follow the fitted Gaussian functions, verifying the adequacy of a single-Gaussian description of the data. The use of twelve extracted E_g values per condition to construct both the KDE and the Gaussian fit reflects fabrication-induced variability follows a normal distribution. The small differences between KDE curves and the Gaussian fits can be attributed to the limited sample size ($n = 12$), rather than to systematic deviations from normality. A summary of the extracted parameters, including mean E_g, SD, CI, and average R^2 is provided in Table 7.1.

The baseline values of E_g for unstrained P3HT films under different annealing conditions are summarized in Table 7.1. The mean values differ by less than 0.1 meV across conditions, indicating that the average optical gap remains essentially unchanged within experimental uncertainty. However, the width of the 95% CI narrows upon annealing, decreasing from 1.7 meV in the unannealed state to 1.1 meV

Table 7.1: Summary of optical bandgap parameters for P3HT films. Values averaged over 12 spectra per condition.

Anneal condition	Mean E_g	SD	95% CI	Mean R^2
Unannealed	1.9571	0.0013	1.9562 – 1.9579	0.997
50°C	1.9571	0.0011	1.9564 – 1.9578	0.997
75°C	1.9572	0.0009	1.9567 – 1.9578	0.997

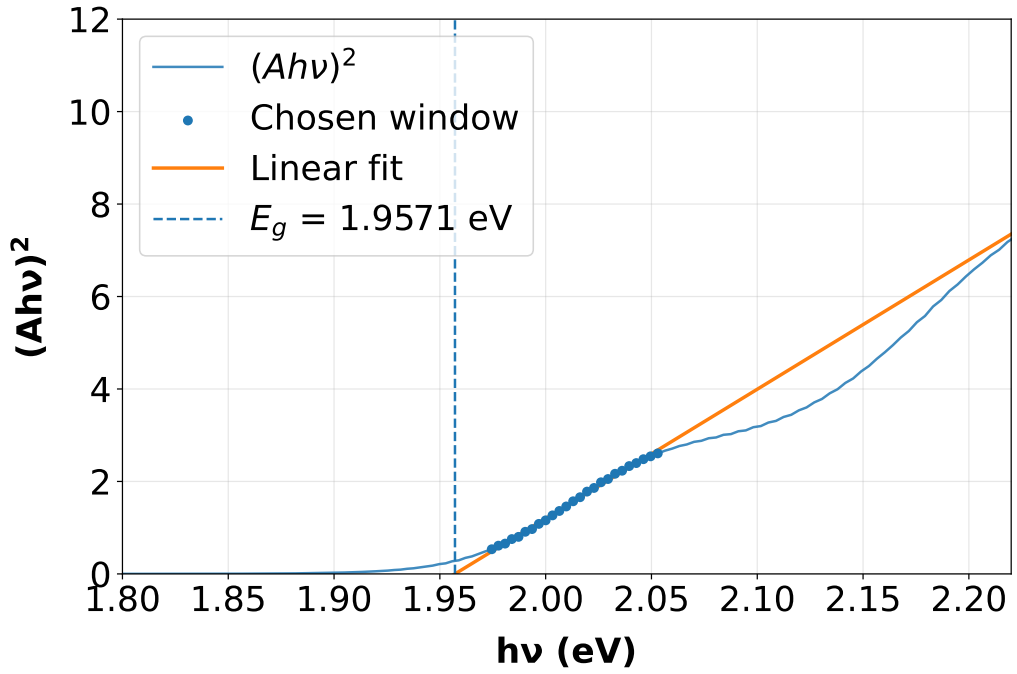

Fig. 7.3: Representative Tauc plot illustrating the method used to extract the optical bandgap E_g. The straight line corresponds to the optimal linear fit within the selected onset region, and the dashed vertical line marks the intercept used to determine E_g.

at 75 °C. This reduction in variability reflects improved structural order and more uniform film morphology. At the relatively low annealing temperatures applied here, the dominant effect is thus a suppression of energetic disorder rather than a pronounced shift in the mean bandgap. These temperatures correspond to commonly employed fabrication protocols for P3HT-based organic solar cells on flexible substrates, where annealing is usually restricted to below ∼80 °C. This observation is consistent with prior reports showing that thermal treatment enhances crystallinity in poly(3-alkylthiophenes) [132, 202, 203]. Fig. 7.3, depicts the Tauc method plot, which is used for the bandgap extraction.

7.4 Results and Discussion

To access the effect of mechanical strain on the optical bandgap, we calculated the per-sample difference

$$\Delta E_g = E_{g,\text{post}} - E_{g,\text{pre}},$$

where $E_{g,\text{pre}}$ and $E_{g,\text{post}}$ denote the bandgaps measured before and after strain application, respectively. The uncertainties from the Tauc fits were carried through so that each ΔE_g value came with its own estimated error. The data were then grouped according to strain level, stacking configuration, and annealing temperature.

Across all conditions, the resulting shifts are generally small (on the order of a few meV). These values often fall within the experimental resolution limit of ± 5 meV, which is determined by the 1 nm spectrometer step size. Fig. 7.4 presents the aggregated results as ΔE_g versus strain, with 95% CIs. For strains up to 7%, the mean values fluctuate around zero and remain largely confined within the resolution band which would suggest the absence of a systematic effect. However, at 10% strain, all groups exhibit a reproducible increase in E_g of approximately 4–5 meV, which, while modest in magnitude, clearly exceeds the estimated statistical noise.

Considering that each strain level was measured on an independent specimen (i.e., one specimen per strain and per condition), the present dataset does not include between-specimen replication of ΔE_g at a fixed strain level (e.g., multiple independent measurements at 1% strain), which is acknowledged as an experimental limitation. The reported uncertainty therefore reflects the propagated Tauc-fit uncertainty and within-specimen spatial variability (three measurement positions). The strain dependence is assessed using pooled equivalence testing over the 1–7% strain range and robust regression contrasts comparing the 10% strain condition to the pooled 1–7% dataset.

These observations suggest a threshold-like response in the optical bandgap, which is stable under moderate strain but increases noticeably upon entering the 10% regime. Two key questions arise from this behaviour: (i) can the apparent minor variations below 7% be regarded as statistically negligible within experimental limits. (ii) how robust is the observed increase at 10% when we consider two matters: first, we must ensure that the pooled effect is not driven by a single experimental subgroup. In particular, no individual annealing or stacking condition should disproportionately influence the observed the 10% increase. Second, the regression model used to quantify this effect should remain valid even if the data deviate from ideal statistical assumptions, such as having constant error variance or normally distributed

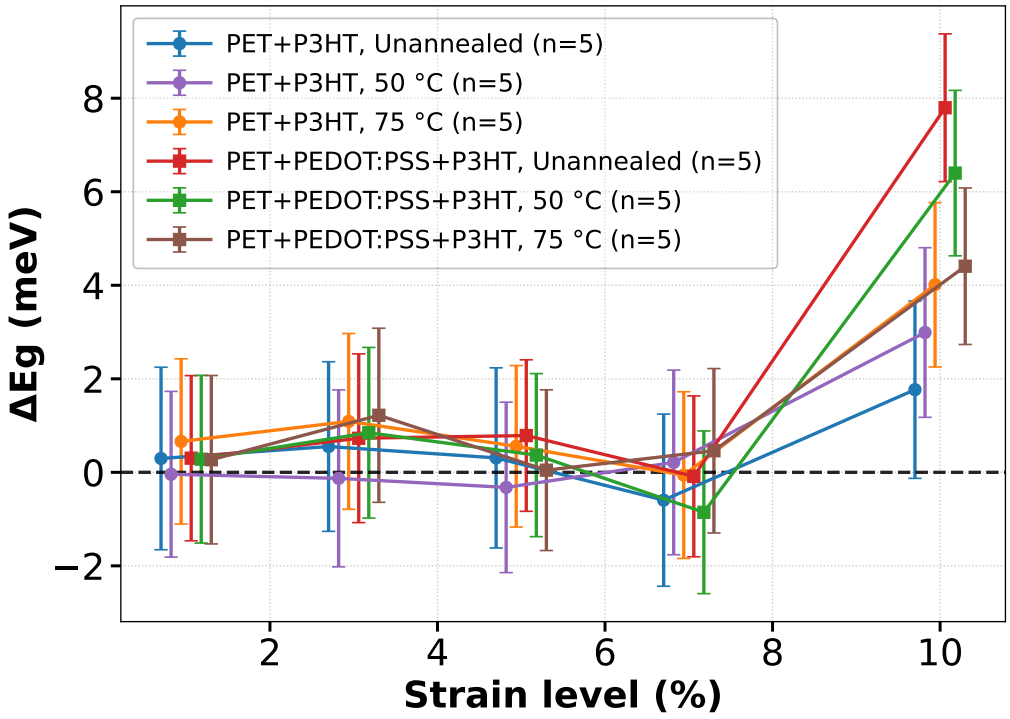

Fig. 7.4: Mean bandgap shift (ΔE_g) versus strain with 95% CIs across all stacks and annealing conditions.

residuals.

7.4.1 Statistical Evaluation of Strain Sensitivity

To quantify the pattern of the observed strain behaviour, we first fitted a pooled linear regression of ΔE_g versus strain using only the points at 1–7%. Here, "pooled" refers to combining all samples across annealing and stacking conditions into a single regression model, thereby yielding a global estimate of the slope while not explicitly modeling subgroup-specific effects. The estimated slope was -0.089 meV/% with a 90% CI of $[-0.173, -0.005]$ meV/%. We then applied a Two One-Sided Tests (equivalence testing) (TOST) for equivalence, using a pre-specified margin of ± 0.5 meV/%. This margin was chosen as a conservative tolerance for practically negligible trends in ΔE_g. The TOST yielded an extremely small p-value ($p < 10^{-14}$), providing strong evidence that the slope is statistically equivalent to zero. Thus, it can be concluded that the optical bandgap remains effectively invariant below 7% strain.

To verify the robustness of the 10% shift, we re-expressed strain as a categorical factor and fitted a regression with Heteroskedasticity-consistent standard errors (type

Table 7.2: Summary of statistical tests evaluating strain sensitivity of ΔE_g.

Contrast	Estimate	CI	Test	Conclusion
Small-strain regime (0–7%)				
Slope (0–7% strain)	−0.089 meV/%	90% CI [–0.173, –0.005]	TOST, margin ±0.5 meV/%	Statistically equivalent to zero; max shift ≤ 2 meV
Onset of permanent strain effects (7–10%)				
10% vs. pooled 1–7%	+4.27 meV	95% CI [2.38, 6.17]	Robust categorical regression (HC3)	Significant permanent strain effects emerge between 7–10%

HC3) (HC3) standard errors. This approach avoids relying on the usual regression assumption of normally distributed and homoscedastic errors, and it reduces the influence of unusual or outlying samples by widening their estimated uncertainty so they cannot dominate the overall result. The coefficient for the 10% condition was estimated at +4.27 meV (95% CI: +2.38 to +6.17 meV, $p = 9.4 \times 10^{-6}$). These values confirm the statistically decisive increase even under conservative assumptions. Table 7.2 summarizes these data.

Although each subgroup independently showed a positive 10% effect, to ensure that the pooled statistical contrast was not dominated by any single condition, we conducted leave-one-group-out sensitivity tests. Here, the overall 10% coefficient was re-estimated while systematically excluding one anneal/stack combination at a time. The resulting values ranged from 3.66 to 4.80 meV, and in all cases the 95% CIs remained strictly positive. This demonstrates that the bandgap widening at 10% strain is a universal feature across annealing and stacking variations, not a subgroup-specific anomaly.

To examine whether the magnitude of the 10% effect depends on preparation or stack layers, we restricted the dataset to the 10% condition and fitted a categorical regression with annealing temperature and stack type as predictors. The results showed neither annealing temperature nor stacking configuration contributed significantly to the variance in ΔE_g (all $p > 0.2$, HC3 regression). Nevertheless, inspection of the group means suggests that stacks containing a PEDOT:PSS interlayer exhibit a slightly larger shift compared to bare PET/P3HT. This trend is consistent with

more efficient and uniform strain transfer into the P3HT layer when the adhesive layer is present, which was indeed the intended purpose of introducing PEDOT:PSS. Finally, to test whether the 10% increase merely reflects a continuation of the linear slope observed below 7%, we fitted a pooled model of the form

$$\Delta E_g \sim \text{strain} + \text{is10},$$

where is10 is a binary indicator for the 10% condition. This formulation separates the effect into a baseline linear trend and any additional changes specific to 10%. The deviation coefficient was estimated at +4.81 meV (SE = 1.03, $p = 3.1 \times 10^{-6}$). This confirms that the 10% regime exhibits a distinct upward departure from the pooled linear trend.

Together, these results demonstrate that the optical bandgap of P3HT films remains stable up to 7% strain, but exhibits a robust and reproducible widening of approximately 4–5 meV at 10%. This effect is consistent across annealing and stacking variations and cannot be explained by extrapolation of the sub-threshold trend.

7.4.2 Physical Interpretation and Device-Level Implications

The negligible bandgap shifts observed up to 7% strain suggest that the optoelectronic properties of P3HT films remain stable because strain is dissipated through intrinsic microstructural relaxation processes rather than electronic perturbation. Poly(3-hexylthiophene) is known to form semicrystalline films comprising ordered lamellae interspersed within amorphous matrices [202, 204]. These crystalline domains, stabilized by π–π stacking and lamellar alignment, have been shown to provide mechanical reinforcement and preserve charge transport properties under moderate strain. Strain in such films is accommodated through chain slippage or relaxation at phase boundaries [126, 127, 205]. In addition, conformational reorganization within amorphous regions can occur, rather than direct deformation of the conjugated backbone. These mechanisms help maintain orbital overlap and prevent significant disruption of the electronic structure.

At higher strain levels (10%), the modest but statistically significant increase in optical bandgap ($\Delta E_g \approx 4.5$ meV) likely reflects a structural perturbation beyond the deformation tolerance of these buffering mechanisms. High-magnitude tensile strain can induce torsional disorder, chain misalignment, or disruption of favorable stacking orientations [127]. These structural changes reduce the effective conjugation length and lead to a blue-shift of the absorption onset. This interpretation aligns qualitatively with the ultrafast microscopy results from Kim *et al.* [30], who ob-

Table 7.3: Comparison of strain-induced energy level and band gap modulation in P3HT across different scales and measurement approaches.

Study	Method / Strain Regime	Scale (spatial / temporal)	Key Finding and Relevance
Menichetti et al. [29]	DFT simulation of the P3HT:PCBM interface under static, imposed strain	Molecular / equilibrium	Band offsets shift with strain (tens of meV), demonstrating intrinsic strain–electronic coupling at the molecular level.
Kim et al. [30]	SUEM under transient, photoinduced strain	Micrometer / picosecond–nanosecond	Local strain dynamically modulates the electronic structure, revealing instantaneous strain effects before any structural relaxation.
This study	UV–Vis Tauc analysis under macroscopic, residual tensile strain (ex-situ)	Thin-film / post-deformation	The band gap remains invariant up to 7% strain and increases only at 10% (about 4–5 meV), establishing a device-relevant strain threshold.

served that tensile perturbations suppress π-orbital overlap and transiently increase E_g on picosecond time scales. While their measurements capture local, rapidly applied strain, our ex-situ thin-film results represent the long-lived, residual outcome of deformation, revealing which microscopic effects persist once the film relaxes.
Importantly, the observed bandgap modulation is largely independent of annealing condition or stack architecture. This suggests that the strain response is governed primarily by the semicrystalline network itself rather than interfacial coupling or surface chemistry. Moreover, since strain was applied and held for 30 minutes before the secondary UV–Vis measurement, the reported spectral shifts show the residual strain effects, reflecting post-deformation structural relaxation.

Bridging Molecular Simulations and Thin-Film Realities. While molecular-scale studies have elucidated fundamental strain–electronic coupling mechanisms, their results do not necessarily extrapolate to thin-film systems under real-world conditions. For instance, Menichetti *et al.* [29] used DFT to show that strain can shift the donor and acceptor levels at the P3HT/PCBM interface, modulating energy offsets relevant for exciton dissociation. Similarly, Kim *et al.* [30] used scanning ultrafast electron microscopy to capture transient strain-induced modulation of E_g in P3HT with sub-nanosecond temporal resolution. Both studies provide invaluable mechanistic insights at the molecular or nanoscale level.
The results presented here contextualize prior molecular- and nanoscale predictions of strain–electronic coupling. This is reflected in the macroscopic optical response of device-relevant organic semiconductor thin-films. While earlier studies demonstrated that localized tensile deformation can perturb electronic structure under idealized or highly confined conditions [29, 30], our measurements show that such effects do not translate into a measurable bandgap response when strain is applied uniformly across a complete semicrystalline film. A concise comparison of these strain regimes, measurement approaches, and their corresponding band gap and en-

ergy level responses is provided in Table 7.3.
This behaviour is a direct consequence of the heterogeneous morphology of P3HT thin-films. Mechanical deformation is accommodated non-affinely through mesoscale relaxation pathways, including chain rearrangement in amorphous regions, reorganization of crystalline–amorphous boundaries, and intergrain accommodation, rather than through uniform stretching of the π-conjugated backbone [126]. These mechanisms dissipate applied stress while preserving intermolecular orbital overlap, effectively buffering the electronic structure against strain-induced perturbation.
As a result, the ensemble-averaged optical response remains stable even under residual tensile strains approaching 10%. This defines a deformation window within which P3HT thin-films can be regarded as electronically robust. This finding establishes a clear scale separation between microscopic strain sensitivity and macroscopic optical invariance. It also provides a physically grounded explanation for the apparent discrepancy between idealized predictions and device-relevant behaviour.
Direct morphological imaging by Atomic Force Microscopy (AFM) or Scanning Electron Microscopy (SEM) was not included, as ex-situ characterization of soft polymer films can be affected by strain relaxation during handling. The interpretation therefore draws on the well-established semicrystalline morphology of P3HT reported in the literature [126, 127, 204, 205]. Importantly, the conclusions are derived from ensemble-averaged optical trends that are insensitive to local nanoscale heterogeneity. Future work will extend this framework through in-situ strain-dependent structural characterization to further elucidate morphology–property relationships under load.

7.5 Conclusion

Our results demonstrate that P3HT-based thin films, both as single layers (PET/P3HT) and in PET/PEDOT:PSS/P3HT stacks, retain stable optical bandgaps under tensile strain up to 7%, with no statistically significant change. This invariance holds across annealing conditions, indicating that the semicrystalline morphology of P3HT allows internal relaxation of strain without perturbing the electronic structure.
However, spectra recorded after applying 10% strain for 30 minutes revealed a consistent increase in E_g of approximately $\sim$4–5 meV. This would suggest a threshold above which torsional disorder or disrupted π–π stacking begins to alter the electronic structure. These findings bridge molecular predictions with thin-film realities, showing that thin films do not exhibit continuous strain sensitivity as simulations

might suggest, but rather a plateaued response up to a critical strain level.
For device simulation including FEM of flexible optoelectronics, this behaviour allows simplification so that the optical bandgap can be treated as a constant parameter up to 7% strain. This enables more accurate and efficient models focused on mechanical propagation and charge transport, rather than strain-modulated absorption.
In general, our study provides a quantitative strain threshold for optical property stability in P3HT films, which supports their viability in long-term flexible device applications and informs design rules for strain-resilient organic photovoltaics.

Chapter 8

Temperature–Strain Interplay in P3HT: A Raman Spectroscopic Probe of Chain Alignment for Flexible Electronics

The contents of this chapter are adapted from a manuscript currently under preparation. The material is included here with the permission of all authors. The text has been edited to avoid repetition, particularly in the Introduction, State of the Art, and Methodology sections.

Temperature–Strain Interplay in P3HT: A Raman Spectroscopic Probe of Chain Alignment for Flexible Electronics; Ayush Kant Ranga, Mahya Ghorab, Veit Wagner, Mojtaba Joodaki, Arnulf Materny.

8.1 Abstract

Strain-induced chain alignment has long been proposed as an effective method to enhance charge transport in organic semiconductors. Among these materials, P3HT remains one of the most widely investigated conjugated polymers for applications ranging from flexible solar cells to field-effect transistors. However, when such materials are incorporated into flexible electronic architectures, mechanical deformation not only aligns polymer chains but can also introduce structural defects that deteriorate the performance of the device. Temperature is another equally critical parameter, as thermal annealing not only promote the long-range ordering in polymers but can also bring a certain level of rigidity to it. Despite the apparent relevance of

both mechanical and thermal cues, their combined effect has not yet been systematically studied. Here, we investigate how uniaxial tensile strain interacts with controlled processing temperature in rr-P3HT thin films deposited on PET substrates at 25°C(unannealed, i.e., room temperature drying), and annealed at 50 and 75 °C. These conditions represent manufacturing-relevant low-temperature processing conditions used in roll-to-roll fabrication of flexible organic electronics. We use Raman spectroscopy to monitor the vibrational fingerprint of rr-P3HT, focusing mainly on the ring-skeleton modes at approximately 1377 cm^{-1} (C–C) and 1445 cm^{-1} (C=C). These modes are sensitive to π-electron delocalization and thus report on the efficiency of charge-carrier transport. Later, we introduce a PEDOT:PSS interlayer between PET and P3HT to improve strain transfer between the underlying substrate and P3HT, which can enhance structural stability, thereby promoting more favourable chain alignment. Our results offer a coherent picture of how strain and temperature co-govern molecular ordering and highlight processing temperature as a key parameter that can either facilitate gentle alignment or lock the polymer into brittle, crack-prone microstructures.

8.2 Introduction

Conjugated-polymer semiconductors remain central to flexible electronics owing to their solution processability on lightweight plastic substrates [63, 206, 207]. They can tolerate mechanical deformation far better than inorganic semiconductors, enabling devices that can bend, stretch, and fold without significant loss of performance [128, 129, 207]. P3HT is among the most widely studied polymers and has become a benchmark system for exploring the interplay between structural order and charge transport for applications like solar cells and field-effect transistors [208, 209]. Recent studies have predicted that tensile deformation can orient the polymer backbone. This could potentially lead to strengthening the interchain interactions π-π and enhancing charge transport [56, 63, 128]. Optical measurements support this interpretation by revealing signatures of increased π-stacking and greater polaron delocalization under strain [208]. However, most of this evidence arises from simulations or experimental conditions that deviate substantially from those used in large-area, manufacturing-relevant processing [150].

Experimentally, a major gap in the literature arises from the fact that most strain-dependent studies probe as-cast films or layers deposited on prestretched substrates [210]. Although these configurations can reveal P3HT's intrinsic tendency to align under tension, they do not capture the role of the thermal history of devices [211].

Annealing promotes crystallization [212] and strengthens the interfacial adhesion [213], the increased crystallintiy have proven a direct impact on the stiffness of polymer blend films, which governs the crack-onset conditions in the polymer [177, 214]. Moreover, it modifies chain packing and increases film stiffness, shifting the response of stretching from smooth molecular alignment to the formation of microcracks [214, 215]. Consequently, the same nominal strain can result in entirely different molecular arrangements, depending on the thermal treatment. In other words, expected chain alignment upon stretching can also lead to tthe formation of microcracks.

Once microcracks form in these films, the mechanical environment becomes even more complex [151]. Crack formation redistributes local stress and reduces the actual strain experienced by the semicrystalline domains that carry excitons, polaron-pairs, delocalized excitons and polarons in such a system [151]. The other consequence of the formation of microcracks is slippage of metal contacts in the actual device and strain-induced defect formation in the substrate holding the semiconducting film [95]. The behavior of the supporting substrate adds another layer of complexity. PET, which is widely used in flexible electronics, is not mechanically inert. Spectroscopic studies show that PET exhibits irreversible band shifts and linewidth changes once tensile deformation exceeds only a few percent [31]. Such substrate evolution alters frictional coupling and modulates strain transmission to the polymer semiconductor. In optoelectronic devices, the substrate, interfacial layers, and active layer form an integrated mechanical system, such that strain imposed on one component is transferred throughout the stack.

Raman spectroscopy offers a sensitive probe of how mechanical deformation alters the molecular order that governs charge transport in P3HT. Two vibrational modes are especially informative: the intra-ring C–C stretch near 1377 cm^{-1} and the symmetric C=C stretch near 1445 cm^{-1} [149]. The 1377 cm^{-1} mode is a signature of backbone planarity and torsional changes in the polymer chain, and the 1445 cm^{-1} mode is sensitive to changes in conjugation length of polymer and chain conformations [216]. Together, they provide a direct view of how the polymer structure reorganizes in response to applied strain. We quantified structural changes by fitting the Raman spectra and analyzing the changes in band position and full width at FWHM of the key bands. Earlier studies show that the 1377 cm^{-1} mode is insensitive to changes induced by better alignment in thin-films, for example, via thermal treatment and heterojunction formation with acceptor-type fullerene molecules. In contrast, the 1445 cm^{-1} mode can shift to lower wavenumbers as temperature-induced ordering in polymer chains increases [93].

In this study, P3HT films were spin-coated onto PET substrates and subsequently annealed at 25°C, i.e., kept at room temperature, 50°C, or 75°C before being stretched incrementally up to 10%. The non-annealed films exhibit a predominantly elastic response, reflected in a narrowing of the FWHM and only minor shifts in the Raman band position. In contrast, the annealed films show a markedly different behaviour: increasing the processing temperature appears to rigidify the microstructure, effectively constraining chain mobility. This stiffening becomes most pronounced at 75°C, where the strain-induced broadening of the FWHM points to the development of microstructural defects under deformation. Introducing an intermediate PEDOT:PSS layer further modifies this response, enabling more efficient strain transfer and improved mechanical stability during stretching.

8.3 Results and Discussion

To understand the evolution of the FWHM of the 1377 cm^{-1} and 1445 cm^{-1} Raman bands responding to strain, we have plotted a time series of this evolution. T_0 represents the time when there is no delay between the applied strain and the spectral measurements. The *Rest* state represents the spectra measured after the strain was released. The total time before releasing the strain was 30 minutes. This method can therefore provide both transient and residual information about the response of these films. All plotted values represent the difference between the stretched and unstretched values of FWHM and band position of the same state. A Raman spectrum of a 75 °C annealed P3HT film is shown in Fig. 8.1. All spectra were measured at three different points for statistical purposes. All spectra were recorded for 10 seconds and averaged over four iterations. The laser power was optimized to 3 mW to eliminate any heat or bleaching-related effects on the sample. From the Raman spectra, we identified the dominant vibrational modes characteristic of P3HT, which are summarized in Tab. 8.1. Additional bands originate from the underlying PET substrate; the strain response of these PET modes has been analyzed in detail in our previous work [31]. In the present study, we concentrate exclusively on the evolution of the two most structurally informative P3HT modes: the C–C stretch at 1377 cm^{-1} , and the C=C stretch at 1445 cm^{-1}. These bands provide the clearest insight into strain and temperature-induced changes in conjugation and backbone ordering.

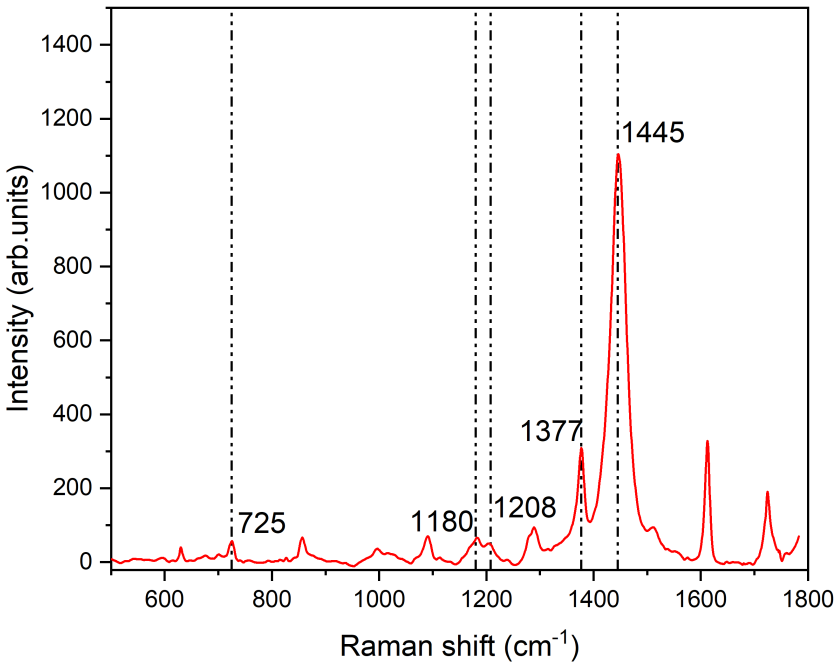

Fig. 8.1: Raman spectrum of an unstretched P3HT-only film annealed at 75°C.

8.3.1 Raman Response of the 1377 cm^{-1} Band Under Strain and Annealing

The Raman band at ∼1377 cm^{-1} in rr-P3HT is commonly assigned to an in-plane C-C skeletal stretching mode of the thiophene backbone, with a non-negligible contribution from motions involving the hexyl side chains [217, 218]. Fanchini and co-workers demonstrated that the corresponding feature near 1380 cm^{-1} is sensitive to nanoscale ordering and phase separation, with changes in intensity and linewidth reflecting variations in local structural order [217]. More recently, Mosca *et al.* showed that the pair of backbone modes near 1377 and 1440 cm^{-1} act as sensitive fingerprints of π-electron delocalization, where increased effective conjugation length and backbone planarity lead to a redshift and spectral narrowing, while localization or enhanced torsional disorder produces blueshifts and linewidth broadening [148]. At the same time, IR and Raman studies of P3HT degradation and composite formation indicate that vibrations in the 1377-1381 cm^{-1} region also carry significant CH_3 deformation character associated with side chains and defect-rich segments [218]. Taken together, these observations imply that the 1377 cm^{-1} band reports simultaneously on backbone conjugation and planarity, as well as on the conformational state of side chains and defect environments. Consequently, analysis

Table 8.1: Characteristic Raman bands of P3HT and their assigned vibrational modes.

S.No	Raman shift (cm^{-1})	Assigned vibration
1	725	C–S–C deformation
2	1180	C–H bending mode
3	1208	Inter-ring C–C stretching
4	1377	Intra-ring C–C stretching
5	1445	Symmetric C=C stretching

of both the band position and FWHM under mechanical strain provides a sensitive probe of how tensile load redistributes microscopic environments within the P3HT layer. In the following section, the strain response of the 1377 cm^{-1} band is analyzed for PET/P3HT and PET/PEDOT:PSS/P3HT stacks. For each stack, wavenumber shifts ($\Delta\tilde{\nu}$) and FWHM changes(ΔFWHM) are evaluated relative to the corresponding unstretched reference spectrum, with negative or positive $\Delta\tilde{\nu}$ indicating red or blueshift and negative or positive ΔFWHM indicating spectral narrowing or broadening, respectively. Both the instantaneous response at T_0 and the post-unloading *Rest* state are considered to distinguish recoverable from retained strain-induced modifications.

In Fig. 8.2, we show the evolution of the 1377 cm^{-1} Raman band as a function of increasing strain under different annealing conditions at the instantaneous T_0 state. Panel (a) presents the strain-induced shift in the apparent Raman band position, while panel (b) displays the corresponding variation in FWHM relative to the unstretched film. The post-unloading response is shown separately in Fig. 8.3. Panel (a) illustrates the residual band-position shifts measured in the *Rest* state, whereas panel (b) reports the corresponding changes in FWHM.

Unannealed P3HT on PET. For unannealed PET/P3HT films, the 1377 cm^{-1} mode shows a very small wavenumber shift that is close to the detection limit under strain, but a consistent narrowing of the FWHM. This indicates that stretching does not significantly change the average backbone vibrational energy, but instead selectively highlights the subset of chains that are better aligned and more effectively coupled to the substrate. The intrinsically soft, heterogeneous morphology of unannealed P3HT allows tensile load to be accommodated mainly through reversible chain alignment and slight planarization, producing a narrower FWHM without major wavenumber shifts. After unloading (at *Rest*), very small residual changes in both peak position and linewidth persist, reflecting minor, irreversible microstructural adjustments accumulated during the 30-minute strain application.

Overall, the unannealed films behave predominantly elastically with strain revealing a mechanically selected, better-aligned chain population and only subtle structural memory after unloading [148, 217, 218].

PET/P3HT annealed at 50°C. After mild thermal annealing at 50°C, the PET/P3HT films show a markedly different response from the unannealed samples. The 1377 cm^{-1} band again exhibits only minimal, near-threshold wavenumber shifts, but its FWHM broadens at all strain levels, both at T_0 and *Rest*. This broadening reflects the more segmented, semi-crystalline microstructure produced by mild annealing, in which strain is distributed unevenly among crystalline lamellae, tie chains, and the constrained amorphous phase. As a result, tensile deformation produces a wider spread of local vibrational environments without significantly altering the average backbone planarity. The incomplete recovery of the ΔFWHM in the *Rest* state indicates that some microstructural heterogeneity, likely small interfacial distortions or microcracks, persist after the 30-minute loading period. Overall, the 50°C films deform, resulting in heterogeneous FWHM in contrast to the clean chain-alignment behavior observed in the unannealed case, which is consistent with a stiffer morphology prone to cracks upon stretching [214, 217, 219].

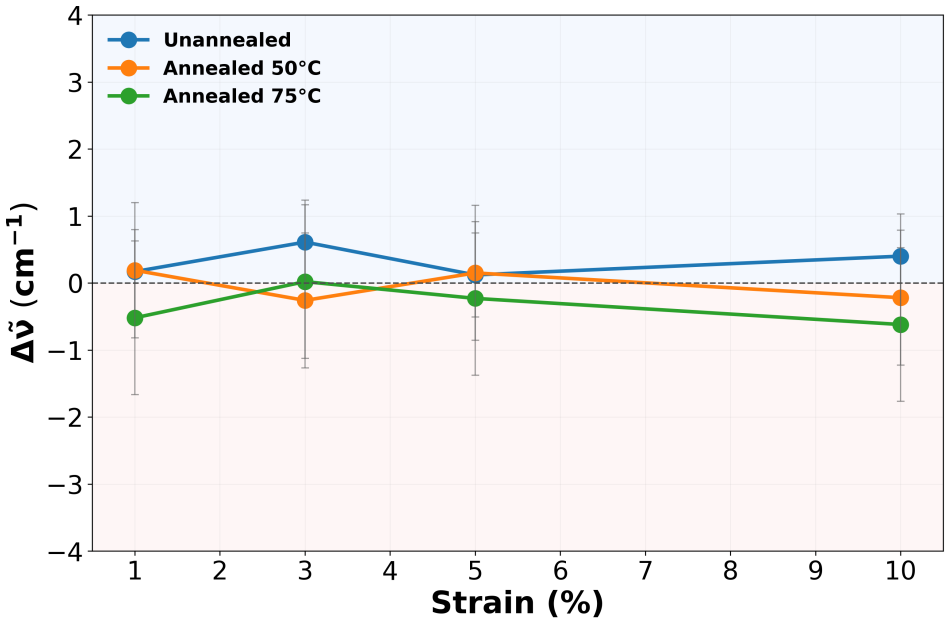

(a)

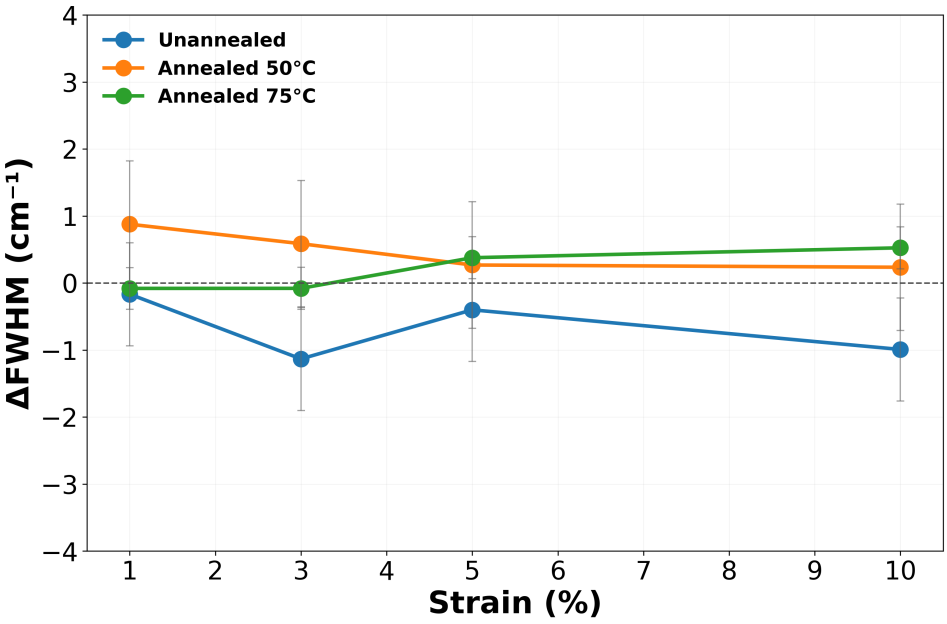

(b)

Fig. 8.2: Strain dependence of the 1377 cm^{-1} Raman band in PET/P3HT under different annealing conditions at T_0. (a) Band-position shift at the instantaneous T_0 state. (b) Corresponding FWHM variation at T_0. Curves correspond to unannealed, 50°C-annealed, and 75°C-annealed films.

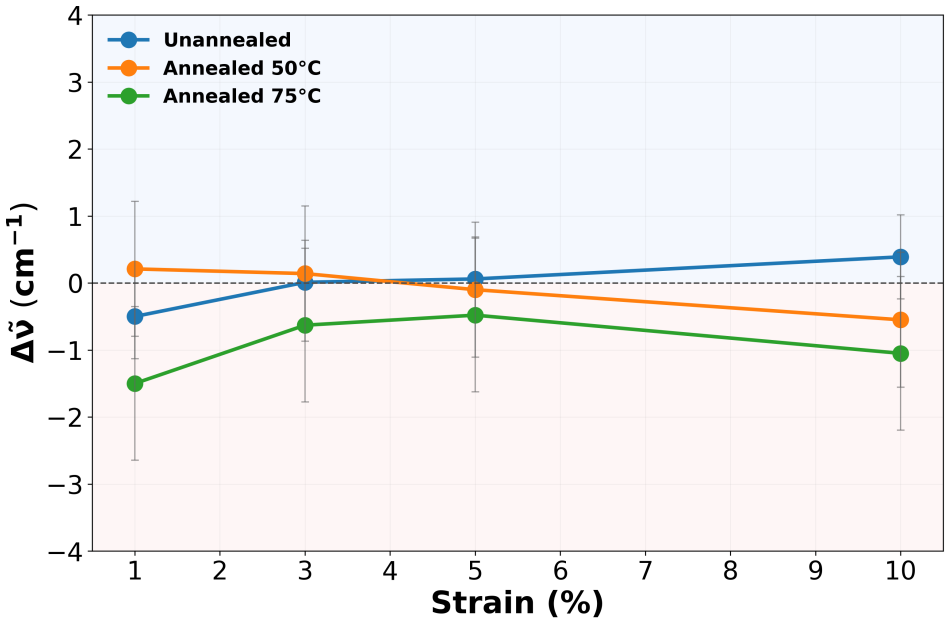

(a)

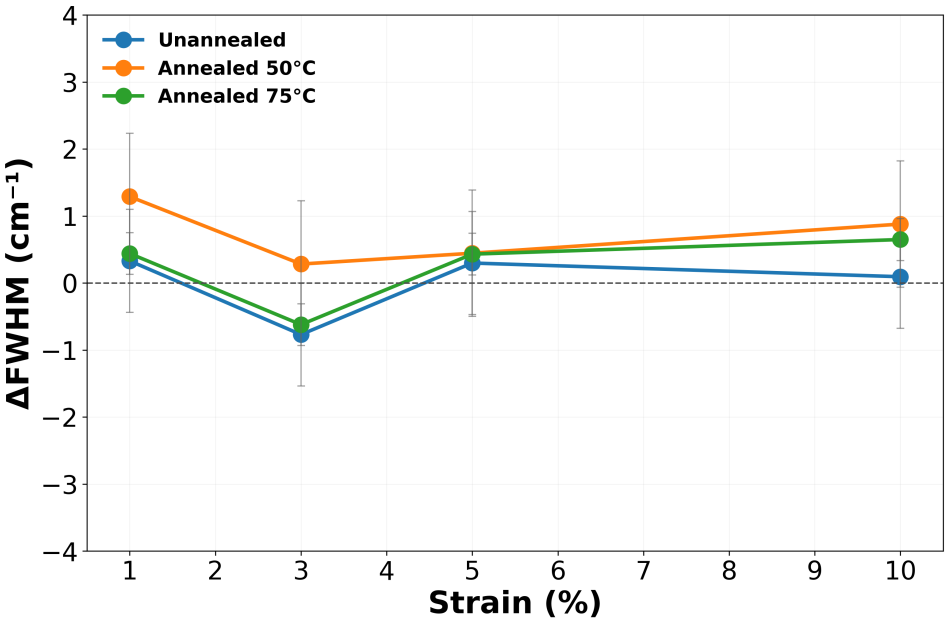

(b)

Fig. 8.3: Strain dependence of the 1377 cm^{-1} Raman band in PET/P3HT under different annealing conditions at *Rest*. (a) Band-position shift in the post-unloading *Rest* state. (b) Corresponding FWHM variation in the *Rest* state. Curves correspond to unannealed, 50°C-annealed, and 75°C-annealed films.

PET/P3HT annealed at 75°C. At 75°C annealing, where P3HT develops even higher ordered lamellar structure compared to other temperatures [220], the strain response of the 1377 cm^{-1} band becomes more brittle than in the 50°C films. For

small applied strain, the changes in FWHM are negligible, but as the applied strain approaches the 5% mark, the FWHM broadens even more than that of 50°C annealed film. Across all strain levels, the peak position at T_0 exhibits a small redshift that persists after unloading, indicating that deformation in these crystalline domains involves irreversible changes in the vibrational environment [215]. The accompanying linewidth evolution remains modest-narrowing at low strain and broadening at higher strain, consistent with an initial regime of coherent chain alignment followed by the emergence of heterogeneous microstructural distortions as applied strain increases. Overall, at 5% and above level of applied strain, the 75°C films exhibit a deformation pathway characteristic of a stiff, highly ordered morphology, in which load-bearing backbones are unable to relax elastically and instead develop irreversible strain-induced defects. More importantly, the observation at 75°C is more important compared to other annealing values, as it is representative of typical annealing temperatures involved in real device architecture, thus the observation here establish a safe deformation limit at around 5%.

8.3.2 Impact of PEDOT:PSS

Introducing a PEDOT:PSS interlayer between PET and P3HT modifies not only the mechanical stability but also the local electrostatic and chemical environment of the P3HT chains. PEDOT:PSS is much softer than PET and can both mediate and partially redistribute strain, while also improving adhesion and suppressing interfacial slippage between PET and P3HT [219, 221]. More importantly, the Raman band near 1377 cm^{-1} contains an overlapping contribution from the P3HT backbone and the poly(3,4-ethylenedioxythiophene) (PEDOT) layer in the trilayer P3HT/PEDOT:PSS/PET configuration [222]. Consequently, this feature is most appropriately interpreted as a stack-level spectral marker rather than a mode uniquely associated with a single polymer component. Strain-induced variations in the band position and FWHM therefore, reflect the collective vibrational response of the multilayer system. The objective of this study was to assess how the presence of an adhesion interlayer (PEDOT:PSS), which is commonly used as a hole transport layer in organic photovoltaic architectures, influences the strain evolution of the Raman response [15, 223]. Because all strain-dependent changes are evaluated relative to the unstretched reference state of each stack, the PEDOT contribution does not alter the observed "trends" with respect to applied strain, but instead results in a systematic offset of the absolute spectral parameters. The measured changes may thus arise from the intrinsic strain sensitivity of the constituent layers, the superposition of overlapping vibrational modes, and mechanical coupling at the interfaces,

all of which are relevant to realistic device configurations.
Figure 8.4 presents the strain-dependent evolution of the 1377 cm^{-1} Raman band in the PET/PEDOT:PSS/P3HT stack at the instantaneous T_0 state. Panel (a) shows the apparent band-position shift as a function of applied strain for different annealing conditions, while panel (b) reports the corresponding variation in FWHM relative to the unstretched film. The post-unloading response is displayed separately in Figure 8.5. Panel (a) illustrates the residual band-position shifts measured in the *Rest* state, whereas panel (b) presents the associated changes in FWHM. The comparison between T_0 and *Rest* enables direct assessment of reversible versus irreversible strain-induced structural modifications in the presence of the PEDOT:PSS interlayer.

Unannealed P3HT with PEDOT:PSS. In unannealed PET/PEDOT:PSS/P3HT stacks, introduction of PEDOT:PSS interlayer alters the early-stage response at 1% strain. The 1377 cm^{-1} band narrows strongly, indicating that PEDOT:PSS improves mechanical coupling and selectively engages a well-aligned subset of chains more effectively than in the PET/P3HT bilayer. At intermediate strain levels (3-5%), the band broadens and shifts slightly to lower frequency, reflecting a temporary increase in microstructural heterogeneity. At even higher strain (7-10%), the narrowing of FWHM suggests that the mechanically dominant chains regain control of the spectral response rather than giving way to irreversible damage. After unloading, only minor residual narrowing and small shifts remain, showing that the tri-layer accommodates strain largely elastically while retaining a weak memory of chain selection.

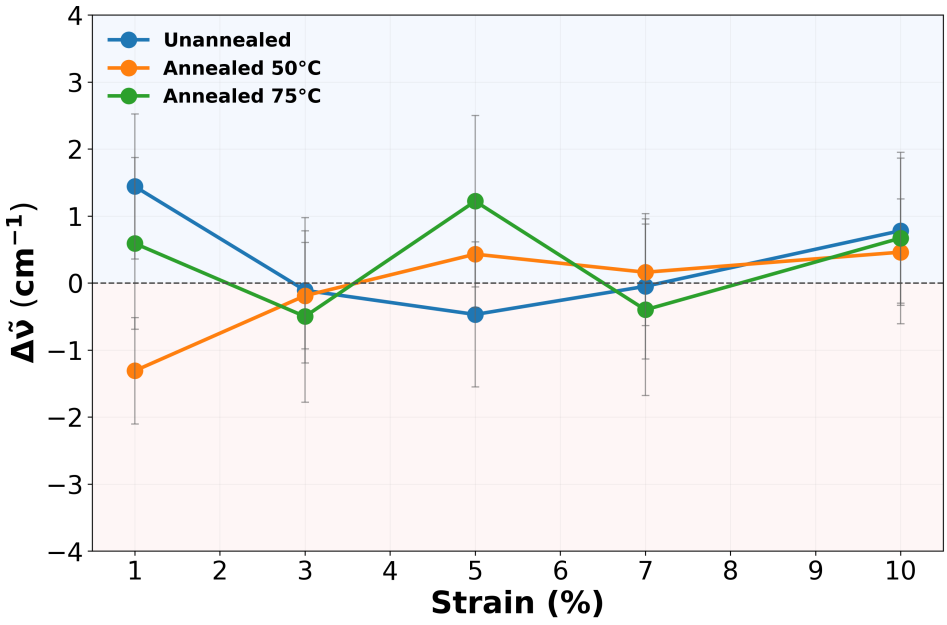

(a)

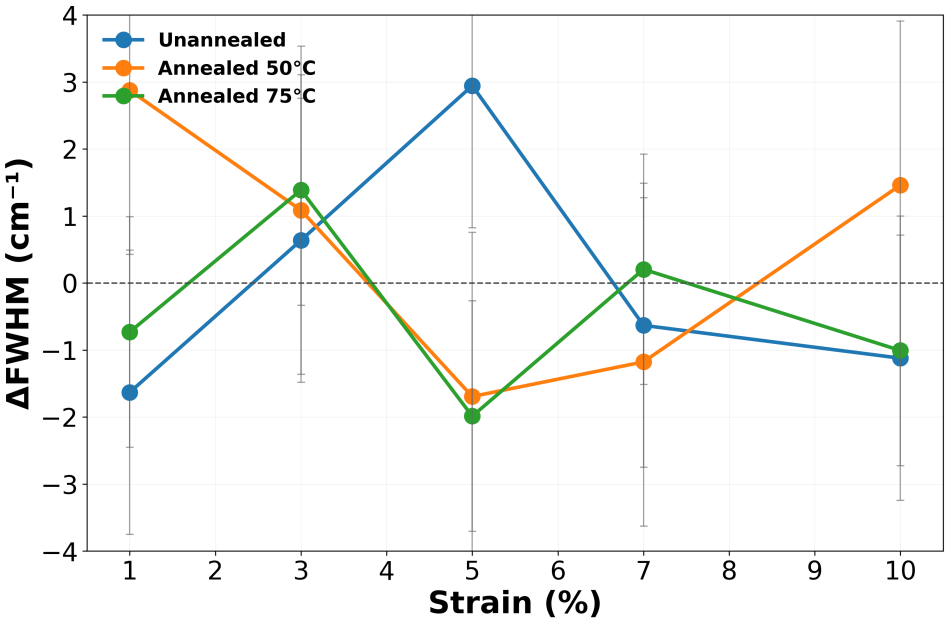

(b)

Fig. 8.4: Strain dependence of the 1377 cm^{-1} Raman band in PET/PEDOT :PSS/P3HT under different annealing conditions at T_0. (a) Band-position shift at the instantaneous T_0 state. (b) Corresponding FWHM variation at T_0. Curves correspond to unannealed, 50°C-annealed, and 75°C-annealed films.

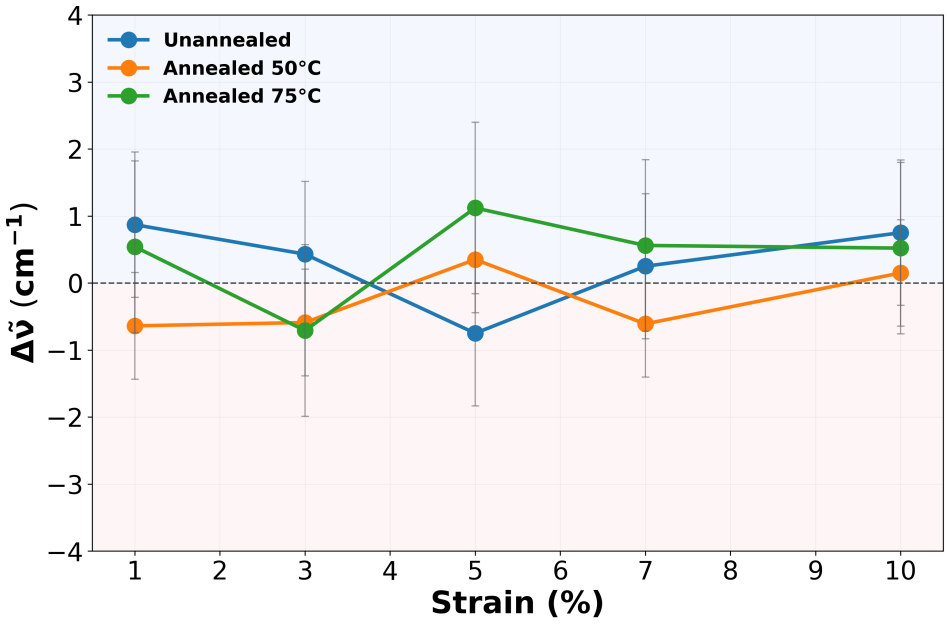

(a)

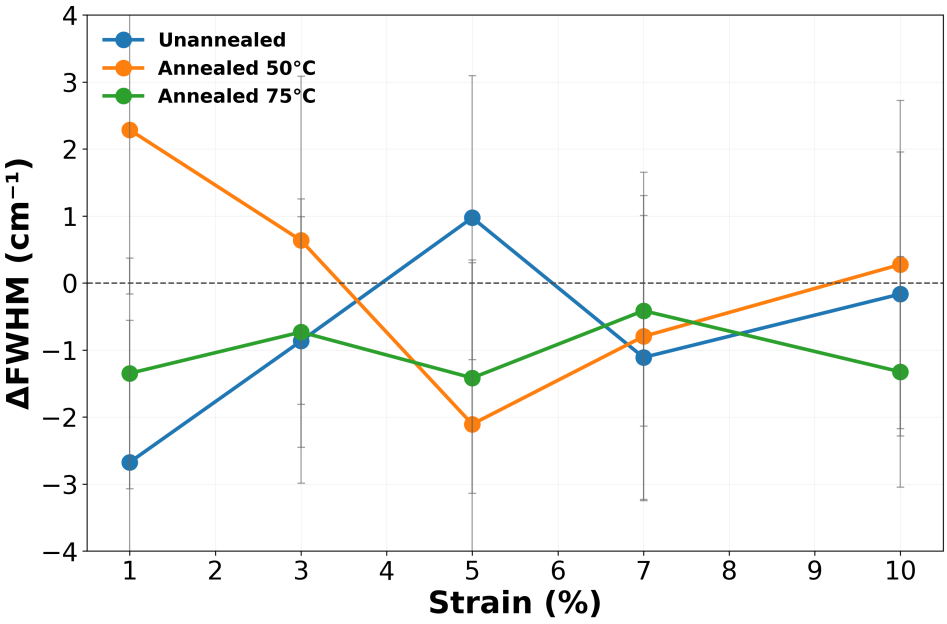

(b)

Fig. 8.5: Strain dependence of the 1377 cm^{-1} Raman band in PET/PEDOT :PSS/P3HT under different annealing conditions at *Rest*. (a) Band-position shift in the post-unloading *Rest* state. (b) Corresponding FWHM variation in the *Rest* state. Curves correspond to unannealed, 50°C-annealed, and 75°C-annealed films.

Annealed P3HT with PEDOT:PSS (50°C). In the annealed PET/ PEDOT:PSS/P3HT stacks, the strain-induced shifts of the 1377 cm^{-1} band remain small at all strain levels and are consistently weaker than in the corresponding PET/P3HT bilayers, re-

flecting the ability of PEDOT:PSS to redistribute the applied load. At 50°C, where P3HT is only moderately ordered, the response consists of dominant broadening initially but with additional strain, the FWHM becomes systematically narrower. The overall observed trend at 50°C is narrowing compared to 1%.

Annealed P3HT with PEDOT:PSS (75°C). Analyzing the stack, which is more relevant to a real organic semiconductor-based device, highly ordered 75°C films with PEDOT:PSS exert an even stronger stabilizing influence. The irreversible redshifts characteristic of the PET/P3HT bilayer are largely suppressed, and the FWHM remains only mildly affected, indicating that the interlayer prevents catastrophic lamellar distortion or defect accumulation at the interface. At the *Rest* state, the overall line width shows consistent narrowing as compared to all the stacks, which is due to increased homogeneity in Raman scattering arising from well-aligned subsets of polymer chains. Taken together, these results show that PEDOT:PSS functions as an effective mechanical buffer across the considered annealing conditions, smoothing strain gradients and preserving the structural integrity of P3HT. This is consistent with earlier investigations reporting stabilization due to the additional layer, with the most pronounced protective effect observed in the most crystalline films [95, 148].

8.3.3 Raman Response of the 1445 cm^{-1} Band Under Strain and Annealing

The Raman band near 1445 cm^{-1} corresponds to the symmetric C=C stretching vibration of the P3HT backbone and is a highly sensitive spectroscopic probe of conjugation length, backbone torsion, and π–π stacking in conjugated polymers. Within this framework, wavenumber shifts $\Delta\tilde{\nu}$ of the 1445 cm^{-1} band primarily indicate changes in effective conjugation length and backbone planarity. Positive shifts (blueshifts) are associated with increased torsional disorder and reduced conjugation, whereas negative shifts (redshifts) may arise from backbone planarization, extended conjugation, or defect-induced softening of local force constants. Changes in FWHM reflect the distribution of local structural environments: narrowing corresponds to a more uniform subset of vibrational microenvironments, while broadening signifies heterogeneous strain fields, distributed disorder. These correlations are well established for P3HT and related conjugated polymers [93]. The analysis below follows the strain response framework established for the 1377 cm^{-1} band. The 1445 cm^{-1} results are therefore not used to redefine deformation regimes, but rather to refine and contrast how strain accommodation differs between PET/P3HT

and PET/PEDOT:PSS/P3HT stacks.

Figure 8.6 shows the strain-dependent evolution of the 1445 cm^{-1} Raman band in PET/P3HT at the instantaneous T_0 state. Panel (a) presents the apparent band-position shift as a function of applied strain under different annealing conditions, while panel (b) displays the corresponding variation in FWHM relative to the unstretched film. The post-unloading response is presented separately in Figure 8.7. Panel (a) illustrates the residual band-position shifts measured in the *Rest* state, whereas panel (b) reports the associated changes in FWHM. Because the 1445 cm^{-1} mode is particularly sensitive to conjugation length and π-electron delocalization, its strain dependence provides direct insight into how mechanical deformation and thermal history jointly influence electronic structure in P3HT.

Unannealed P3HT on PET. In unannealed PET/P3HT, stretching consistently produces a small blueshift, indicating that the dominant microscopic effect is increased torsional disorder and a shortening of conjugation segments along the P3HT chains. Notably, similar to the 1377 cm^{-1} band, the corresponding linewidth of 1445 cm^{-1} narrows at low and intermediate strains, showing that although the film becomes more disordered on average, the vibrational response is increasingly dominated by a subset of semi-ordered domains that efficiently transmit mechanical stress. This effect is characteristic of strain-assisted alignment in flexible photovoltaics and establishes safe deformation limits for P3HT of extended chain segments while the more amorphous portions remain mechanically inactive [224, 225]. Only at the highest strains (10%) does the linewidth broaden, signaling the onset of heterogeneous deformation. After strain release at *Rest*, the wavenumber is nearly fully recovered and the FWHM becomes narrower, reflecting the elasticity of these soft unannealed films [95].

PET/P3HT annealed at 50°C. The 50°C-annealed PET/P3HT films exhibit a more intricate balance between disordering and domain-specific deformation. Although the wavenumber response under load remains dominated by small blueshifts-indicating that the backbone continues to lose conjugation with tensile strain, the linewidth alternates between narrowing and broadening depending on the strain level. This behavior is typical of moderately semicrystalline P3HT, in which lamellar crystallites and amorphous regions share mechanical load in a nonuniform fashion. At some strains, only specific lamellar stacks or extended chain segments bear deformation, narrowing the linewidth; at others, a wider distribution of torsional configurations is activated, broadening the peak. The persistence of slight blueshifts

after unloading at low-medium strains shows that a portion of the induced disorder is plastically retained, consistent with modest conformational rearrangements within semi-ordered domains.

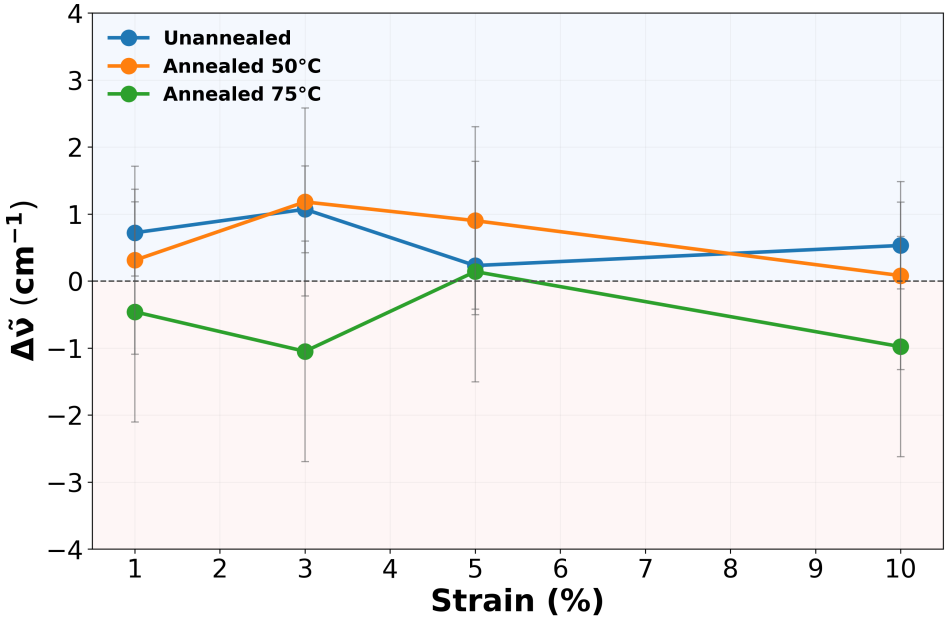

(a)

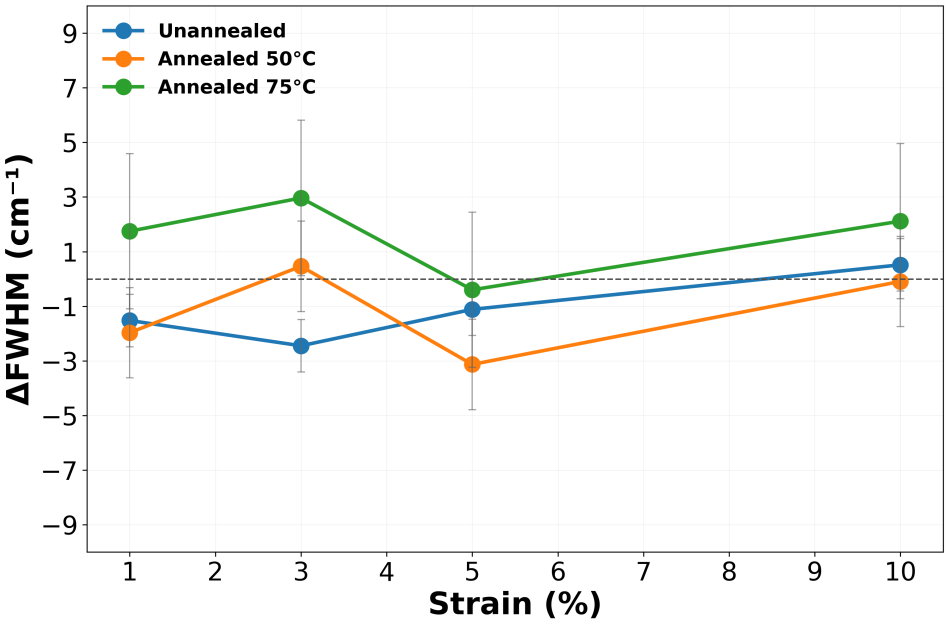

(b)

Fig. 8.6: Strain dependence of the 1445 cm^{-1} Raman band in PET/P3HT under different annealing conditions at T_0. (a) Band-position shift at the instantaneous T_0 state. (b) Corresponding FWHM variation at T_0. Curves correspond to unannealed, 50°C-annealed, and 75°C-annealed films.

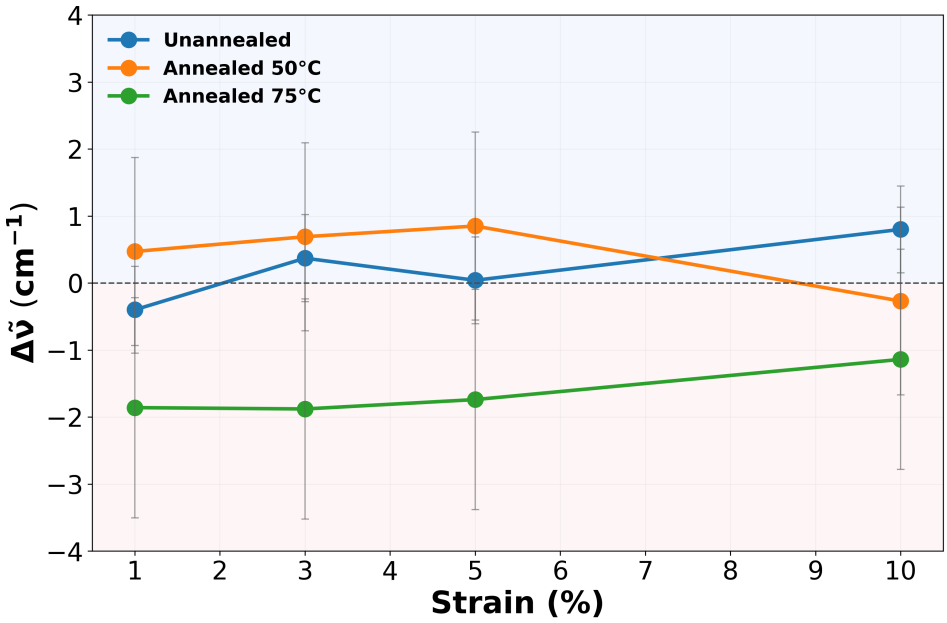

(a)

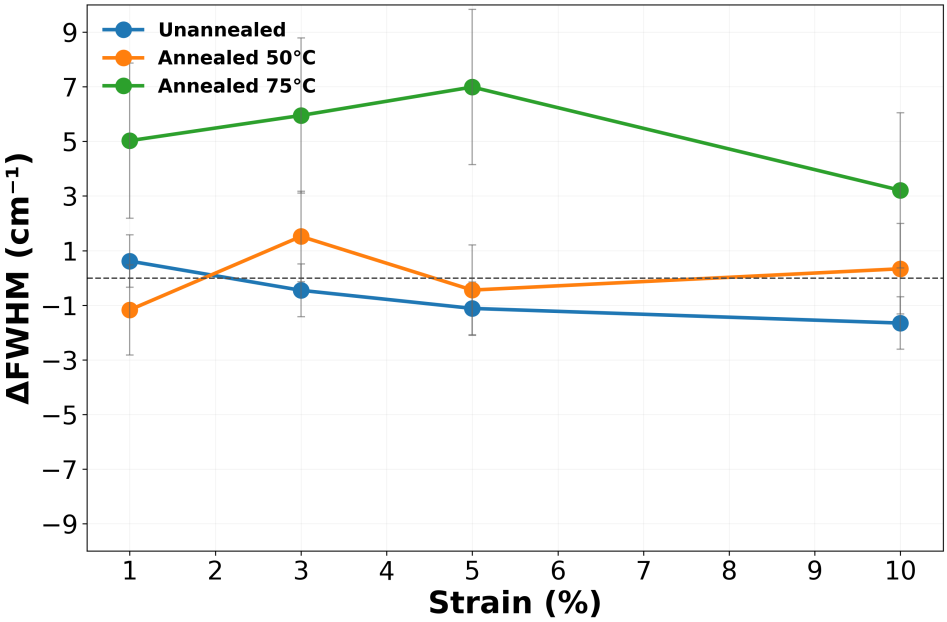

(b)

Fig. 8.7: Strain dependence of the 1445 cm^{-1} Raman band in PET/P3HT under different annealing conditions at *Rest*. (a) Band-position shift in the post-unloading *Rest* state. (b) Corresponding FWHM variation in the *Rest* state. Curves correspond to unannealed, 50°C-annealed, and 75°C-annealed films.

PET/P3HT annealed at 75°C. A qualitatively different response was observed in the 75°C-annealed PET/P3HT films, where P3HT is substantially more crystalline and mechanically stiff [95]. Here, strain produces redshifts both during load-

ing and after relaxation, accompanied by dramatic linewidth broadening (up to approximately 6-7 cm^{-1} at *Rest*). This combination is the spectroscopic hallmark of defect-dominated deformation rather than planarization. Highly ordered P3HT lamellae are brittle and prone to early crack onset, interlamellar slip, and strain localization [152, 221]. When such damage accumulates, bond-softening mechanisms and local mechanical decoupling lower the vibrational wavenumber (redshift), while the coexistence of intact, rotated, damaged, and fragmented chain segments produces a highly heterogeneous vibrational environment, manifested as substantial broadening. The irreversible nature of these shifts after unloading indicates that the microstructure of highly annealed (75°C) P3HT undergoes permanent, damage-mediated reorganization rather than reversible backbone deformation.
Figure 8.8 presents the strain-dependent evolution of the 1445 cm^{-1} Raman band in the PET/PEDOT:PSS/P3HT stack at the instantaneous T_0 state. Panel (a) shows the apparent band-position shift as a function of applied strain for different annealing conditions, while panel (b) reports the corresponding variation in FWHM relative to the unstretched film. The post-unloading response is shown separately in Figure 8.9. Panel (a) illustrates the residual band-position shifts measured in the *Rest* state, whereas panel (b) presents the associated changes in FWHM. As the 1445 cm^{-1} mode is particularly sensitive to conjugation length and π-electron delocalization, its strain dependence provides direct insight into how mechanical deformation is transmitted through the PEDOT:PSS interlayer and how thermal history modulates the electronic response of P3HT.

8.3.4 Introduction of PEDOT:PSS

Unannealed P3HT with PEDOT:PSS Introducing a PEDOT:PSS interlayer alters these behaviors across all annealing conditions. In unannealed PET/ PEDOT:PSS/P3HT, strain induces very minute blue and red shifts, and the linewidth fluctuations, though present, are consistently smaller and more controlled than in the corresponding bare PET/P3HT films. More importantly, apart from 1% strain, the changes in FWHM are also close to the detection limit, which shows that the overall impact of PEDOT:PSS manifests itself as a more stable Raman response.

Annealed P3HT with PEDOT:PSS (50°C). In the 50°C-annealed trilayers, the spectral evolution becomes more balanced: blueshifted and redshifted components coexist, linewidth changes alternate in sign, and the film evolves into a more stable load-bearing configuration at higher strains. Crucially, linewidth broadening is always far less extreme than in the bare PET/P3HT analog.

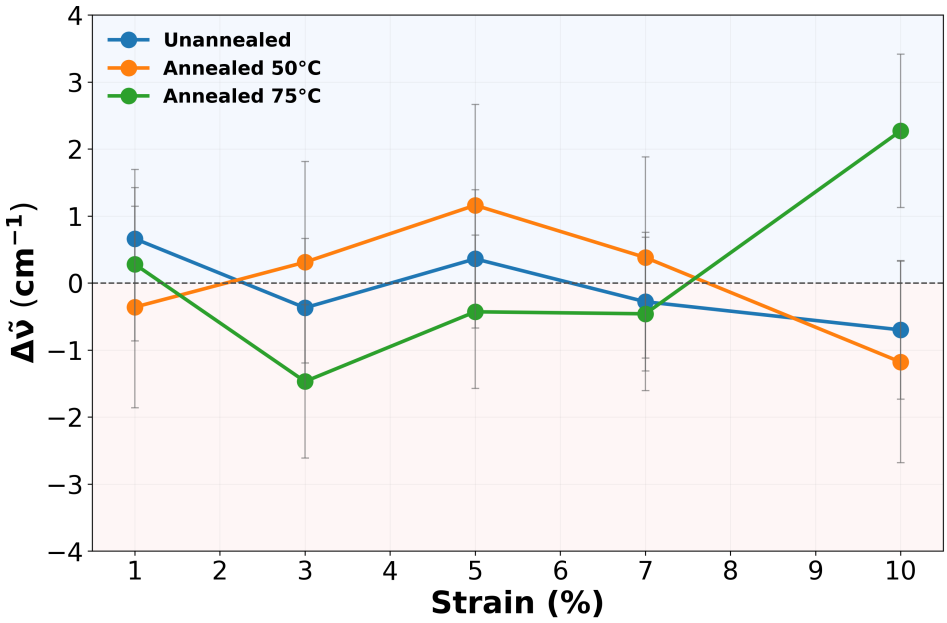

(a)

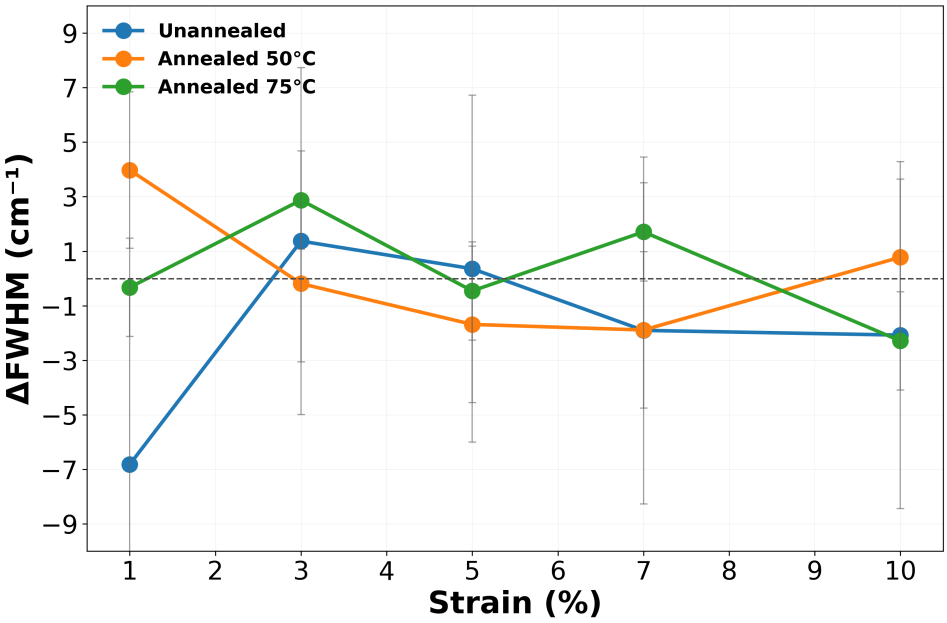

(b)

Fig. 8.8: Strain dependence of the 1445 cm^{-1} Raman band in PET/PEDOT :PSS/P3HT under different annealing conditions at T_0. (a) Band-position shift at the instantaneous T_0 state. (b) Corresponding FWHM variation at T_0. Curves correspond to unannealed, 50°C-annealed, and 75°C-annealed films.

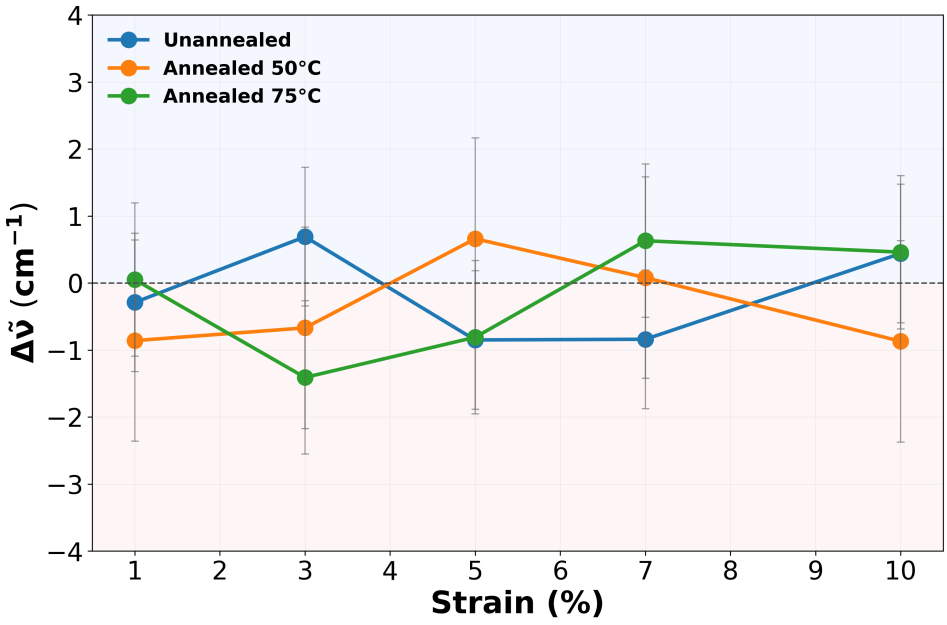

(a)

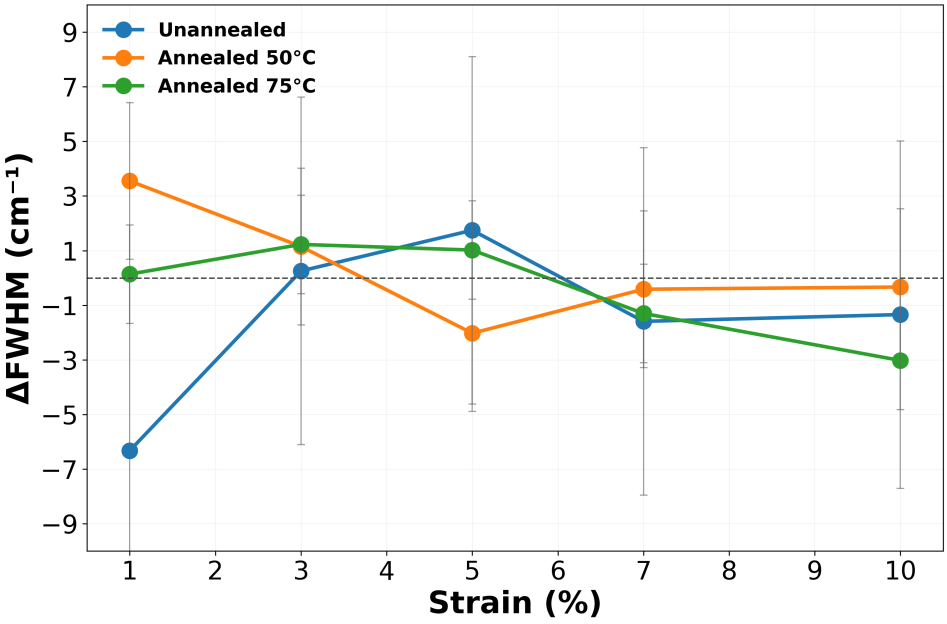

(b)

Fig. 8.9: Strain dependence of the 1445 cm^{-1} Raman band in PET/PEDOT :PSS/P3HT under different annealing conditions at *Rest*. (a) Band-position shift in the post-unloading *Rest* state. (b) Corresponding FWHM variation in the *Rest* state. Curves correspond to unannealed, 50°C-annealed, and 75°C-annealed films.

Annealed P3HT with PEDOT:PSS at 75°C The most important and device-relevant stack shows the trends which are well in line with our argument of role of PEDOT:PSS as stabilizing layer. At 75°C-annealed PET/PEDOT:PSS/P3HT stacks,

the presence of PEDOT:PSS suppresses the severe broadening and uniformly red-shifted behavior observed in the brittle, highly crystalline P3HT films on bare PET. While some mid-strain broadening persists, reflecting partial lamellar rearrangement or defect formation, the overall vibrational signature lacks the catastrophic disordering seen in the absence of the interlayer. This demonstrates that PEDOT:PSS not only improves interfacial adhesion but also dissipates strain energy, allowing brittle P3HT domains to reorganize without undergoing widespread fracture.

8.4 Conclusion and Outlook

We have investigated how mechanical strain and thermal processing jointly govern the response of rr-P3HT thin films integrated on flexible PET substrates using Raman spectroscopy. By systematically tracking band-position shifts and FWHM under controlled stretching, we focused on the two dominant Raman-active modes at 1377 and 1445 cm^{-1}. The combined evolution of band position and linewidth is required to disentangle changes in average backbone configuration from variations in local microstructural heterogeneity. Thermal history emerges as a decisive parameter as the unannealed films deform primarily through reversible conformational adjustment whereas increasing annealing temperature progressively constrains structural mobility, promoting retention of strain-induced configurations and the onset of irreversible damage. In other words, the increased stiffness in annealed films have moved the focus of strain assisited chain alignment to microcracks or damage assisted heterogeneity. Finally, it is important to note a methodological and physical limitation inherent to the present analysis. Although a systematic and controlled experimental approach was employed to ensure that the Raman response provides direct insight into the underlying microscopic processes, the mechanical deformation of thin polymer films inevitably gives rise to microstructural damage that is spatially heterogeneous and, to some extent, stochastic in nature. Such physically relevant microdamage does not necessarily evolve monotonically with applied strain and can therefore manifest as nontrivial or apparently irregular trends in the extracted spectral parameters. This effect is further amplified by the intrinsically low scattering efficiency of Raman spectroscopy, which enhances the influence of local variations and signal fluctuations on the measured response. Consequently, the observed strain dependence should be interpreted in terms of dominant physical regimes and reproducible trends rather than as strictly continuous or deterministic trajectories.
The 1377 cm^{-1} mode provides insight into how tensile strain redistributes micro-

scopic environments. In PET/P3HT, unannealed films exhibit negligible band-position shifts but pronounced FWHM narrowing, indicating selective engagement of mechanically coupled chain populations and largely elastic deformation. Mild annealing at 50 °C shifts the response toward systematic linewidth broadening with minimal wavenumber change, reflecting heterogeneous microstrain within a semi-crystalline morphology. At 75 °C annealing, small but persistent redshifts accompanied by enhanced linewidth broadening reveal a transition to brittle, defect-mediated deformation within highly ordered lamellar domains. Introducing a PEDOT:PSS interlayer modifies this behavior across all annealing conditions. In unannealed trilayers, PEDOT:PSS enhances mechanical coupling and suppresses localized stress concentrations, leading to smoother and more reversible linewidth variations. In annealed films, the interlayer suppresses large irreversible shifts and redistributes strain more uniformly, delaying microstructural damage. Overall, PEDOT:PSS preserves strain sensitivity while shifting the balance toward recoverable deformation.
The 1445 cm^{-1} band, dominated by the symmetric C=C stretching vibration of the P3HT backbone, provides a more direct probe of backbone-level deformation. In PET/P3HT, unannealed films show strain-induced blueshifts accompanied by linewidth narrowing at low to intermediate strain, consistent with increased torsional disorder coexisting with selective engagement of load-bearing chains. At higher strain, linewidth broadening signals the onset of heterogeneous deformation. Moderate annealing at 50 °C produces a mixed elastic-plastic response, with alternating narrowing and broadening reflecting nonuniform load sharing between crystalline and amorphous regions. In contrast, highly annealed films exhibit pronounced redshifts and strong linewidth broadening that persist after unloading, indicating irreversible, defect-dominated reorganization within brittle crystalline domains. The introduction of PEDOT:PSS again alters this response. In unannealed trilayers, strain-induced shifts and linewidth changes are modest and evolve smoothly, reflecting improved mechanical coupling and reduced strain localization. In annealed systems, PEDOT:PSS suppresses the severe broadening and uniformly redshifted behavior observed in PET/P3HT, even at high strain, demonstrating efficient dissipation of strain energy and stabilization of the P3HT microstructure.
Taken together, these results establish that mechanical stretching does not universally enhance order in conjugated polymer films. Instead, the strain response reflects a balance between processing-induced constraint and deformation-induced redistribution, governed jointly by thermal history and stack architecture. The PEDOT:PSS interlayer plays an active mechanical role by redistributing strain, suppressing defect accumulation, and stabilizing ordered domains, in addition to

its established electronic function. Raman spectroscopy combined with controlled mechanical loading thus provides a direct probe into how backbone conformation, microstructural order, interfacial mechanics, and damage accumulation evolve under strain. The framework established here offers practical guidance for defining safe deformation regimes and for the rational design of mechanically robust organic semiconductor stacks for flexible and wearable optoelectronic applications.

Chapter 9

Conclusion

9.1 Summary

This thesis examined how mechanical strain affects the optical and molecular behaviour of thin-film layers used in flexible organic solar cells. The central objective was to establish a physically consistent basis for interpreting strain effects in multilayer stacks by systematically investigating the behaviour of individual functional layers.

A key premise of this work is that device-level strain responses cannot be understood without prior knowledge of how individual functional layers behave under deformation. Measurements performed only at the molecular scale often do not translate directly to macroscopic behaviour. Conversely, device-level observations obscure the distinct contributions of substrates, active layers, and interfaces. This work therefore focused on the thin-film scale as an intermediate and necessary level of description.

By probing strain-dependent optical response and vibrational signatures under controlled and application-relevant conditions, the thesis demonstrates that strain accommodation is highly layer dependent. It is expressed through different balances between recoverable alignment, retained structural reconfiguration, and defect-driven heterogeneity. Elastic response, irreversible structural modification, and defect accumulation emerge at different strain levels depending on the role of each layer in the stack. These behaviours are not continuous with strain and cannot be inferred from microscopic considerations alone.

The results further show that optical stability and molecular stability do not necessarily coincide. Electronic and optical observables may remain unchanged over a given strain window, while molecular reorganization and structural fatigue already take place. This distinction is essential for reliable interpretation of strained device

measurements and long-term operation.
Although the experimental scope is intentionally constrained, the outcomes provide quantitative, strain-dependent descriptors that can be parameterized and incorporated directly into mechanical and optoelectronic models. From an electrical engineering perspective, the work establishes a structured framework for linking deformation, thin-film response, and device-relevant behaviour in flexible organic electronics.

9.2 Perspectives

The findings of this thesis define several clear directions for future work. These directions follow naturally from the limitations that were deliberately imposed to maintain physical clarity and experimental control.
First, the mechanical loading conditions can be extended beyond uniaxial tensile strain. Biaxial deformation, cyclic loading, and bending-induced strain would provide access to fatigue behaviour and failure accumulation that are directly relevant to real operating conditions.
Second, time-dependent effects merit further investigation. Strain relaxation, creep, and long-term structural evolution under sustained load were not addressed here. These effects are expected to play a critical role in device lifetime and stability.
Third, additional characterization techniques could complement the present framework. In-situ optical measurements during deformation, structural probes sensitive to mesoscale ordering, and correlated electrical measurements would provide a more complete picture of strain-induced evolution across length scales.
Fourth, the layer-resolved approach developed in this thesis can be extended to full device stacks. Once individual layer responses are quantitatively established, device-level measurements can be interpreted without relying on implicit or arbitrary assumptions about strain transfer. This includes explicit treatment of interlayers that redistribute strain rather than simply suppressing it.
Finally, the framework is not limited to organic solar cells. Any multilayer flexible electronic system faces similar challenges in connecting microscopic reorganization to macroscopic function. The approach presented here therefore provides a general basis for strain-aware modeling and design in flexible electronic technologies.

Bibliography

[1] D. Kearns and M. Calvin. "Photovoltaic Effect and Photoconductivity in Laminated Organic Systems". *Journal of Chemical Physics* vol. 29, no. 4 (1958), pp. 950–951. DOI: 10.1063/1.1744619.

[2] M. Pope and C. E. Swenberg. *Electronic Processes in Organic Crystals and Polymers*. New York, NY, USA: Oxford University Press, 1999.

[3] C. W. Tang. "Two-Layer Organic Photovoltaic Cell". *Applied Physics Letters* vol. 48, no. 2 (1986), pp. 183–185. DOI: 10.1063/1.96937.

[4] G. Yu, J. Gao, J. C. Hummelen, F. Wudl, and A. J. Heeger. "Polymer Photovoltaic Cells: Enhanced Efficiencies via a Network of Internal Donor–Acceptor Heterojunctions". *Science* vol. 270, no. 5243 (1995), pp. 1789–1791. DOI: 10.1126/science.270.5243.1789.

[5] C. Wu and H. Murata. "Thinking Small for Solar". *MRS Bulletin* vol. 37, no. 3 (2012), pp. 194–195. DOI: 10.1557/mrs.2012.62.

[6] Y. Yang, Z. G. Zhang, H. Bin, S. Chen, L. Gao, L. Xue, C. Yang, and Y. Li. "Side-Chain Isomerization on an n-Type Organic Semiconductor ITIC Acceptor Makes 11.77% High Efficiency Polymer Solar Cells". *Journal of the American Chemical Society* vol. 138, no. 45 (2016), pp. 15011–15018. DOI: 10.1021/jacs.6b09110.

[7] C. Li, J. Zhou, J. Song, et al. "Non-Fullerene Acceptors with Branched Side Chains and Improved Molecular Packing to Exceed 18% Efficiency in Organic Solar Cells". *Nature Energy* vol. 6 (2021), pp. 605–613. DOI: 10.1038/s41560-021-00820-x.

[8] B. Liang, X. Chen, X. Wang, H. Yuan, A. Sun, Z. Wang, L. Hu, G. Hou, Y. Zhao, and X. Zhang. "Progress in Crystalline Silicon Heterojunction Solar Cells". *Journal of Materials Chemistry A* vol. 13, no. 4 (2025), pp. 2441–2477. DOI: 10.1039/D4TA06224H.

[9] T. D. Raju, V. Murugadoss, K. A. Nirmal, T. D. Dongale, A. V. Kesavan, and T. G. Kim. "Advancements in Perovskites for Solar Cell Commercialization: A Review". *Advanced Powder Materials* vol. 4, no. 2 (2025), p. 100275. DOI: 10.1016/j.apmate.2025.100275.

[10] Y. Jiang, S. Sun, R. Xu, et al. "Non-Fullerene Acceptor with Asymmetric Structure and Phenyl-Substituted Alkyl Side Chain for 20.2% Efficiency Organic Solar Cells". *Nature Energy* vol. 9 (2024), pp. 975–986. DOI: 10.1038/s41560-024-01557-z.

[11] Y. Li, W. Huang, D. Zhao, L. Wang, Z. Jiao, Q. Huang, P. Wang, M. Sun, and G. Yuan. "Recent Progress in Organic Solar Cells: A Review on Materials from Acceptor to Donor". *Molecules* vol. 27, no. 6 (2022), p. 1800. DOI: 10.3390/molecules27061800.

[12] Z. Chen et al. "20.2% Efficiency Organic Photovoltaics Employing a π-Extension Quinoxaline-Based Acceptor with Ordered Arrangement". *Advanced Materials* vol. 36 (2024), p. 2406690. DOI: 10.1002/adma.202406690.

[13] K. Liu, Y. Jiang, G. Ran, F. Liu, W. Zhang, and X. Zhu. "19.7% Efficiency Binary Organic Solar Cells Achieved by Selective Core Fluorination of Non-fullerene Electron Acceptors". *Joule* vol. 8, no. 3 (2024), pp. 835–851. DOI: 10.1016/j.joule.2024.01.005.

[14] L. Zhu, M. Zhang, J. Xu, et al. "Single-Junction Organic Solar Cells with Over 19% Efficiency Enabled by a Refined Double-Fibril Network Morphology". *Nature Materials* vol. 21 (2022), pp. 656–663. DOI: 10.1038/s41563-022-01244-y.

[15] J. Wang et al. "Tandem Organic Solar Cells with 20.6% Efficiency Enabled by Reduced Voltage Losses". *National Science Review* vol. 10, no. 6 (2023), nwad085. DOI: 10.1093/nsr/nwad085.

[16] R. Zhang, H. Chen, T. Wang, et al. "Equally High Efficiencies of Organic Solar Cells Processed from Different Solvents Reveal Key Factors for Morphology Control". *Nature Energy* vol. 10 (2025), pp. 124–134. DOI: 10.1038/s41560-024-01678-5.

[17] S. E. Root, S. Savagatrup, A. D. Printz, D. Rodriquez, and D. J. Lipomi. "Mechanical Properties of Organic Semiconductors for Stretchable, Highly Flexible, and Mechanically Robust Electronics". *Chemical Reviews* vol. 117, no. 9 (2017), pp. 6467–6499. DOI: 10.1021/acs.chemrev.7b00003.

[18] M. Li, J. Zheng, X. Wang, et al. "Light-Responsive Self-Strained Organic Semiconductor for Large Flexible OFET Sensing Array". *Nature Communications* vol. 13 (2022), p. 4912. DOI: 10.1038/s41467-022-32647-9.

[19] M. Kaltenbrunner, M. White, E. D. Głowacki, et al. "Ultrathin and Lightweight Organic Solar Cells with High Flexibility". *Nature Communications* vol. 3 (2012), p. 770. DOI: 10.1038/ncomms1772.

[20] D. J. Lipomi, B. C.-K. Tee, M. Vosgueritchian, and Z. Bao. "Stretchable Organic Solar Cells". *Advanced Materials* vol. 23 (2011), pp. 1771–1775. DOI: 10.1002/adma.201004426.

[21] F. Yang, Y. Huang, Y. Li, et al. "Large-Area Flexible Organic Solar Cells". *NPJ Flexible Electronics* vol. 5 (2021), p. 30. DOI: 10.1038/s41528-021-00128-6.

[22] J. Zhu, J. Xia, Y. Li, and Y. Li. "Perspective on Flexible Organic Solar Cells for Self-Powered Wearable Applications". *ACS Applied Materials & Interfaces* vol. 17, no. 4 (2025), pp. 5595–5608. DOI: 10.1021/acsami.4c12238.

[23] Y. Ding, S. Xiong, W. A. Memon, D. Zhang, Z. Wang, M. Li, Z. Deng, H. Li, M. Shao, and F. He. "High-Performance Intrinsically-Stretchable Organic Solar Cells Enabled by Electron Acceptors with Flexible Linkers". *Angewandte Chemie International Edition* vol. 64 (2025), e202421430. DOI: 10.1002/anie.202421430.

[24] M. Riede, D. Spoltore, and K. Leo. "Organic Solar Cells—The Path to Commercial Success". *Advanced Energy Materials* vol. 11 (2021), p. 2002653. DOI: 10.1002/aenm.202002653.

[25] R. Suthar, H. Dahiya, S. Karak, and G. D. Sharma. "Indoor Organic Solar Cells for Low-Power IoT Devices: Recent Progress, Challenges, and Applications". *Journal of Materials Chemistry C* vol. 11, no. 37 (2023), pp. 12486–12510. DOI: 10.1039/D3TC02570E.

[26] N. K. Wardani, M. Jahandar, J. Heo, Y. H. Kim, S. Kim, and D. C. Lim. "Enhancing Physicochemical Durability and Photoelectronic Performance Beyond Bendable Large-Area Organic Photoelectronic Devices Through Tailored Multilayer Interface". *Chemical Engineering Journal* vol. 502 (2024), p. 157958. DOI: 10.1016/j.cej.2024.157958.

[27] E. Dauzon, X. Sallenave, C. Plesse, F. Goubard, A. Amassian, and T. D. Anthopoulos. "Pushing the Limits of Flexibility and Stretchability of Solar Cells: A Review". *Advanced Materials* vol. 33, no. 36 (2021), p. 2101469. DOI: 10.1002/adma.202101469.

[28] G. J. N. Wang, A. Gasperini, and Z. Bao. "Stretchable Polymer Semiconductors for Plastic Electronics". *Advanced Electronic Materials* vol. 4, no. 2 (2018), p. 1700429. DOI: 10.1002/aelm.201700429.

[29] G. Menichetti, R. Colle, and G. Grosso. "Strain Modulation of Band Offsets at the PCBM/P3HT Heterointerface". *The Journal of Physical Chemistry C* vol. 121, no. 25 (2017), pp. 13707–13716. DOI: 10.1021/acs.jpcc.7b02717.

[30] T. Kim, S. Oh, U. Choudhry, C. D. Meinhart, M. L. Chabinyc, and B. Liao. "Transient Strain-Induced Electronic Structure Modulation in a Semiconducting Polymer Imaged by Scanning Ultrafast Electron Microscopy". *Nano Letters* vol. 21, no. 21 (2021), pp. 9146–9152. DOI: 10.1021/acs.nanolett.1c02963.

[31] M. Ghorab, A. K. Ranga, P. Donfack, A. Materny, V. Wagner, and M. Joodaki. "Strain-Induced Optical and Molecular Transformations in Poly(Ethylene Terephthalate) Films for Organic Electronic Applications". *Advanced Photonics Research* (2025), p. 2500081. DOI: 10.1002/adpr.202500081.

[32] R. Z. Aboutorabi and M. Joodaki. "Thermal Analysis of Organic Solar Cells Using an Enhanced Opto-Thermal Model". *Organic Electronics* vol. 25 (2015), pp. 184–192. DOI: 10.1016/j.orgel.2015.06.034.

[33] R. Z. Aboutorabi and M. Joodaki. "A Tripartite Physics-Based Model for Organic Solar Cells". *Proceedings of the 29th European Photovoltaic Solar Energy Conference and Exhibition (EU PVSEC 2014)*. Munich, Germany, Sept. 2014, pp. 1592–1596. DOI: 10.4229/EUPVSEC20142014-3BV.5.46.

[34] A. Khorami and M. Joodaki. "Extracting Voltage-Dependent Series Resistance of Single Diode Model for Organic Solar Cells". *SN Applied Sciences* vol. 1, no. 6 (2019), p. 619. DOI: 10.1007/s42452-019-0613-2.

[35] M. Salari and M. Joodaki. "Investigation of Electrical Characteristics Dependency of Roll-to-Roll Printed Solar Cells With Silver Electrodes on Mechanical Tensile Strain". *IEEE Transactions on Device and Materials Reliability* vol. 19, no. 4 (2019), pp. 718–722. DOI: 10.1109/TDMR.2019.2949116.

[36] M. Salari, M. Joodaki, and S. Mehregan. "Experimental Investigation of Tensile Mechanical Strain Influence on the Dark Current of Organic Solar Cells". *Organic Electronics* vol. 54 (2018), pp. 192–196. DOI: 10.1016/j.orgel.2017.12.047.

[37] M. Joodaki and M. Salari. "Investigation of the Tensile Strain Influence on Flicker Noise of Organic Solar Cells Under Dark Condition". *Organic Electronics* vol. 59 (2018), pp. 230–235. DOI: 10.1016/j.orgel.2018.05.018.

[38] M. Ghorab, A. Fattah, and M. Joodaki. "Tensile Mechanical Strain Effects on the Electrical Characteristics of Roll-to-Roll Printed OSC". *IEEE Journal of Photovoltaics* vol. 12, no. 3 (2022), pp. 737–743. DOI: 10.1109/JPHOTOV.2022.3148717.

[39] L. Sun, Y. Chen, M. Sun, and Y. Zheng. "Organic Solar Cells: Physical Principle and Recent Advances". *Chemistry – An Asian Journal* vol. 18, no. 5 (2023), e202300006. DOI: 10.1002/asia.202300006.

[40] X. He, F. Qi, X. Zou, et al. "Selenium Substitution for Dielectric Constant Improvement and Hole-Transfer Acceleration in Non-Fullerene Organic Solar Cells". *Nature Communications* vol. 15 (2024), p. 2103. DOI: 10.1038/s41467-024-46352-2.

[41] J. D. Servaites, M. A. Ratner, and T. J. Marks. "Organic Solar Cells: A New Look at Traditional Models". *Energy & Environmental Science* vol. 4, no. 11 (2011), pp. 4410–4422. DOI: 10.1039/C1EE01663F.

[42] T. Fritsch, J. Kurpiers, S. Roland, N. Tokmoldin, S. Shoaee, T. Ferron, B. A. Collins, S. Janietz, K. Vandewal, and D. Neher. "On the Interplay Between CT and Singlet Exciton Emission in Organic Solar Cells with Small Driving Force and Its Impact on Voltage Loss". *Advanced Energy Materials* vol. 12 (2022), p. 2200641. DOI: 10.1002/aenm.202200641.

[43] Y. Firdaus, V. M. L. Corre, S. Karuthedath, et al. "Long-Range Exciton Diffusion in Molecular Non-Fullerene Acceptors". *Nature Communications* vol. 11 (2020), p. 5220. DOI: 10.1038/s41467-020-19029-9.

[44] V. Coropceanu, X. K. Chen, T. Wang, et al. "Charge-Transfer Electronic States in Organic Solar Cells". *Nature Reviews Materials* vol. 4 (2019), pp. 689–707. DOI: 10.1038/s41578-019-0137-9.

[45] Z. Zheng, N. R. Tummala, Y.-T. Fu, V. Coropceanu, and J.-L. Brédas. "Charge-Transfer States in Organic Solar Cells: Understanding the Impact of Polarization, Delocalization, and Disorder". *ACS Applied Materials & Interfaces* vol. 9, no. 21 (2017), pp. 18095–18102. DOI: 10.1021/acsami.7b02193.

[46] L. Krückemeier, P. Kaienburg, J. Flohre, et al. "Developing Design Criteria for Organic Solar Cells Using Well-Absorbing Non-Fullerene Acceptors". *Communications Physics* vol. 1 (2018), p. 27. DOI: 10.1038/s42005-018-0026-3.

[47] A. F. Marmolejo-Valencia, Z. Mata-Pinzón, and C. Amador-Bedolla. "Charge-Transfer Electronic States in Organic Solar Cells: A TDDFT Study". *Physical Chemistry Chemical Physics* vol. 23, no. 31 (2021), pp. 16806–16815. DOI: 10.1039/D1CP00723H.

[48] T. A. D. Peña et al. "Understanding the Charge Transfer State and Energy Loss Trade-Offs in Non-Fullerene-Based Organic Solar Cells". *ACS Energy Letters* vol. 6, no. 10 (2021), pp. 3408–3416. DOI: 10.1021/acsenergylett.1c01574.

[49] J. M. Hodgkiss, S. Albert-Seifried, A. Rao, A. J. Barker, A. R. Campbell, R. A. Marsh, and R. H. Friend. "Exciton-Charge Annihilation in Organic Semiconductor Films". *Advanced Functional Materials* vol. 22 (2012), pp. 1567–1577. DOI: 10.1002/adfm.201102433.

[50] B. Balraj, M. Raja, T. G. V. Prabhu, M. Balaji, J. Chandrasekaran, S. K. Nagarajan, M. Bharathi, S. Lee, and C. Sivakumar. "A Critical Review on Decade Progress and Future Prospects of P3HT:PCBM Bulk Heterojunction Solar Cells". *Solar Energy* vol. 297 (2025), p. 113574. DOI: 10.1016/j.solener.2025.113574.

[51] H. Bässler. "Charge Transport in Disordered Organic Photoconductors: A Monte Carlo Simulation Study". *Physica Status Solidi (b)* vol. 175 (1993), pp. 15–56. ISSN: 0370-1972. DOI: 10.1002/pssb.2221750102.

[52] H. Bässler and A. Köhler. "Charge Transport in Organic Semiconductors". *Topics in Current Chemistry* vol. 312 (2012), pp. 1–65. ISSN: 0340-1022. DOI: 10.1007/128_2011_218.

[53] R. Coehoorn, W. F. Pasveer, P. A. Bobbert, and M. A. J. Michels. "Charge-Carrier Concentration Dependence of the Hopping Mobility in Organic Materials with Gaussian Disorder". *Physical Review B* vol. 72, no. 15 (2005), pp. 155206-1–155206-20. DOI: 10.1103/PhysRevB.72.155206.

[54] A. Miller and E. Abrahams. "Impurity Conduction at Low Concentrations". *Physical Review* vol. 120, no. 3 (1960), pp. 745–755. DOI: 10.1103/PhysRev.120.745.

[55] N. Zhou and A. Facchetti. "Charge Transport and Recombination in Organic Solar Cells (OSCs)". *Organic and Hybrid Solar Cells*. Ed. by H. Huang and J. Huang. Cham: Springer, 2014. DOI: 10.1007/978-3-319-10855-1_2.

[56] V. Coropceanu, J. Cornil, D. A. da Silva Filho, Y. Olivier, R. Silbey, and J.-L. Brédas. "Charge Transport in Organic Semiconductors". *Chemical Review* vol. 107, no. 4 (2007), pp. 926–952. DOI: 10.1021/cr050140x.

[57] R. A. Street. "Localized State Distribution and Its Effect on Recombination in Organic Solar Cells". *Physical Review B* vol. 84, no. 7 (2011), p. 075208. DOI: 10.1103/PhysRevB.84.075208.

[58] E. L. Ratcliff, B. Zacher, and N. R. Armstrong. "Selective Interlayers and Contacts in Organic Photovoltaic Cells". *The Journal of Physical Chemistry Letters* vol. 2, no. 11 (2011), pp. 1337–1350. DOI: 10.1021/jz2002259.

[59] A. Opitz, J. Frisch, R. Schlesinger, A. Wilke, and N. Koch. "Energy Level Alignment at Interfaces in Organic Photovoltaic Devices". *Journal of Electron Spectroscopy and Related Phenomena* vol. 190 (2013), pp. 12–24. ISSN: 0368-2048. DOI: 10.1016/j.elspec.2012.11.008.

[60] C. Zhao, C. G. Tang, Z. L. Seah, Y. Zhao, S. R. P. Silva, and L. S. Wong. "Improving Organic Photovoltaic Cells by Forcing Electrode Work Function Well Beyond Onset of Ohmic Transition". *Nature Communication* vol. 12 (2021), p. 2250. DOI: 10.1038/s41467-021-22358-y.

[61] P. Cheng and X. Zhan. "Stability of Organic Solar Cells: Challenges and Strategies". *Chemical Society Reviews* vol. 45, no. 9 (2016), pp. 2544–2582. DOI: 10.1039/C5CS00593K.

[62] H.-L. Yip and A. K.-Y. Jen. "Recent Advances in Solution-Processed Interfacial Materials for Efficient and Stable Polymer Solar Cells". *Energy Environmental Science* vol. 5, no. 3 (2012), pp. 5994–6011. DOI: 10.1039/C2EE02806A.

[63] D. J. Lipomi, H. Chong, M. Vosgueritchian, J. Mei, and Z. Bao. "Toward Mechanically Robust and Intrinsically Stretchable Organic Solar Cells: Evolution of Photovoltaic Properties with Tensile Strain". *Sol. Ener. Mat. and Sol. Cells* vol. 107 (2012), pp. 355–365. ISSN: 0927-0248. DOI: 10.1016/j.solmat.2012.07.013.

[64] L. Li, L. Han, H. Hu, and R. Zhang. "A Review on Polymers and Their Composites for Flexible Electronics". *Materials Advances* vol. 4, no. 3 (2023), pp. 726–746. DOI: 10.1039/D2MA00940D.

[65] D. J. Lipomi, J. A. Lee, M. Vosgueritchian, B. C.-K. Tee, J. A. Bolander, and Z. Bao. "Electronic Properties of Transparent Conductive Films of PEDOT:PSS on Stretchable Substrates". *Chemistry of Materials* vol. 24, no. 2 (2012), pp. 373–382. DOI: 10.1021/cm203216m.

[66] Z. Ding, J. Hua, Z. Gao, M. Wang, K. Zhao, and Y. Han. "Molecular Weight Optimization for Intrinsically Stretchable Conjugated Polymers: From Film Microstructure to Strain-Insensitive Performance". *Journal of Materials Chemistry C* vol. 13, no. 25 (2025), pp. 12612–12627. DOI: 10.1039/D5TC01357G.

[67] Y. Lin and X. Zhan. "Non-Fullerene Acceptors for Organic Photovoltaics: An Emerging Horizon". *Materials Horizons* vol. 1, no. 5 (2014), pp. 470–488. DOI: 10.1039/C4MH00042K.

[68] Y. Lin, J. Wang, Z. Zhang, H. Bai, Y. Li, D. Zhu, and X. Zhan. "An Electron Acceptor Challenging Fullerenes for Efficient Polymer Solar Cells". *Advanced Materials* vol. 27 (2015), pp. 1170–1174. DOI: 10.1002/adma.201404317.

[69] C. J. Brabec and V. Dyakonov. "Photoinduced Charge Transfer in Bulk Heterojunction Composites". *Organic Photovoltaics: Concepts and Realization*. Ed. by C. J. Brabec, V. Dyakonov, J. Parisi, and N. S. Sariciftci. Berlin, Heidelberg: Springer Berlin Heidelberg, 2003, pp. 1–56. ISBN: 978-3-662-05187-0. DOI: 10.1007/978-3-662-05187-0_1.

[70] K. Vandewal, K. Tvingstedt, A. Gadisa, O. Inganäs, and J. V. Manca. "On the Origin of the Open-Circuit Voltage of Polymer–Fullerene Solar Cells". *Nature Materials* vol. 8 (2009), pp. 904–909. DOI: 10.1038/nmat2548.

[71] B. Qi and J. Wang. "Fill Factor in Organic Solar Cells". *Physical Chemistry Chemical Physics* vol. 15, no. 23 (2013), pp. 8972–8982. DOI: 10.1039/C3CP51383A.

[72] M. L. D. Lorenzo. "Crystallization of Poly(ethylene terephthalate): A Review". *Polymers (Basel)* vol. 16, no. 14 (2024), p. 1975. DOI: 10.3390/polym16141975.

[73] M. D. Polêto and J. A. Lemkul. "Structural and Electronic Properties of Poly(ethylene terephthalate) (PET) from Polarizable Molecular Dynamics Simulations". *Macromolecules* vol. 58, no. 1 (2025), pp. 403–414. DOI: 10.1021/acs.macromol.4c02109.

[74] T. A. Osswald and G. Menges. *Material Science of Polymers for Engineers*. 3rd ed. Munich: Carl Hanser Verlag, 2012. ISBN: 978-1-56990-514-2. DOI: 10.3139/9781569905241.

[75] J. F. Rabek. *Experimental Methods in Polymer Chemistry: Physical Principles and Applications*. New York: John Wiley & Sons Ltd, 1980. ISBN: 978-0471276043.

[76] M. I. Avadanei, D. G. Dimitriu, and D. O. Dorohoi. "Optical Anisotropy of Polyethylene Terephthalate Films Characterized by Spectral Means". *Polymers (Basel)* vol. 16, no. 6 (2024), p. 850. DOI: 10.3390/polym16060850.

[77] V. Zardetto, T. M. Brown, A. Reale, and A. D. Carlo. "Substrates for Flexible Electronics: A Practical Investigation on the Electrical, Film Flexibility, Optical, Temperature, and Solvent Resistance Properties". *Journal of Polymer Science B Polymer Physics* vol. 49 (2011), pp. 638–648. DOI: 10.1002/polb.22227.

[78] G. Primc and M. Mozetič. "Surface Modification of Polymers by Plasma Treatment for Appropriate Adhesion of Coatings". *Materials* vol. 17, no. 7 (2024), p. 1494. DOI: 10.3390/ma17071494.

[79] A. T. Kleinschmidt, S. E. Root, and D. J. Lipomi. "Poly(3-hexylthiophene) (P3HT): Fruit Fly or Outlier in Organic Solar Cell Research?" *Journal of Materials Chemistry A* vol. 5, no. 23 (2017), pp. 11396–11400. DOI: 10.1039/C6TA08317J.

[80] R. D. McCullough, R. D. Lowe, M. Jayaraman, and D. L. Anderson. "Design, Synthesis, and Control of Conducting Polymer Architectures: Structurally Homogeneous Poly(3-alkylthiophenes)". *The Journal of Organic Chemistry* vol. 58, no. 4 (1993), pp. 904–912. DOI: 10.1021/jo00056a024.

[81] I. Osaka and R. D. McCullough. "Advances in Molecular Design and Synthesis of Regioregular Polythiophenes". *Accounts of Chemical Research* vol. 41, no. 9 (2008), pp. 1202–1214. DOI: 10.1021/ar800130s.

[82] M. Brinkmann. "Structure and Morphology Control in Thin Films of Regioregular Poly(3-hexylthiophene)". *Journal of Polymer Science B Polymer Physics* vol. 49 (2011), pp. 1218–1233. DOI: 10.1002/polb.22310.

[83] R. D. McCullough, S. Tristram-Nagle, S. P. Williams, R. D. Lowe, and M. Jayaraman. "Self-Orienting Head-to-Tail Poly(3-alkylthiophenes): New Insights on Structure–Property Relationships in Conducting Polymers". *Journal of*

the American Chemical Society vol. 115, no. 11 (1993), pp. 4910–4911. DOI: 10.1021/ja00064a070.

[84] R. Noriega, J. Rivnay, K. Vandewal, F. P. V. Koch, N. Stingelin, P. Smith, M. F. Toney, and A. Salleo. "A General Relationship Between Disorder, Aggregation and Charge Transport in Conjugated Polymers". *Nature Material* vol. 12 (2013), pp. 1038–1044. DOI: 10.1038/nmat3722.

[85] J. Rivnay, R. Noriega, R. J. Kline, A. Salleo, and M. F. Toney. "Quantitative Analysis of Lattice Disorder and Crystallite Size in Organic Semiconductor Thin Films". *Physical Review B* vol. 84, no. 4 (2011), p. 045203. DOI: 10.1103/PhysRevB.84.045203.

[86] D. P. McMahon, D. L. Cheung, L. Goris, J. Dacuña, A. Salleo, and A. Troisi. "Relation Between Microstructure and Charge Transport in Polymers of Different Regioregularity". *The Journal of Physical Chemistry C* vol. 115, no. 39 (2011), pp. 19386–19393. DOI: 10.1021/jp207026s.

[87] F. C. Spano. "The Spectral Signatures of Frenkel Polarons in H- and J-Aggregates". *Accounts of Chemical Research* vol. 43, no. 3 (2010), pp. 429–439. DOI: 10.1021/ar900233v.

[88] R. Ghosh and F. C. Spano. "Excitons and Polarons in Organic Materials". *Accounts of Chemical Research* vol. 53, no. 10 (2020), pp. 2201–2211. DOI: 10.1021/acs.accounts.0c00349.

[89] M. C. Scharber and N. S. Sariciftci. "Efficiency of Bulk-Heterojunction Organic Solar Cells". *Progress in Polymer Science* vol. 38, no. 12 (2013), pp. 1929–1940. DOI: 10.1016/j.progpolymsci.2013.05.001.

[90] J. Clark, C. Silva, R. H. Friend, and F. C. Spano. "Role of Intermolecular Coupling in the Photophysics of Disordered Organic Semiconductors: Aggregate Emission in Regioregular Polythiophene". *Physical Review Letters* vol. 98, no. 20 (2007), p. 206406. DOI: 10.1103/PhysRevLett.98.206406.

[91] F. C. Spano and C. Silva. "H- and J-Aggregate Behavior in Polymeric Semiconductors". *Annual Review of Physical Chemistry* vol. 65 (2014), pp. 477–500. DOI: 10.1146/annurev-physchem-040513-103639.

[92] N. J. Hestand and F. C. Spano. "Expanded Theory of H- and J-Molecular Aggregates: The Effects of Vibronic Coupling and Intermolecular Charge Transfer". *Chemical Review* vol. 118, no. 15 (2018), pp. 7069–7163. DOI: 10.1021/acs.chemrev.7b00581.

[93] W. C. Tsoi, D. T. James, J. S. Kim, P. G. Nicholson, C. E. Murphy, D. D. C. Bradley, J. Nelson, and J.-S. Kim. "The Nature of In-Plane Skeleton Raman Modes of P3HT and Their Correlation to the Degree of Molecular Order in P3HT:PCBM Blend Thin Films". *Journal of the American Chemical Society* vol. 133, no. 25 (2011), pp. 9834–9843. DOI: 10.1021/ja2013104.

[94] F. C. Spano. "Modeling Disorder in Polymer Aggregates: The Optical Spectroscopy of Regioregular Poly(3-hexylthiophene) Thin Films". *The Journal of Chemical Physics* vol. 122, no. 23 (2005), p. 234701. DOI: 10.1063/1.1914768.

[95] S. Savagatrup, A. D. Printz, T. F. O'Connor, A. V. Zaretski, D. Rodriquez, E. J. Sawyer, K. M. Rajan, R. I. Acosta, S. E. Roota, and D. J. Lipomi. "Mechanical Degradation and Stability of Organic Solar Cells: Molecular and Microstructural Determinants". *Energy Environmental Science* vol. 8 (2015), pp. 55–80. DOI: 10.1039/C4EE02657H.

[96] J.-L. Brédas, D. Beljonne, V. Coropceanu, and J. Cornil. "Charge-Transfer and Energy-Transfer Processes in π-Conjugated Oligomers and Polymers: A Molecular Picture". *Chemical Review* vol. 104, no. 11 (2004), pp. 4971–5003. DOI: 10.1021/cr040084k.

[97] P. W. Atkins and R. S. Friedman. *Molecular Quantum Mechanics*. 5th. Oxford: Oxford University Press, 2010. ISBN: 9780199541423.

[98] D. L. Pavia, G. M. Lampman, G. S. Kriz, and J. A. Vyvyan. *Introduction to Spectroscopy*. 5th. Boston: Cengage Learning, 2014, p. 784. ISBN: 9781305177826.

[99] E. W. Knapp. "Lineshapes of Molecular Aggregates, Exchange Narrowing and Intersite Correlation". *Chemical Physics* vol. 85, no. 1 (1984), pp. 73–82. DOI: 10.1016/S0301-0104(84)85174-5.

[100] F. C. Spano and H. Yamagata. "Vibronic Coupling in J-Aggregates and Beyond: A Direct Means of Determining the Exciton Coherence Length from the Photoluminescence Spectrum". *The Journal of Physical Chemistry B* vol. 115, no. 18 (2011), pp. 5133–5143. DOI: 10.1021/jp104752k.

[101] D. Beljonne, J. Cornil, R. J. Silbey, P. Millié, and J.-L. Brédas. "Interchain Interactions in Conjugated Materials: The Exciton Model Versus the Supermolecular Approach". *Th Journal of Chemical Physics* vol. 112, no. 10 (2000), pp. 4749–4758. DOI: 10.1063/1.481031.

[102] J. Tauc, R. Grigorovici, and A. Vancu. "Optical Properties and Electronic Structure of Amorphous Germanium". *physica status solidi (b)* vol. 15, no. 2 (1966), pp. 627–637. DOI: 10.1002/pssb.19660150224.

[103] P. Y. Yu and M. Cardona. *Fundamentals of Semiconductors: Physics and Materials Properties*. 4th ed. Berlin, Heidelberg: Springer-Verlag, 2010. DOI: 10.1007/978-3-642-00710-1.

[104] B. Ferreira, P. F. da Silva, J. S. S. de Melo, J. Pina, and A. Maçanita. "Excited-State Dynamics and Self-Organization of Poly(3-hexylthiophene) (P3HT) in Solution and Thin Films". *The Journal of Physical Chemistry B* vol. 116, no. 8 (2012), pp. 2347–2355. DOI: 10.1021/jp207418q.

[105] O. P. Dimitriev, D. A. Blank, C. Ganser, and C. Teichert. "Effect of the Polymer Chain Arrangement on Exciton and Polaron Dynamics in P3HT and P3HT:PCBM Films". *The Journal of Physical Chemistry C* vol. 122, no. 30 (2018), pp. 17096–17109. DOI: 10.1021/acs.jpcc.8b05155.

[106] G. Lu, Z. Shen, H. Wang, L. Bu, and G. Lu. "Optical Interference on the Measurement of Film-Depth-Dependent Light Absorption Spectroscopy and a Correction Approach". *Review of Scientific Instruments* vol. 94, no. 2 (2023), p. 023907. DOI: 10.1063/5.0138336.

[107] M. Milosevic and S. W. King. "Validation of a Correction Procedure for Removing the Optical Effects from Transmission Spectra of Thin Films on Substrates". *Journal of Applied Physics* vol. 112, no. 9 (2012), p. 093514. DOI: 10.1063/1.4764346.

[108] D. J. Gardiner. "Introduction to Raman Scattering". *Practical Raman Spectroscopy*. Ed. by D. J. Gardiner and P. R. Graves. Berlin, Heidelberg: Springer, 1989. ISBN: 978-3-540-50254-8. DOI: 10.1007/978-3-642-74040-4_1.

[109] G. Keresztury. "Raman Spectroscopy: Theory". *Handbook of Vibrational Spectroscopy*. Ed. by J. M. Chalmers and P. R. Griffiths. John Wiley & Sons, 2006. DOI: 10.1002/0470027320.s0109.

[110] D. A. Long. "Quantum Mechanical Theory of Rayleigh and Raman Scattering". *The Raman Effect*. Ed. by D. A. Long. John Wiley & Sons, 2002. DOI: 10.1002/0470845767.ch4.

[111] E. B. Wilson, J. C. Decius, and P. C. Cross. *Molecular Vibrations: The Theory of Infrared and Raman Vibrational Spectra*. New York: McGraw-Hill, 1955.

[112] G. Turrell and J. Corset, eds. *Raman Microscopy: Developments and Applications*. Academic Press, 1996. ISBN: 9780121896904.

[113] D. A. Long. "Rotational and Vibration–Rotation Raman Scattering". *The Raman Effect*. Ed. by D. A. Long. John Wiley & Sons, 2002. DOI: 10.1002/0470845767.ch6.

[114] M. Yin, L. Zhao, S. Liu, S. Tian, F. Meng, and L. Luo. "Conjugation Length-Dependent Raman Scattering Intensity of Conjugated Polymers". *Macromolecular Rapid Communications* vol. 44 (2023), p. 2300412. DOI: 10.1002/marc.202300412.

[115] K. C. Cole, A. Ajji, and É. Pellerin. "New Insights into the Development of Ordered Structure in Poly(ethylene terephthalate). Results from External Reflection Infrared Spectroscopy". *Macromolecules* vol. 35, no. 3 (2002), pp. 770–784. DOI: 10.1021/ma011492i.

[116] F. J. Boerio, S. K. Bahl, and G. E. McGraw. "Vibrational Analysis of Polyethylene Terephthalate and its Deuterated Derivatives". *Journal of Polymer Science: Polymer Physics Edition* vol. 14, no. 6 (1976), pp. 1029–1046. DOI: 10.1002/pol.1976.180140607.

[117] E. Rebollar, S. Pérez, M. Hernández, C. Domingo, M. Martín, T. A. Ezquerra, J. P. García-Ruiz, and M. Castillejo. "Physicochemical Modifications Accompanying UV Laser Induced Surface Structures on Poly(Ethylene Terephthalate) and Their Effect on Adhesion of Mesenchymal Cells". *Physical Chemistry Chemical Physics* vol. 16 (33 2014), pp. 17551–17559. DOI: 10.1039/C4CP02434F.

[118] M. Richard-Lacroix and C. Pellerin. "Orientation and Structure of Single Electrospun Nanofibers of Poly(ethylene terephthalate) by Confocal Raman Spectroscopy". *Macromolecules* vol. 45, no. 4 (2012), pp. 1946–1953. DOI: 10.1021/ma202749d.

[119] I. Ward and J. Sweeney. "Anisotropic Mechanical Behaviour". *Mechanical Properties of Solid Polymers*. John Wiley & Sons, Ltd, 2012, pp. 167–226. ISBN: 9781119967125. DOI: 10.1002/9781119967125.ch8.

[120] J. K. Grey. "Resonance Raman Spectroscopy and Imaging of Franck–Condon Vibrational Activity and Morphology in Conjugated Polymers for Solar Cells". *Accounts of Chemical Research* vol. 52, no. 8 (2019), pp. 2221–2231. DOI: 10.1021/acs.accounts.9b00088.

[121] L. Brambilla, C. C. Ferrón, M. Tommasini, K. Hong, J. T. L. Navarrete, V. Hernández, and G. Zerbi. "Infrared and Multi-Wavelength Raman Spectroscopy of Regio-Regular P3HT and Its Deutero Derivatives". *Journal of Raman Spectroscopy* vol. 49 (2018), pp. 569–580. DOI: 10.1002/jrs.5301.

[122] H.-M. Liem, P. Etchegoin, K. S. Whitehead, and D. D. C. Bradley. "Raman Anisotropy Measurements: An Effective Probe of Molecular Orientation in Conjugated Polymer Thin Films". *Advanced Functional Materials* vol. 13 (2003), pp. 66–72. DOI: 10.1002/adfm.200390008.

[123] M. Campoy-Quiles, P. G. Etchegoin, and D. D. C. Bradley. "On the Optical Anisotropy of Conjugated Polymer Thin Films". *Physical Review B* vol. 72 (2005), p. 045209. DOI: 10.1103/PhysRevB.72.045209.

[124] J. González-Córdova, D. Ariza-Flores, J. Pérez-Huerta, J. Madrigal-Melchor, A. López-Miranda, and J. Ortega-Gallegos. "Optical Anisotropy Raman Response of Polyethylene terephthalate Strained Thin Films". *Physica B: Condensed Matter* vol. 654 (2023), p. 414693. DOI: 10.1016/j.physb.2023.414693.

[125] J. H. Werner. "Schottky barrier and pn-junction I/V plots — Small signal evaluation". *Applied Physics A* vol. 47 (1988), pp. 291–300. DOI: 10.1007/BF00615935.

[126] Q. Fan, W. Su, S. Chen, T.-S. Kim, L. Huang, C. Yang, and E. Wang. "Mechanically Robust All-Polymer Solar Cells from Narrow Band Gap Acceptors with Hetero-Bridging Atoms". *Joule* vol. 4 (2020), pp. 658–672. DOI: 10.1016/j.joule.2020.01.014.

[127] N. Hollingsworth, S. T. Hoffmann, and J. Clark. "Influence of Backbone Regioregularity on the Optoelectronic and Mechanical Response of Conjugated Polyelectrolyte-Based Hydrogels". *The Journal of Physical Chemistry B* vol. 127, no. 9 (2023), pp. 2277–2285. DOI: 10.1021/acs.jpcb.3c00152.

[128] B. O'Connor, R. J. Kline, B. R. Conrad, L. J. Richter, D. Gundlach, M. F. Toney, and D. M. DeLongchamp. "Anisotropic Structure and Charge Transport in Highly Strain-Aligned Regioregular Poly(3-hexylthiophene)". *Advanced Functional Materials* vol. 21, no. 19 (2011), pp. 3697–3705. DOI: 10.1002/adfm.201100904.

[129] D. Gargi, R. J. Kline, D. M. DeLongchamp, D. A. Fischer, M. F. Toney, and B. T. O'Connor. "Charge Transport in Highly Face-On Poly(3-Hexylthiophene) Films". *Journal of Physical Chemistry C* vol. 117 (2013), pp. 17421–17428. DOI: 10.1021/jp4050644.

[130] S. Wilken, D. Scheunemann, S. Dahlström, M. Nyman, J. Parisi, and R. Österbacka. "How to Reduce Charge Recombination in Organic Solar Cells: There are Still Lessons to Learn from P3HT:PCBM". *Advanced Electronic Materials* vol. 7, no. 5 (2021), p. 2001056. DOI: 10.1002/aelm.202001056.

[131] O. Ostroverkhova. "Organic Optoelectronic Materials: Mechanisms and Applications". *Chemistry Review* vol. 116, no. 22 (2016), pp. 13279–13412. DOI: 10.1021/acs.chemrev.6b00127.

[132] A. Müller, V. Jovanov, and V. Wagner. "Analytical Model (CELIC) for Describing Organic and Inorganic Solar Cells Based on Drift-Diffusion Calculations". *Applied Physics Letters* vol. 111, no. 2 (2017), p. 023506. DOI: 10.1063/1.4993778.

[133] S. Wageh, M. Raïssi, T. Berthelot, M. Laurent, D. Rousseau, A. M. Abusorrah, O. A. Al-Hartomy, and A. A. Al-Ghamdi. "Digital Printing of a Novel Electrode for Stable Flexible Organic Solar Cells with a Power Conversion Efficiency of 8.5%". *Scientific Reports* vol. 11 (2021), p. 14212. DOI: 10.1038/s41598-021-93365-8.

[134] O. Awartani, M. W. Kudenov, R. J. Kline, and B. T. O'Connor. "In-Plane Alignment in Organic Solar Cells to Probe the Morphological Dependence of Charge Recombination". *Advanced Functional Materials* vol. 25, no. 8 (2015), pp. 1296–1303. DOI: 10.1002/adfm.201403377.

[135] S. Gupta, M. Dixit, K. Sharma, and N. Saxena. "Mechanical Study of Metalized Polyethylene Terephthalate (PET) Films". *Surface and Coatings Technology* vol. 204, no. 15 (2009), pp. 661–666. DOI: 10.1016/j.surfcoat.2009.08.051.

[136] J. Y. Lim and S. Y. Kim. "Yield Strain Behavior of Poly(Ethylene Terephthalate): Correlation with Yield Stress Behavior in Strain Rate, Temperature, and Structure Dependence". *Polymer Journal* vol. 36 (2004), pp. 769–773. DOI: 10.1295/POLYMJ.36.769.

[137] F. Teng, G. Menary, S. Malinov, S. Yan, and J. B. Stevens. "Predicting the Multiaxial Stress-Strain Behavior of Polyethylene Terephthalate (PET) at Different Strain Rates and Temperatures Above Tg by Using an Artificial Neural Network". *Mechanics of Materials* vol. 165 (2022), p. 104175. DOI: 10.1016/j.mechmat.2021.104175.

[138] Y. Bin, K. Oishi, K. Yoshida, and M. Matsuo. "Mechanical Properties of Poly(ethylene terephthalate) Estimated in Terms of Orientation Distribution of Crystallites and Amorphous Chain Segments under Simultaneous Biaxially Stretching". *Polymer Journal* vol. 36 (2004), pp. 888–898. DOI: 10.1295/POLYMJ.36.888.

[139] J. K. Keum, J. Kim, S. M. Lee, H. H. Song, Y.-K. Son, J.-I. Choi, and S. S. Im. "Crystallization and Transient Mesophase Structure in Cold-Drawn PET Fibers". *Macromolecules* vol. 36, no. 26 (2003), pp. 9873–9878. DOI: 10.1021/ma034694i.

[140] A. Misra and R. S. Stein. "Stress-Induced Crystallization of Poly(Ethylene Terephthalate)". *Journal of Polymer Science: Polymer Physics Edition* vol. 17, no. 2 (1979), pp. 235–257. DOI: 10.1002/pol.1979.180170205.

[141] M. Ghorab, V. Wagner, and M. Joodaki. "Electrical Modeling of Active Layer Morphology Alterations in Response to the Applied Mechanical Strain in Organic Solar Cells". *2024 IEEE 24th International Conference on Nanotechnology (NANO)*. 2024, pp. 97–102. DOI: 10.1109/NANO61778.2024.10628870.

[142] A. Laskarakis and S. Logothetidis. "Study of the Electronic and Vibrational Properties of Poly(Ethylene Terephthalate) and Poly(Ethylene Naphthalate) Films". *Journal of Applied Physics* vol. 101, no. 5 (Mar. 2007), p. 053503. ISSN: 0021-8979. DOI: 10.1063/1.2709572.

[143] Z. Zhou, H. Jiang, H. Gu, X. Chen, H. Peng, Y. Liao, S. Liu, and X. Xie. "Strain-Optical Behavior of Polyethylene Terephthalate Film During Uniaxial Stretching Investigated by Mueller Matrix Ellipsometry". *Polymer* vol. 182 (2019), p. 121842. ISSN: 0032-3861. DOI: 10.1016/j.polymer.2019.121842.

[144] Y. Wu et al. "Strain Effects on the Work Function of an Organic Semiconductor". *Nature Communications* vol. 7 (2016), p. 10270. DOI: 10.1038/ncomms10270.

[145] C. Yang, J. Yoon, S. H. Kim, K. Hong, D. S. Chung, K. Heo, C. E. Park, and M. Ree. "Bending-Stress-Driven Phase Transitions in Pentacene Thin Films for Flexible Organic Field-Effect Transistors". *Applied Physics Letters* vol. 92, no. 24 (2008), p. 243305. DOI: 10.1063/1.2948862.

[146] Y. Wang, Z. Li, K. Niu, W. Xia, and A. Giuntoli. "A Molecular Dynamics Study of Mechanical and Conformational Properties of Conjugated Polymer Thin Films". *Macromolecules* vol. 57, no. 11 (2024), pp. 5130–5142. DOI: 10.1021/acs.macromol.4c00232.

[147] N. Tong, C.-j. Zhu, L.-x. Song, C.-h. Zhang, G.-q. Zhang, and Y.-x. Zhang. "Characteristics of Raman Spectra of Polyethylene Terephthalate". vol. 36, no. 01 (2016), pp. 114–118. DOI: 10.3724/SP.J.1249.2015.06594.

[148] S. Mosca, A. Milani, C. Castiglioni, V. H. Jolín, C. Meseguer, J. T. L. Navarrete, C. Zhao, K. Sugiyasu, and M. C. R. Delgado. "Raman Fingerprints of π-Electron Delocalization in Polythiophene-Based Insulated Molecular Wires". *Macromolecules* vol. 55, no. 9 (2022), pp. 3458–3468. DOI: 10.1021/acs.macromol.1c02458.

[149] A. E. Mansour, A. M. Valencia, D. Lungwitz, B. Wegner, N. Tanaka, Y. Shoji, T. Fukushima, A. Opitz, C. Cocchi, and N. Koch. "Understanding the Evolution of the Raman Spectra of Molecularly p-Doped Poly(3-Hexylthiophene-2,5-Diyl): Signatures of Polarons and Bipolarons". *Physical Chemistry Chemical Physics* vol. 24, no. 5 (2022), pp. 3109–3118. DOI: 10.1039/D1CP04985B.

[150] J. C. Roldao, A. Batagin-Neto, F. C. Lavarda, and F. Sato. "Effects of Mechanical Stretching on the Properties of Conjugated Polymers: Case Study for MEH-PPV and P3HT Oligomers". *Journal of Polymer Science Part B: Polymer Physics* vol. 56 (2018), pp. 1413–1426. DOI: 10.1002/polb.24731.

[151] L. Hou, Y. Liu, X. Song, K. Wang, Y. Zhang, B. Zhang, and S. Wang. "Theoretical and Experimental Raman Investigation of Mechanical Strain and Electric Field Effects on Conductive Polymers". *Langmuir* vol. 40, no. 49 (2024), pp. 25997–26006. DOI: 10.1021/acs.langmuir.4c03445.

[152] L. Zhang, D. Liu, J. Li, F. Wu, Q. Zhang, R. Zhang, and Y. Han. "Deformation Mechanism of Conjugated Polymer Films During Single and Cyclic Stretching". *Polymer* vol. 308 (2024), p. 127370. DOI: 10.1016/j.polymer.2024.127370.

[153] COMSOL AB. *COMSOL Multiphysics® v. 6.4*. www.comsol.com. Stockholm, Sweden, 2024.

[154] G. F. Burkhard, E. T. Hoke, and M. D. McGehee. "Accounting for Interference, Scattering, and Electrode Absorption to Make Accurate Internal Quantum Efficiency Measurements in Organic and Other Thin Solar Cells". *Advanced Materials* vol. 22 (2010), pp. 3293–3297. DOI: 10.1002/adma.201000883.

[155] W. S. Koh, M. Pant, Y. A. Akimov, W. P. Goh, and Y. Li. "Three-Dimensional Optoelectronic Model for Organic Bulk Heterojunction Solar Cells". *IEEE Journal of Photovoltaics* vol. 1, no. 1 (2011), pp. 84–92. DOI: 10.1109/JPHOTOV.2011.2163620.

[156] C. Liang, Y. Wang, D. Li, X. Ji, F. Zhang, and Z. He. "Modeling and Simulation of Bulk Heterojunction Polymer Solar Cells". *Solar Energy Materials and Solar Cells* vol. 127 (2014), pp. 67–86. DOI: 10.1016/j.solmat.2014.04.009.

[157] N. Chaudhary, R. Chaudhary, J. P. Kesari, and A. Patra. "Effect of Composition Ratio of P3HT:PC61BM in Organic Solar Cells: Optical and Morphological Properties". *Materials Research Innovations* vol. 22, no. 5 (2018), pp. 282–286. DOI: 10.1080/14328917.2017.1317061.

[158] R. Wang et al. "Ultrafast Hole Transfer Mediated by Polaron Pairs in All-Polymer Photovoltaic Blends". *Nature Communications* vol. 10 (2019), p. 3984. DOI: 10.1038/s41467-019-08361-4.

[159] T. Fukuhara, Y. Tamai, and H. Ohkita. "Nongeminate Charge Recombination in Organic Photovoltaics". *Sustainable Energy & Fuels* vol. 4, no. 9 (2020), pp. 4321–4351. DOI: 10.1039/D0SE00310G.

[160] B. S. Guru and H. R. Hiziroglu. *Electromagnetic Field Theory Fundamentals*. 2nd. Cambridge University Press, 2004. ISBN: 9780521830164.

[161] L. Onsager. "Deviations from Ohm's Law in Weak Electrolytes". *The Journal of Chemical Physics* vol. 2, no. 9 (1934), pp. 599–615. DOI: 10.1063/1.1749541.

[162] L. Onsager. "Initial Recombination of Ions". *Physical Review* vol. 54, no. 8 (1938), pp. 554–557. DOI: 10.1103/PhysRev.54.554.

[163] C. L. Braun. "Electric Field Assisted Dissociation of Charge Transfer States as a Mechanism of Photocarrier Production". *The Journal of Chemical Physics* vol. 80, no. 9 (1984), pp. 4157–4161. DOI: 10.1063/1.447243.

[164] D. Liraz and N. Tessler. "Charge Dissociation in Organic Solar Cells—From Onsager and Frenkel to Modern Models". *Chemical Physics Reviews* vol. 3, no. 3 (2022), p. 031305. DOI: 10.1063/5.0099986.

[165] V. I. Arkhipov, P. Heremans, and H. Bässler. "Why Is Exciton Dissociation so Efficient at the Interface Between a Conjugated Polymer and an Electron Acceptor?" *Applied Physics Letters* vol. 82, no. 25 (2003), pp. 4605–4607. DOI: 10.1063/1.1586456.

[166] S. D. Baranovskii, M. Wiemer, A. V. Nenashev, F. Jansson, and F. Gebhardt. "Calculating the Efficiency of Exciton Dissociation at the Interface Between a Conjugated Polymer and an Electron Acceptor". *The Journal of Physical Chemistry Letters* vol. 3, no. 9 (2012), pp. 1214–1221. DOI: 10.1021/jz300123k.

[167] A. L. Domanski, I. Lieberwirth, E. Sengupta, K. Landfester, H.-J. Butt, R. Berger, J. Rauh, V. Dyakonov, and C. Deibel. "Effect of Morphological Changes on Presence of Trap States in P3HT:PCBM Solar Cells Studied by Cross-Sectional Energy Filtered TEM and Thermally Stimulated Current Measurements". *The Journal of Physical Chemistry C* vol. 117, no. 45 (2013), pp. 23495–23499. DOI: 10.1021/jp406014m.

[168] P. Yu, A. Migan-Dubois, J. Alvarez, A. Darga, V. Vissac, D. Mencaraglia, Y. Zhou, and M. Krueger. "Study of Traps in P3HT:PCBM Based Organic Solar Cells Using Fractional Thermally Stimulated Current (FTSC) Technique". *Journal of Non-Crystalline Solids* vol. 358, no. 17 (2012). Proceedings of the 24th International Conference on Amorphous and Nanocrystalline Semiconductors (ICANS 24) Nara, Japan August 21–26, 2011, pp. 2537–2540. DOI: 10.1016/j.jnoncrysol.2012.01.021.

[169] S. Zeiske, O. J. Sandberg, N. Zarrabi, W. Li, P. Meredith, and A. Armin. "Direct Observation of Trap-Assisted Recombination in Organic Photovoltaic Devices". *Nature Communications* vol. 12, no. 1 (2021), pp. 1–9. DOI: 10.1038/s41467-021-23870-x.

[170] Y. Liu, K. Zojer, B. Lassen, J. Kjelstrup-Hansen, H. G. Rubahn, and M. Madsen. "Role of the Charge-Transfer State in Reduced Langevin Recombination in Organic Solar Cells: A Theoretical Study". *The Journal of Physical Chemistry C* vol. 119, no. 46 (2015), pp. 26588–26597. DOI: 10.1021/acs.jpcc.5b08936.

[171] M. Mingebach, S. Walter, V. Dyakonov, and C. Deibel. "Direct and Charge Transfer State Mediated Photogeneration in Polymer–Fullerene Bulk Heterojunction Solar Cells". *Applied Physics Letters* vol. 100, no. 19 (2012), p. 193302. DOI: 10.1063/1.4711849.

[172] S. Zhang et al. "Molecular Origin of Strain-Induced Chain Alignment in PDPP-Based Semiconducting Polymeric Thin Films". *Advanced Functional Materials* vol. 31, no. 21 (2021), p. 2100161. DOI: https://doi.org/10.1002/adfm.202100161.

[173] A. Khasbaatar, Z. Xu, J.-H. Lee, G. Campillo-Alvarado, C. Hwang, B. N. Onusaitis, and Y. Diao. "From Solution to Thin Film: Molecular Assembly of π-Conjugated Systems and Impact on (Opto)electronic Properties". *Chemical Reviews* vol. 123, no. 13 (2023), pp. 8395–8487. DOI: 10.1021/acs.chemrev.2c00905.

[174] C.-K. Pan, Y.-F. Ding, Z.-F. Yao, X.-Y. Wang, Y.-Y. Zhou, X.-Z. Wu, J.-Y. Wang, and J. Pei. "Role of the Chain Structure and Conformation of Conjugated Polymers on Aggregation Behavior". *Macromolecules* vol. 57, no. 9 (2024), pp. 4107–4117. DOI: 10.1021/acs.macromol.3c02547.

[175] S. Savagatrup, A. D. Printz, T. F. O'Connor, A. V. Zaretski, D. Rodriquez, E. J. Sawyer, K. M. Rajan, R. I. Acosta, S. E. Root, and D. J. Lipomi. "Mechanical Degradation and Stability of Organic Solar Cells: Molecular and Microstructural Determinants". *Energy Environ. Sci.* vol. 8 (1 2015), pp. 55–80. DOI: 10.1039/C4EE02657H.

[176] S. Xu, J. Zhou, and P. Pan. "Strain-induced multiscale structural evolutions of crystallized polymers: From fundamental studies to recent progresses". *Progress in Polymer Science* vol. 140 (2023), p. 101676. ISSN: 0079-6700. DOI: 10.1016/j.progpolymsci.2023.101676.

[177] O. Awartani, B. I. Lemanski, H. W. Ro, L. J. Richter, D. M. DeLongchamp, and B. T. O'Connor. "Correlating Stiffness, Ductility, and Morphology of Polymer:Fullerene Films for Solar Cell Applications". *Advanced Energy Materials* vol. 3, no. 3 (2013), pp. 399–406. DOI: 10.1002/aenm.201200595.

[178] J. Gorenflot, M. C. Heiber, A. Baumann, J. Lorrmann, M. Gunz, A. Kämpgen, V. Dyakonov, and C. Deibel. "Nongeminate Recombination in Neat P3HT and P3HT:PCBM Blend Films". *Journal of Applied Physics* vol. 115, no. 14 (Apr. 2014), p. 144502. ISSN: 0021-8979. DOI: 10.1063/1.4870805.

[179] K. B. Hafsia, M. Ponçot, D. Chapron, et al. "A Novel Approach to Study the Isothermal and Non-isothermal Crystallization Kinetics of Poly(Ethylene Terephthalate) by Raman Spectroscopy". *Journal of Polymer Research* vol. 23, no. 93 (2016). DOI: 10.1007/s10965-016-0984-7.

[180] F. J. Boerio, S. K. Bahl, and G. E. McGraw. "Vibrational Analysis of Polyethylene Terephthalate and its Deuterated Derivatives". *Journal of Polymer Science: Polymer Physics Edition* vol. 14, no. 6 (1976), pp. 1029–1046. DOI: 10.1002/pol.1976.180140607.

[181] R. R. Jones, D. C. Hooper, L. Zhang, D. Wolverson, and V. K. Valev. "Raman Techniques: Fundamentals and Frontiers". *Nanoscale Research Letters* vol. 14, no. 1 (2019), p. 231. DOI: 10.1186/s11671-019-3039-2.

[182] S. Webster and D. Bower. "The Effect of Hydrostatic Pressure on the Position of the 1616 cm^{-1} Raman Line of Poly(ethylene terephthalate)". *Polymer Journal* vol. 36 (22 1995), pp. 4351–4353. DOI: 10.1016/0032-3861(95)92234-6.

[183] D. Bower, E. Lewis, and I. Ward. "Relationships Among Stress-Induced Raman Shifts for Isotropic and Uniaxially Oriented Polymers". *Polymer* vol. 36, no. 18 (1995), pp. 3473–3477. ISSN: 0032-3861. DOI: 10.1016/0032-3861(95)92018-A.

[184] R. J. Angel, M. Murri, B. Mihailova, and M. Alvaro. "Stress, Strain, and Raman Shifts". *Zeit. für Krist. - Cryst. Mat.* vol. 234, no. 2 (2019), pp. 129–140. DOI: https://doi.org/10.1515/zkri-2018-2112.

[185] A. Materny, T. Chen, A. Vierheilig, and W. Kiefer. "A Review on Linear and Non-Linear Resonance Raman Spectroscopy of the Conjugated System Polydiacetylene". *Journal of Raman Spectroscopy* vol. 32, no. 6-7 (2001), pp. 425–445. DOI: 10.1002/jrs.716.

[186] N. Roisin, M. S. Colla, J. P. Raskin, and F. Denis. "Raman Strain–Shift Measurements and Prediction from First-Principles in Highly Strained Silicon". *Journal of Materials Science: Materials in Electronics* vol. 34 (2023), p. 373. DOI: 10.1007/s10854-022-09769-3.

[187] R. Saleh, M. Barth, W. Eberhardt, and A. Zimmermann. "Bending Setups for Reliability Investigation of Flexible Electronics". *Micromachines* vol. 12, no. 1 (2021), p. 78. DOI: 10.3390/mi12010078.

[188] M. Finn, C. J. Martens, A. V. Zaretski, B. Roth, R. R. Søndergaard, F. C. Krebs, and D. J. Lipomi. "Mechanical Stability of Roll-to-Roll Printed Solar Cells Under Cyclic Bending and Torsion". *Solar Energy Materials and Solar Cells* vol. 174 (2018), pp. 7–15. DOI: 10.1016/j.solmat.2017.08.015.

[189] Z. Rang, M. I. Nathan, P. P. Ruden, R. Chesterfield, and C. D. Frisbie. "Hydrostatic-Pressure Dependence of Organic Thin-Film Transistor Current Versus Voltage Characteristics". *Applied Physics Letters* vol. 85, no. 23 (2004), pp. 5760–5762. DOI: 10.1063/1.1829388.

[190] H. Huang and J. Huang, eds. *Organic and Hybrid Solar Cells*. Cham, Switzerland: Springer International Publishing, 2014. DOI: 10.1007/978-3-319-10855-1.

[191] J.-L. Brédas, J. E. Norton, J. Cornil, and V. Coropceanu. "Molecular Understanding of Organic Solar Cells: The Challenges". *Accounts of Chemical Research* vol. 42, no. 11 (2009), pp. 1691–1699. DOI: 10.1021/ar900099h.

[192] O. P. Dimitriev. "Dynamics of Excitons in Conjugated Molecules and Organic Semiconductor Systems". *Chemical Reviews* vol. 122, no. 9 (2022), pp. 8487–8593. DOI: 10.1021/acs.chemrev.1c00648.

[193] S. Pittner, D. Lehmann, D. R. T. Zahn, and V. Wagner. "Charge Transport Analysis of Poly(3-hexylthiophene) by Electroreflectance Spectroscopy". *Physical Review B* vol. 87, no. 11 (2013), p. 115211. DOI: 10.1103/PhysRevB.87.115211.

[194] R. Kerremans, C. Kaiser, W. Li, N. Zarrabi, P. Meredith, and A. Armin. "The Optical Constants of Solution-Processed Semiconductors—New Challenges With Perovskites and Non-Fullerene Acceptors". *Advanced Optical Materials* vol. 8, no. 16 (2020), p. 2000319. DOI: 10.1002/adom.202000319.

[195] D. M. Mamand, D. S. Muhammad, D. Q. Muheddin, et al. "Optical Band Gap Modulation in Functionalized Chitosan Biopolymer Hybrids Using Absorption and Derivative Spectrum Fitting Methods: A Spectroscopic Analysis". *Scientific Reports* vol. 15 (2025), p. 3162. DOI: 10.1038/s41598-025-87353-5.

[196] P. Hang, C. Kan, B. Li, Y. Yao, Z. Hu, Y. Zhang, J. Xie, Y. Wang, D. Yang, and X. Yu. "Highly Efficient and Stable Wide-Bandgap Perovskite Solar Cells via Strain Management". *Advanced Functional Materials* vol. 33, no. 11 (2023), p. 2214381. DOI: 10.1002/adfm.202214381.

[197] P. Makuła, M. Pacia, and W. Macyk. "How to Correctly Determine the Band Gap Energy of Modified Semiconductor Photocatalysts Based on UV–Vis Spectra". *The Journal of Physical Chemistry Letters* vol. 9, no. 23 (2018), pp. 6814–6817. DOI: 10.1021/acs.jpclett.8b02892.

[198] M. C. Scharber and N. S. Sariciftci. "Low Band Gap Conjugated Semiconducting Polymers". *Advanced Materials Technologies* vol. 6, no. 4 (2021), p. 2000857. DOI: 10.1002/admt.202000857.

[199] H. Zhong, F. Pan, S. Yue, C. Qin, V. Hadjiev, F. Tian, X. Liu, F. Lin, Z. Wang, and J. Bao. "Idealizing Tauc Plot for Accurate Bandgap Determination of Semiconductor With Ultraviolet–Visible Spectroscopy: A Case Study for Cubic Boron Arsenide". *The Journal of Physical Chemistry Letters* vol. 14, no. 29 (2023), pp. 6702–6708. DOI: 10.1021/acs.jpclett.3c01416.

[200] T. Tsumuraya, J.-H. Song, and A. J. Freeman. "Linear optical properties and electronic structures of poly(3-hexylthiophene) and poly(3-hexylselenophene) crystals from first principles". *Physical Review B* vol. 86, no. 7 (2012), p. 075114. DOI: 10.1103/PhysRevB.86.075114.

[201] D. W. Scott. "Kernel Density Estimators". *Multivariate Density Estimation*. John Wiley & Sons, Ltd, 1992. Chap. 6, pp. 125–193. DOI: 10.1002/9780470316849.ch6.

[202] T. J. Prosa, M. J. Winokur, J. Moulton, P. Smith, and A. J. Heeger. "X-Ray Structural Studies of Poly(3-alkylthiophenes): An Example of an Inverse Comb". *Macromolecules* vol. 25, no. 17 (1992), pp. 4364–4372. DOI: 10.1021/ma00043a019.

[203] E. Verploegen, R. Mondal, C. J. Bettinger, S. Sok, M. F. Toney, and Z. Bao. "Effects of thermal annealing upon the morphology of polymer–fullerene blends". *Advanced Functional Materials* vol. 20, no. 20 (2010), pp. 3519–3529. DOI: 10.1002/adfm.201000975.

[204] W. Ma, C. Yang, X. Gong, K. Lee, and A. J. Heeger. "Thermally Stable, Efficient Polymer Solar Cells With Nanoscale Control of the Interpenetrating Network Morphology". *Advanced Functional Materials* vol. 15, no. 10 (2005), pp. 1617–1622. DOI: 10.1002/adfm.200500211.

[205] K. Bhargava and V. Singh. "High-Sensitivity Organic Phototransistors Prepared by Floating Film Transfer Method". *Applied Physics Express* vol. 9, no. 9 (2016), p. 091601. DOI: 10.7567/APEX.9.091601.

[206] S. Yuvaraja, A. Nawaz, Q. Liu, D. Dubal, S. G. Surya, K. N. Salama, and P. Sonar. "Organic Field-Effect Transistor-Based Flexible Sensors". *Chemical Society Reviews* vol. 49, no. 11 (2020), pp. 3423–3460. DOI: 10.1039/C9CS00811J.

[207] Z. Wang et al. "Mechanically Robust and Stretchable Organic Solar Cells Plasticized by Small-Molecule Acceptors". *Science* vol. 387, no. 6732 (2025), pp. 381–387. DOI: 10.1126/science.adp9709.

[208] G. Li, V. Shrotriya, J. Huang, Y. Yao, T. Moriarty, K. Emery, and Y. Yang. "High-Efficiency Solution Processable Polymer Photovoltaic Cells by Self-Organization of Polymer Blends". *Nature Materials* vol. 4, no. 11 (2005), pp. 864–868. DOI: 10.1038/nmat1500.

[209] B. Gburek and V. Wagner. "Influence of the Semiconductor Thickness on the Charge Carrier Mobility in P3HT Organic Field-Effect Transistors in Top-Gate Architecture on Flexible Substrates". *Organic Electronics* vol. 11 (2010), pp. 814–819. DOI: 10.1016/j.orgel.2010.01.023.

[210] J. Zhao, L. Sun, Z. Chu, T. Li, F. Zhang, L. Li, and W. Zhang. "Trade-Off of Mechanical and Electrical Properties in Stretchable P3HT/PDMS Blending Films Driven by Interpenetrating Double Networks Formation". *AIP Advances* vol. 10, no. 3 (2020), p. 035020. DOI: 10.1063/1.5145180.

[211] A. Salleo, R. J. Kline, D. M. DeLongchamp, and M. L. Chabinyc. "Microstructural Characterization and Charge Transport in Thin Films of Conjugated Polymers". *Advanced Materials* vol. 22, no. 34 (2010), pp. 3812–3838. DOI: 10.1002/adma.200903712.

[212] S. T. Salammal, E. Mikayelyan, S. Grigorian, U. Pietsch, N. Koenen, U. Scherf, N. Kayunkid, and M. Brinkmann. "Impact of Thermal Annealing on the Semicrystalline Nanomorphology of Spin-Coated Thin Films of Regioregular Poly(3-alkylthiophene)s as Observed by High-Resolution Transmission Electron Microscopy and Grazing Incidence X-ray Diffraction". *Macromolecules* vol. 45, no. 13 (2012), pp. 5575–5585. DOI: 10.1021/ma300906v.

[213] F.-C. Chen, C.-J. Ko, J.-L. Wu, and W.-C. Chen. "Morphological Study of P3HT:PCBM Blend Films Prepared Through Solvent Annealing for Solar Cell Applications". *Solar Energy Materials and Solar Cells* vol. 94, no. 12 (2010), pp. 2426–2430. DOI: 10.1016/j.solmat.2010.09.004.

[214] A. D. Printz, S. Savagatrup, D. J. Burke, T. N. Purdy, and D. J. Lipomi. "Increased Elasticity of a Low-Bandgap Conjugated Copolymer by Random Segmentation for Mechanically Robust Solar Cells". *RSC Advances* vol. 4, no. 26 (2014), pp. 13635–13643. DOI: 10.1039/C4RA00029C.

[215] J. M. Méndez-Hernández, A. Hernández-Pérez, M. Oviedo-Mendoza, and E. Hernández-Rodríguez. "Effects of Tensile Strain on P3HT:PCBM Coated PET/ITO Flexible Substrates". *2021 IEEE 48th Photovoltaic Specialists Conference (PVSC)*. 2021, pp. 1697–1700. DOI: 10.1109/PVSC43889.2021.9519123.

[216] Y. Gao and J. K. Grey. "Resonance Chemical Imaging of Polythiophene/Fullerene Photovoltaic Thin Films: Mapping Morphology-Dependent Aggregated and Unaggregated C=C Species". *Journal of the American Chemical Society* vol. 131, no. 28 (2009), pp. 9654–9662. DOI: 10.1021/ja900636z.

[217] S. Miller, G. Fanchini, Y.-Y. Lin, C. Li, C.-W. Chen, W.-F. Su, and M. Chhowalla. "Investigation of Nanoscale Morphological Changes in Organic Photovoltaics During Solvent Vapor Annealing". *Journal of Materials Chemistry* vol. 18, no. 3 (2008), pp. 306–312. DOI: 10.1039/B713926H.

[218] M. Baibarac, G. Arzumanyan, M. Daescu, A. Udrescu, and K. Mamatkulov. "Anisotropic Photoluminescence of Poly(3-Hexyl Thiophene) and Their Composites with Single-Walled Carbon Nanotubes Highly Separated in Metallic and Semiconducting Tubes". *Molecules* vol. 26, no. 2 (2021), p. 294. DOI: 10.3390/molecules26020294.

[219] T. F. O'Connor, K. M. Rajan, A. D. Printz, and D. J. Lipomi. "Toward Organic Electronics with Properties Inspired by Biological Tissue". *Journal of Materials Chemistry B* vol. 3, no. 25 (2015), pp. 4947–4952. DOI: 10.1039/C5TB00173K.

[220] T. B. Thomsen, C. J. Hunt, and A. S. Meyer. "Influence of Substrate Crystallinity and Glass Transition Temperature on Enzymatic Degradation of Polyethylene Terephthalate (PET)". *New Biotechnology* vol. 69 (2022), pp. 28–35. DOI: 10.1016/j.nbt.2022.02.006.

[221] C. Zhang, A. Khan, J. Cai, C. Liang, Y. Liu, J. Deng, S. Huang, G. Li, and W.-D. Li. "Stretchable Transparent Electrodes with Solution-Processed Regular Metal Mesh for an Electroluminescent Light-Emitting Film". *ACS Applied Materials & Interfaces* vol. 10, no. 24 (2018), pp. 21009–21017. DOI: 10.1021/acsami.8b06691.

[222] M. Stavytska-Barba and A. M. Kelley. "Surface-Enhanced Raman Study of the Interaction of PEDOT:PSS with Plasmonically Active Nanoparticles". *The Journal of Physical Chemistry C* vol. 114, no. 14 (2010), pp. 6822–6830. DOI: 10.1021/jp100135x.

[223] F. Jin, R. Peng, Y. Qiu, J. Zhang, and Z. Ge. "Highly Efficient and Stable Organic Solar Cells Enabled by a PEDOT:PSS/HxMoO3 Hybrid Hole Transport Layer". *ACS Applied Energy Materials* vol. 6, no. 18 (2023), pp. 9532–9542. DOI: 10.1021/acsaem.3c01522.

[224] R. J. Young and S. J. Eichhorn. "Deformation Mechanisms in Polymer Fibres and Nanocomposites". *Polymer* vol. 48, no. 1 (2007), pp. 2–18. DOI: 10.1016/j.polymer.2006.11.016.

[225] G. Strobl. "Deformation, Yielding and Fracture". *The Physics of Polymers: Concepts for Understanding Their Structures and Behavior*. Berlin, Heidelberg: Springer Berlin Heidelberg, 2007, pp. 415–461. DOI: 10.1007/978-3-540-68411-4_10.